From molybdenum based model catalysts to technically applied systems

vorgelegt von

Diplom-Chemiker

Stefan Knobl

aus Selb

Fakultät II - Mathematik und Naturwissenschaften

der Technischen Universität Berlin

zur Erlangung des akademischen Grades

Doktor der Naturwissenschaften

Dr. rer. nat.

genehmigte Dissertation

Promotionsausschuss:

Vorsitzender: Prof. Dr. rer. nat. R. Schomäcker
Berichter/Gutachter: Prof. Dr. rer. nat. M. Lerch
Berichter/Gutachter: Prof. Dr. rer. nat. R. Schlögl

Tag der wissenschaftlichen Aussprache: 09. März 2004

Berlin 2004

D 83

Acknowledgement

Table of contents

From molybdenum based model catalysts to technically applied systems

1 Introduction

1.1 GENERAL INTRODUCTION

About one quarter of added value world wide is produced via catalytic reactions that originate from partial oxidation reactions and contribute to the gross national product of industrialised countries[1]. Many catalytic systems are based on molybdenum oxides. Common reactions are the partial oxidation of propane, propene and acrolein.

The availability and price of the feed stock mentioned above depend largely on economic conditions, caused by changes in refinery technique, resources (natural gas) and political interests in oil producing countries. Propane however needs different catalysts e.g. a molybdenum based catalyst with vanadium, tellurium and niobium (MoVTe) for partial oxidation reactions[1;5;6], whereas the acrolein oxidation is carried out on V and W promoted Mo suboxides[2-4]. Test reactions in this thesis were the partial oxidation of propene (first part) and the partial oxidation of acrolein (second part).

High performance catalysts have been developed for these reactions and optimised by empiric methods. High throughput experimentation (precipitation and testing) is very successfully applied for development and testing of high performance systems. However many important details are not monitored by this approach. Effects caused by minor amounts of additives cannot be precisely recorded. Further parameters which are often considered to be minor but decisive for the preparation are the speed of addition, concentrations of precursor solutions, concentration gradients, speed of stirring, type and form of stirrer, temperature, size of the reaction vessel, solubility, super-saturation, rate of precipitation, mode of operation and mixing sequence. These

influences are difficult to control and to elaborate in detail scientifically in such experiments. The major disadvantage of high throughput experimentation (*hthe*) is that it does not improve the understanding of the chemistry behind the preparation process. Consequently high throughput experimentation is most effective with a knowledge based support and knowledge based key experiments.

Only a knowledge based approach will make straightforward developments of new processes possible and improve industrial catalysts. The ultimate goal of this work was to contribute to the fundamental understanding of partial oxidation catalysis i.e. to understand the function of a catalytically active material. One step towards this goal was the identification of a structure reactivity relation. Suitable model catalysts have been prepared because industrial systems are both structurally and chemically complex[2;4;7-15].

In order to rationalise and explain catalytic reactions various theories are discussed in the literature such as spill over phenomena, site isolation and phase cooperation [1;16;17]. To test these theories and to generate more knowledge about catalytic reaction mechanisms the focal point of this thesis was to provide well defined materials with varying degrees of complexity.

Structural Inorganic Chemistry was a good starting point for the development of preparation strategies for larger scale functional materials such as catalysts based on the paradigm of a principle structure-reactivity relationship. In order to be a useful candidate for a model catalyst more than just the structural information is necessary. Relevant for catalysis is the `real structure´ of the material. This includes knowledge about nanostructuring, particle size, composites, surface phenomena and amorphous parts. Only after having gained thorough information about this structurally complex systems and the influence of the addition of vanadium and tungsten can be understood (chapter 4 and 5).

This enables a knowledge based approach of catalyst preparation and the specific improvement of catalytic properties. This can be seen as an iterative improvement starting with well defined and documented preparation and activation. After a thorough ex- and even more important in situ characterisation of the material the second iterative cycle started with the preparation of the identified active phases in a pure form. Having this well characterised material in hand a structure reactivity relation was established which was refined in the following cycles.

This strategy enabled generation of information about industrially relevant processes under realistic conditions (e.g. reaction temperature and pressure). The obtained material was more similar to the industrial catalysts than single crystals applied in UHV and surface science studies but still well defined enough for scientifically valuable conclusions. Consequently the results are relevant for industrial multi million ton processes.

1.2 MO-ONLY MODEL SYSTEMS

Structural changes of molybdenum species in solution were investigated as a function of pH under preparative conditions. Precursors such as ammonium hepta molybdate (AHM), sodium molybdate (Na_2MoO_4), lithium molybdate (Li_2MoO_4) and potassium molybdate (K_2MoO_4) were dissolved in water. The pH was decreased by adding HNO_3. Precipitation led to solid catalyst precursor. Another method applied to obtain a solid was spray drying[18; 19].

Depending on the preparation conditions the molybdenum oxygen systems developed structures which were also identified in high performance catalysts used in production plants. A hexagonal molybdenum oxide phase showed a structure similar to the M 2 phase of the MoVTeNb system used industrially for the partial oxidation of propane[1;16;17;21-24]. Other authors found the same structure and named it Mo_5O_{16}[20].

Another example is Mo_5O_{14} which is identified as active phase of an industrial MoVW Oxide catalyst for the selective partial oxidation of acrolein or propene to acrylic acid. The characteristic structural motif is a pentagonal bipyramid. This motif is also found in $Mo_{36}O_{112}^{8-}$. Therefore the model system allows studying structurally highly complex materials with low chemical complexity.

The complex parameter space such as temperature, molybdenum concentration, and acid concentration was investigated with an automated titration machine which is an excellent tool for fast screening. The influences of up scaling were examined with a reaction vessel one order of magnitude larger than the titrator.

One important aim of chapter two was further to bridge gaps between Structural Inorganic Chemistry in aqueous solution and Solid State Chemistry and further between Solid Phase Chemistry and functional materials.

Very early investigations on aqueous molybdenum systems were carried out[18; 19]. The main methods used at this time were determination of diffusion coefficients, UV/Vis and conductometric-, potentiometric-, and thermometric–titrations. Saski and Sillen presented the first comprehensive potentiometric investigation[25]. A milestone was the identification of the hepta and octa molybdate structures by X-ray single crystal analysis[26-28].

Significant contributions were made by Aveston and Anacker and also by Tytko and Glemser[29-37]. They combined Raman spectroscopy and single crystal analysis, which enabled them to compare solid state structures with compounds in solution. Contributions to reveal details of the reaction mechanism were delivered by O-NMR spectroscopy[38-40]. Recently Cruywagen published more potentiometric data and a computer aided evaluation[41-43]. All experiments were carried out at room temperature with diluted solutions.

With the help of these data four different structures were obtained on a preparative scale. Using TEM it was shown that so called `minor species´ in solution obviously play an important role in the solidification process. Therefore the role of integral analytical techniques such as Raman spectroscopy and XRD were reflected critically.

One task of this work was to test whether this knowledge is applicable under preparative conditions. This was achieved by carefully controlling parameters such as pH, conductivity, temperature etc. in small and large scale reactions. To bridge the above described gaps the solid phase chemistry of the obtained catalyst precursors was investigated by TG/DSC-MS and the catalytic behaviour was monitored by temperature programmed reaction spectroscopy (TPRS).

1.3 MULTI METAL OXIDES

The second part of this work was dedicated to the more complex system $(Mo_{0.68}V_{0.23}W_{0.09})_5O_{14}$. Based on the knowledge generated by using the model systems a single crystalline phase was obtained. This procedure was investigated by a variety of analytical techniques such as in situ Raman spectroscopy, pH-measurements, conductivity-measurements and UV/Vis spectroscopy. In order to follow the preparation in detail a novel in situ method was developed for UV/Vis measurements based on a reflection fibre optic.

The reaction mechanism that has been set up for the binary model system was in principle transferred to the complex system. The role of vanadium was identified as the linking element between isomerising octamolydate species.

From the catalytic point of view it was shown that the very ill defined phase mixture in the industrial catalyst can be reduced to only one catalytically relevant crystalline phase, namely Mo_5O_{14}. Additional phases are most likely just side products of the preparation procedure.

However, it was shown that a single crystalline phase theory is too simple to explain the whole catalytic process as differences in catalytic activity were detected with compounds of identical stoichiometry and XRD pattern. Similar to the model case amorphous overlayers were detected on the single phase material. Therefore the approach to control the real- and nano structure is much more important than the influence of additives.

Comparing this thesis to traditional catalyst research and optimisation it is striking that almost only additives are changed. Here however a novel approach is presented. Carefully chosen model catalysts which contain only molybdenum and oxygen were described. Several reasons support this choice. Firstly, much catalytic data is available on orthorhombic MoO_3. This has been reviewed lately by Haber[44-46]. Secondly, as nanostructuring oxygen mobility and vacancies are considered to play a major role in catalysis (Mars van Krevelen) molybdenum oxides are good candidates for investigation. Related to this are substoichiometric oxides so called Magneli phases[47-55]. Therefore on the one hand this work is the logical consequence of preceding work carried out in this department on molybdenum oxides e.g. three preceding Ph.D. theses by Dieterle[56], Wienold[57] and Blume[58] and numerous publications[11;15;59;60]. On the other hand this preparative approach opens the way to check recent theories on tailor like materials.

Additionally molybdenum oxides are very sensitive to changes of the preparation conditions. Therefore an investigation of this system is absolutely needed. The role of additives can only be understood after the effects of the matrix are known completely.

Reference List

[1.]   R. K. Grasselli, *Catal.Today* **1999,** *49* 141-153.

[2.]   Hibst, H. and Unverricht, S. BASF AG. [DE 19815281 A 1]. 1981.
       Ref Type: Patent

[3.]   Hibst, H. and Unverricht, S. BASF AG. [DE 19815281 A 1]. 1981.
       Ref Type: Patent

[4.]   Tenten, A., Martin, F.-G., Hibst, H., Marosi, L., and Kohl, V. BASF AG. [EP 668104 B1].
       1995.
       Ref Type: Patent

[5.]   R. K. Grasselli, J. D. Burrington, *Advances in Catalysis* **1981,** *30* 133.

[6.]   R. K. Grasselli, *Surface Reaktion Mechanisms of Selective Olefin Oxidation over Mixed
       Metal Oxides*, (Eds.: M. Che, G. C. Bond) Elsevier, Amsterdam **1985,** p. 275.

[7.]   Kurtz, A. N., Cunningdam, R. W., and Naumann, A. W. Union Carbide Co. [US 4111983].
       1978.
       Ref Type: Patent

[8.]   Novak, V., Sokol, L., and Jelinek, J. CS1207807B. 1981.
       Ref Type: Patent

[9.]   Bertolini, N. and Ferlazzo, S. Euteco Impianti S.p.A. [US 4289654]. 1981.
       Ref Type: Patent

[10.] Kawajiri, T., Uchida, S., and Hironaka, H. Nippon Shokubai Kagaku. [EP 427 508 A1].
       1991.
       Ref Type: Patent

[11.] M. Dieterle, G. Mestl, J. Jäger, Y. Uchida, R. Schlögl, *J.Mol.Catal.A: Chemical* **2001,** *74*
       169.

[12.] M. Dieterle, G. Mestl, *Phys.Chem.Chem.Phys.* **2002,** *4* 822.

[13.] S. Knobl, G. A. Zenkovets, G. N. Kryukova, O. Ovitser, M. Dieterle, R. Schlögl, G. Mestl,
       J.Catal. **2003,** *215* 177-187.

[14.] G. Mestl, Ch. Linsmeier, R. Gottschall, M. Dieterle, J. Find, D. Herein, J. Jäger, Y. Uchida,
       R. Schlögl, *Journal of Molecular Catalysis* **2000,** *162* 455-484.

[15.] T. Ressler, O. Timpe, T. Neisius, J. Find, G. Mestl, M. Dieterle, R. Schlögl, *Journal of Catalysis* **2001,** *191* 75-85.

[16.] R. K. Grasselli, *Topics in Catalysis* **2001,** *15* 93.

[17.] R. K. Grasselli, *Topics in Catalysis* **2002,** *21* 79.

[18.] G. Jander, K. F. Jahr, W. Heukeshoven, *Zeitschrift fur Anorganische und Allgemeine Chemie* **1930,** *194* 383-428.

[19.] A. Rosenheim, *Zeitschrift fur Anorganische und Allgemeine Chemie* **1916,** *96* 139.

[20.] B. Krebs, I. Paulat-Böschen, *Acta Cryst.* **1976,** *B32* **1697**.

[21.] Hatano, M. and Kayou, K. [EP 318295]. 1988. Ref Type: Patent

[22.] T. Ushikubo, K. Oshima, A. Kayou, M. Hatano, *Study of Surface Science and Catalylis*, (Eds.: C. Li, Q. Xin) Elsevier, Amsterdam **1997,** p. 473.

[23.] M. M. Lin, *Applied Catalysis A-General* **2003,** *250* 305-318.

[24.] M. M. Lin, *Applied Catalysis A-General* **2003,** *250* 287-303.

[25.] Y. Sasaki, L. Sillén, *Arkiv För Kemi Mineralogi och Geologi* **1968,** *29* 253.

[26.] I. Lindquist, *Arkiv För Kemi Mineralogi och Geologi* **1950,** *18* 325-341.

[27.] I. Lindquist, *Arkiv För Kemi Mineralogi och Geologi* **1950,** *2* 349.

[28.] I. Lindquist, *Acta Cryst.* **1950,** *3* 159.

[29.] J. Aveston, E. W. Anacker, J. S. Johnson, *Inorganic Chemistry* **1964,** *3* 735-746.

[30.] I. Böschen, B. Buss, B. Krebs, O. Glemser, *Angew.Chem.* **1973,** *85* 409.

[31.] O. Glemser, W. Holznagel, A. Iftikhar, *Z.Naturforsch.* **1965,** *20b* 192.

[32.] K.-H. Tytko, B. Schönfeld, B. Buss, O. Glemser, *Angewandte Chemie* **1973,** *85* 305-307.

[33.] K.-H. Tytko, B. Schönfeld, *Zeitschrift fur Naturforschung* **1975,** *30b* 471-484.

[34.] K.-H. Tytko, O. Glemser, *Adv.in Chem.Series* **1976,** *19* 239-315.

[35.] K.-H. Tytko, O. Glemser, *Adv.Inorg.Chem.Radiochem* **1976,** *19* 239.

[36.] K.-H. Tytko, G. Baethe, E. R. Hirschfeld, K. Mehmke, D. Stellhorn, *Z.Anorg.Allg.Chem.* **1983,** *503* 43-66.

[37.] K.-H. Tytko, G. Baethe, *Z.Anorg.Allg.Chem.* **1987,** *555* 85-97.

[38.] V. W. Day, M. F. Fredrich, W. G. Klemperer, W. Shum, *J.Am.Chem.Soc.* **1977,** *99* **6146**.

[39.] W. G. Klemperer, W. Shum, *J.Am.Chem.Soc.* **1976,** *98* 8291.

[40.] W. G. Klemperer, *Angew.Chem.* **1978,** *17* 246.

[41.] J. J. Cruywagen, J. B. B. Heyns, *Inorganic Chemistry* **1987,** *26* 2569.

[42.] J. J. Cruywagen, *Advances in Inorganic Chemistry* **2000,** *49* 127.

[43.] J. J. Cruywagen, A. G. Draaijer, J. B. B. Heyns, E. A. Rohwer, *Inorganica Chimica Acta* **2002,** *331* 322.

[44.] J. Haber, *Catalysis by Transition Metal Oxides*, (Eds.: R. Grasselli, J. Brazdil) American Chemical Society, Washington D. C. **1985,** p. 1.

[45.] J. Haber, *3 rd World Congress on Oxidation Catalysis, (R.K.Grasseli, S.T.Oyama, A.F.Gaffney, J.E.Lyons)* **1997,** *1997 Elsevier, Amsterdam* 1.

[46.] J. Haber, V. Turek, *Journal of Catalysis* **2000,** *190* 320-326.

[47.] G. Andersson, A. Magnéli, *Acta Chemica Scandinavica* **1950,** *xxx* 793-797.

[48.] A. Magnéli, *Arkiv För Kemi Mineralogi och Geologi* **1946,** *24 a* 1.

[49.] A. Magnéli, *Acta Chemica Scandinavica* **1948,** *2* 501-517.

[50.] A. Magnéli, *Acta Chemica Scandinavica* **1948,** *2* 861-871.

[51.] A. Magnéli, G. Andersson, B. Blomberg, L. Kihlborg, *Analytical Chemistry* **1952,** *24* 1998.

[52.] A. Magnéli, *Research* **1952,** *5* 394.

[53.] A. Magnéli, *Acta Cryst.* **1953,** *6* 495.

[54.] A. Magnéli, G. Andersson, *Acta Chemica Scandinavica* **1955,** *9* 1378-1381.

[55.] A. Magnéli, B. Blomberg-Hansson, L. Kihlborg, G. Sundkvist, *Acta Chemica Scandinavica* **1955,** *9* 1382.

[56.] Dieterle, M., TU Berlin, **2000**.

[57.] Wienold, J., **2003**.

[58.] Blume, A., TU Berlin, **2004**.

[59.]   M. Dieterle, G. Mestl, *Phys.Chem.Chem.Phys.* **2002,** *4* 822.

[60.]   O. Ovitser, Y. Uchida, G. Mestl, G. Weinberg, A. Blume, J. Jager, M. Dieterle, H. Hibst, R. Schlögl, *J.Mol.Catal.A: Chemical* **2002,** *185* 291-303.

2 Controlled preparation of molybdenum oxide catalysts

2.1 INTRODUCTION

The production of high value petrochemicals such as acrolein or acrylic acid is carried out by selective oxidation of lower alkanes over molybdenum oxide based catalysts[1-9]. Empirical optimisation of the catalyst performance through doping with foreign cations has already reached a high level again stressing the huge potential of such catalysts. There is a number of recent patents for a material with the approximate composition of $Mo_1V_{0.33}Te_{0.22}Nb_{0.11}O_x$[10-15]. Characterisation of this material has led to the identification of two major phases amongst other minor phases. The first one (M1) is orthorhombic and isostructural of $Cs_{0.7}(NbW)_5O_{14}$[16] and shows a great similarity to Mo_5O_{14} because of its pentagonal bipyramides as the most striking feature. The second phase (M2) is pseudo hexagonal[11] and isostructural to $Sb_4Mo_{10}O_{31}$.

Although additives are proven to enhance catalytic activity there is an ongoing debate about whether they act as structural builders or linkers and therefore favour a certain type of structure or they form active sites themselves. Grasselli[17-19] has outlined `seven pillars of selective oxidation´, in which `phase cooperation and site isolation´ are two of his major concepts. As testing these concepts on multi component and multi phase industrial catalysts is rather difficult, there is a need for good model catalysts. A breakthrough was achieved recently by the successful synthesis of single phase $(MoVW)_5O_{14}$ material. This synthesis was done with a nanostructured precursor as intermediate in which vanadyl linkers connect octamolybdate species, that were distorted by tungsten atoms[20]. During the catalytic reaction at elevated temperature the material undergoes structural and electronic changes and its activity and selectivity are enhanced. The post mortem sample shows the Mo_5O_{14}-type structure, which was first discovered by Kihlborg[21]. This work led to the conclusion that the function of V and W atoms is only to form and stabilise the catalytically active site of Mo_5O_{14}. This assumption would be further validated, if a solid containing such sites would be successfully prepared containing only molybdenum and oxygen. This material should then have a similar catalytic activity to the industrial $(MoVW)_5O_{14}$ catalyst.

Another matter of debate is whether the catalytic reaction happens on bulk-terminated oxide, as can be deducted from Grassellis work, or on differently coordinated Mo oxide surface layers. The latter statement can be supported by studies from Wachs *et al.* who investigated methoxy chemisorption on monolayer supported Mo oxide prepared by incipient wetness[22]. They found a correlation between the monolayer of methoxy species of the surface and the number of active surface sites. These sites were formed by transformation of crystalline (bulk) metal oxides into active surface metal oxide species by reaction-induced spreading. This phenomenon clearly depends on the nature of the support. Bell *et al.* identified the active surface species as two dimensional MoO_x polymers, who are favoured at low surface densities <4.5 nm per Mo. Formation of Mo^{6+} centers and oxygen vacancies as active sites was observed for ODH of propane. Increasing density resulted in a decline in catalytic activity per Mo atom, because of transformation into three dimensional MoO_3 structures with inaccessible Mo species[23-27]. Small additions of alkali (<0.2 per Mo) do not lead to any structural changes, however, some electronic modifications are detected. Haber *et al.* performed kinetic measurements of propene oxidation on bismuth molybdates and postulated the existence of two different oxygen species at the surface that carry out different functions during the catalytic process[28]. Whilst lattice oxygen is responsible for the partial oxidation of propene into acrolein or acrylic acid, total oxidation is carried out by surface oxygen species that are in equilibrium with the gas phase.

The results mentioned above generally imply that the active species consist of nanostructured binary molybdenum oxides. In order to test this hypothesis any influence of dopants or support on the catalytic reaction has to be ruled out, therefore it is highly desirable to synthesise unsupported and undoped MoO_x polymers and test their catalytic activity against the industrial catalysts and as well against bulk MoO_3. A variety of such polymolybdates has been successfully obtained by controlled precipitation. The first prominent compound of this type was reported by Böschen *et al.* in $K_4Mo_{36}O_{112}$ *8 H_2O[29-33]. Like the Mo_5O_{14} and M1 industrial catalysts, this species also contains the pentagonal bipyramide as a structural motif, that is recognised as an important building block[34] for large polymolybdates (keplerates, >500 atoms). Even in the photochemical molybdenum blues reaction this motif is discussed[35].

The approach used in this paper was to obtain the pentagonal bipyramides directly from precipitation of nano sized clusters. The aim was to directly influence the nature of the nano clusters by careful adjustment of the reaction conditions. A variety of control

variables have been reported in earlier work, dealing with pH dependent reactions of Mo compounds in aqueous solution[36-38] [39-46] [47-50] [51;52] [53] [34] [52;54-62] [63-66] [67-69]. These variables are extrapolated on a preparative scale in order to ensure the production of different structural families. Clusters containing these pentagonal bipyramides should show catalytic activity without any need for calcination or activation, as these procedures cause uncontrolled reformation of the clusters, leading to pure ortho-MoO_3 revealed in its defect-free form, if the temperature is raised above 500 °C. This material shows unsuitable local chemical bonding for selective oxidation[9;70-72] and requires tuning by the introduction of defects that can be achieved by heating the sample above the limit of oxygen diffusion to the surface. Finally up scaling is an important factor to ensure a reproducible production of catalytic material especially when diffusion plays an important role in the reaction mechanism.

2.2 EXPERIMENTAL

Preparation

All solids were obtained by precipitation. Small-scale preparation (200 ml) to scan the parameter range was carried out in a Mettler-Toledo DL 77 Titrator to which an automated Rondo 60 sample changer was attached. The Rondo was modified in such a way that a water bath maintained constant temperature conditions. As starting material aqueous solutions of $(NH_4)_6Mo_7O_{24}$ * 4 H_2O (AHM), Na_2MoO_4, Li_2MoO_4, K_2MoO_4 (all MERCK, p.a.) at a concentration range between 0.28 mol/l and 2 mol/l calculated on Mo was used. As precipitation agent HNO_3 (1 mol/l − 5 mol/l) was applied. The experiments were carried out at 30 °C, 50 °C and 70 °C.

In a separate set of experiments the effects of up scaling have been studied by using a home-made 4l computerised semi-technical preparation set-up allowing to control the temperature accurately and to measure pH and electrical conductivity. The same concentration ranges have been used as before, the starting solution was 1l. The pH and was recorded and analyzed digitally. After the addition of HNO_3 the samples were allowed to age for 1 h at 35 °C. All samples were filtered and dried in a desiccator over dry gel. It is crucial not to wash the samples, as this would cause partial re- dissolution.

XRD

A STOE STADI-P focusing monochromatic transmission diffractometer equipped with a Ge(111) monochromator and a position sensitive detector. Cu-K_a radiation was used. The phase analysis was performed with the STOE Win XPOW software package (version 1.06; Stoe Darmstadt, Germany) and with PowderCell (V 2.3; Bundesanstalt für Materialforschung und -prüfung (BAM) Berlin, Germany).

TEM

The samples were prepared for transmission electron microscopy (TEM) by standard preparation routines. The powder is suspended in ethanol and dispersed onto a standard meshed copper grid coated with a holey carbon film, by dipping the grid into the slurry. The samples are studied in a Philips CM 200 FEG electron microscope operated at 200~kV and equipped with a Gatan Image Filter and a CCD camera. Scanning electron microscopy (SEM) images are acquired with an S 4000 FEG microscope (Hitachi).

Raman DRIFTS

Raman spectroscopy was performed on a Labram I (Dilor) instrument equipped with a confocal microscope (Olympus). A notch filter (Kaiser Optical) was applied to cut off the laser-line and the Rayleigh scattering up to 150 cm^{-1}. The spectrometer is equipped with a CCD camera (1024*298 diodes), which is Peltier cooled to -30 °C to reduce the thermal noise. A He-laser (Melles Griot) was used to excite the Raman scattering at 632 nm with a laser power of 1,4 mW. The following spectrometer parameters were used: microscope objective: 10; slit width: 200 μm (spectral resolution: 2.5 cm^{-1}), integration time: 30 s per spectrum and 5 averages.

DRIFTS were recorded on a Bruker ifs 66 FTIR-spectrometer equipped with OPUS software. 100 spectra were averaged and the resolution was 4 cm^{-1}. The spectra were recorded in air. For background measurement KBr was used. The aperture was set to 5 mm, scan velocity 7; 20 kHz.

UV/Vis/NIR

A commercial UV-Vis-NIR spectrometer (Lambda 9, Perkin Elmer) equipped with an integrating sphere was supplemented with a construction to measure in situ diffuse reflectance spectra from room temperature to 450 °C. A full description of the complete setup has been given elsewhere[73].

BET

BET was carried out on a Quantachrom Autosorb-1 apparatus. Degassing of the sample was carried out at 120 °C for two hours. 0.3 g of sample was weighed in and nitrogen was used as adsobate.

TG

Thermal analysis (TA) was performed with a STA 449 C Jupiter apparatus (Netzsch). Flowing helium and air atmosphere were applied (the flow rate was set at 15 ml/min in both cases). The heating rate was set at 5 °C/min. Mass spectrometric analysis (TG-MS) of the evolved gases was performed with an Omnistar quadrupole mass spectrometer (Pfeiffer Vacuum).

TPRS

The test reaction for TPRS was the partial oxidation of propene. The instrumentation for the TPRS runs consists of a simple tubular reactor. The sample (50 mg) is diluted in a matrix of BN and SiC (for amelioration of heat transfer).

The total gas flow is set to 100 ml/min and the resulting hsv ranges about 13500. The feed is composed of 10 % propene and oxygen each in He. The temperature is ramped twice to 500 °C by 5 °C/min in two successive cycles.

2.3 RESULTS

Depending on preparation conditions such as temperature, molybdenum concentration, acid concentration and the choice of starting material and counter ion such as Li^+, Na^+, K^+, NH_4^+ four different families of products were obtained by precipitation: orthorhombic MoO_3, hexagonal MoO_3, trimolybdate and a supramolecular $Mo_{36}O_{112}^{8-}$ like compound (Fig. 2.1).
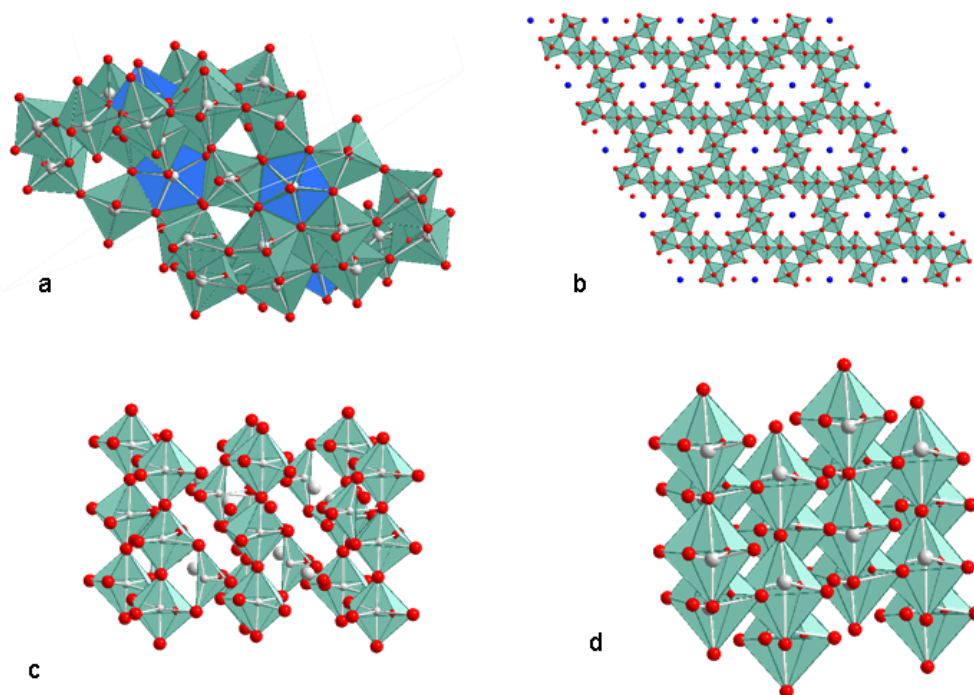
Figure 2.1: Lead structures of the obtained materials identified by XRD and Raman; a) supramolecular compound; b) hexagonal MoO₃; c) trimolybdate; d) orthorhombic MoO₃

2.3.1 Orthorhombic MoO₃

Orthorhombic MoO_3 is only obtained with Li^+ as counter ion. Regardless of the preparation temperatures further heating to the boiling point was necessary to force precipitation.

pH-dependency

Lithium monomolybdate shows typically an initial pH at around 6.5 (Fig. 2.2). Acidification with nitric acid leads first to a sudden pH drop followed by a buffering region around pH = 5.5 and a further drastic pH drop down to pH = 2. This pH curve is very temperature dependent as the sample treated at 50 °C needs the smallest amount of acid in this series to reach its final pH = 1. The second largest acid volume is used for the sample at 70 °C. The 30 °C sample needs the largest amount of acid. In Fig. 2.2 the amount of acid added is normalised to the acid concentration and to the molybdenum concentration. Therefore all pH data shown in this plot can be directly compared.
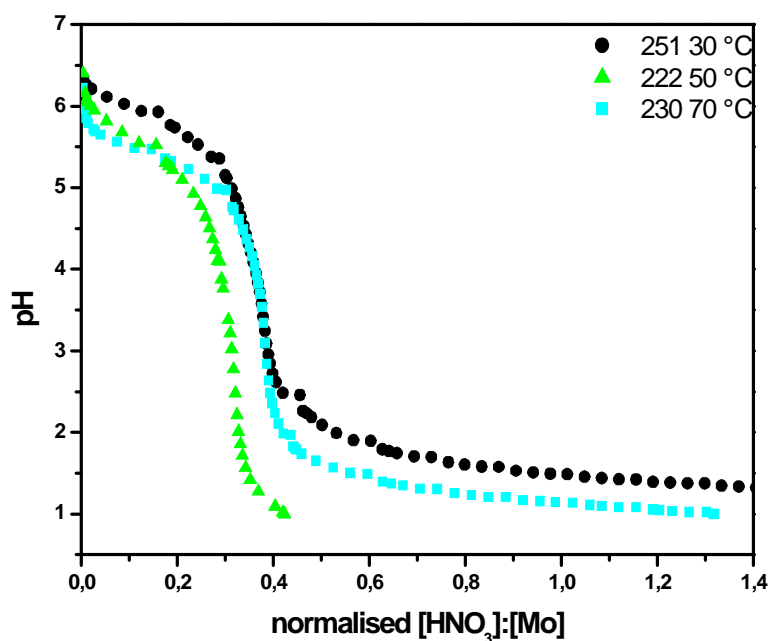
Figure 2.2: pH curve for samples (LiMoO$_4$ 0.28 mol/l HNO$_3$ 2 mol/l) 251, 30 °C; 222, 50 °C; 230, 70 °C. Data normalised to molybdenum and acid concentration respectively

XRD

All three samples show the pattern of orthorhombic MoO$_3$ however poorly crystalline. One typical pattern is shown in Fig. 2.4 B (222). The indexing was done according to PDF 5-508.

Raman

Bands are detected at 996, 825, 667, 376, 335, 292 and 244 cm^{-1}. This is in line with the bands reported in the literature[74] for orthorhombic MoO$_3$ apart from the band at 825 cm^{-1}, which should be at 820 cm^{-1}. Further a shoulder is detected at 980 cm^{-1}, which does not belong to MoO$_3$. Fig. 2.5 (222) shows a typical Raman spectrum, the other samples are listed in Table 2.6.

DRIFTS

Bands are found at 840, 743, 1000, 1387, 1636, 1946, 2389, 3584 cm^{-1}. The band at 3584 cm^{-1} is assigned to OH stretching and deformation frequencies of hydrated water respectively. The band at 1636 cm^{-1} suggests that water is present as water molecules as well as hydroxyl[75-77]. Representative spectra are shown in Fig. 2.9 and 2.10.

16

UV/Vis NIR

Bands in the NIR region are detected at 1430, 1790, 1930 and 2280 nm as seen in Fig. 2.25. The sample prepared at 50 °C shows the biggest band areas and a band gap energy of 3.37 eV. The band gap energy of the other two samples is 3.48 eV (Fig. 2.7 I, II). Results are listed in Table 2.4. A strong band at 970 nm is observed in the samples prepared from 0.28 mol/l Li_2MoO_4 with 2 mol/l HNO_3 at 30 °C and 50 °C. Such a band cannot be observed for all other samples with hexagonal MoO_3, supramolecular $Mo_{36}O_{112}^{8-}$, and trimolybdate structure as can be seen in Fig. 2.13.

Thermal analysis

Although precipitation was only achieved after boiling of the aqueous solutions, the precipitation temperature seems to have an effect on the behaviour during calcination. The sample (Fig. 2.3; 222) prepared at 50 °C shows the most characteristic events in the
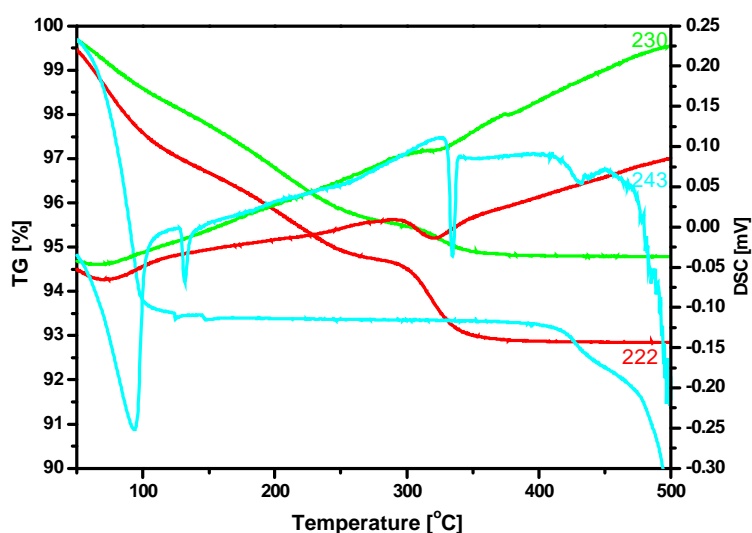
Figure 2.3: TG-DSC of 222, 230 and 243

TG-MS. The biggest overall mass loss is detected for the sample prepared at 50 °C (7 %) and the last mass loss at 320 °C is most pronounced and accompanied by a significant endothermic signal. This sample shows a peak in the water signal (MS) at 75 °C. After that water is evolved constantly up to 240 °C. NO_X at 320 °C is evolved. The intensity of the water signal is nicely reflected by the DSC trace. The maximum of the water MS trace coincides with a minimum in the DSC curve. As soon as the water MS trace is declining the DSC curve is getting steeper.

Relative to the other two samples the NO_X signal is much bigger. The TG traces of the samples prepared at 30 °C and at 70 °C are similar showing an almost constant mass

loss up to 266 °C and hardly any mass loss up to appr. 310 °C. From 372 °C upwards no more mass losses are detected. Some decisive differences however appear in the DSC trace. The sample prepared at 30 °C shows an exothermic transition at 238 °C which coincides with the declining water MS trace. As soon as no more water is present the DSC trace is changing its curvature. An endothermicity is detected at 352 °C at the same time NO_X is evolved. In contrast to that the sample prepared at 70 °C shows a plateau in the DSC curve at 311 °C. From this temperature on no more water is evolved. At 330 °C water is leaving the sample.

TPRS

The obtained orthorhombic MoO_3 starts to convert propene to CO_2 at around 300 °C. At 350 °C a plateau is reached. Another rise in activity is observed at 370 °C and at 430 °C the maximum CO_2 production is measured (Fig. 2.20 and 2.21).

2.3.2 Trimolybdate

Trimolybdate is obtained with K^+ as counter ion and at a reaction temperature of 70 °C and a minimum molybdenum and acid concentration of 2 mol/l. In this investigation trimolybdate was obtained with K_2MoO_4 2 mol/l, HNO_3 2 mol/l and 5 mol/l. The compound precipitates spontaneously (sample 244 and 243).

pH dependency

The titration starts at around pH = 9, buffers at around pH = 7 and reaches the final pH = 1 asymptotically (Fig. 2.18).

XRD

Using K_2MoO_4 2 mol/l and HNO_3 2 mol/l the XRD pattern (Fig. 2.4, sample 243) indicates a phase mixture containing hexagonal MoO_3, trimolybdate and at least one more phase. The interpretation is difficult because peaks can shift depending on the preparation conditions.
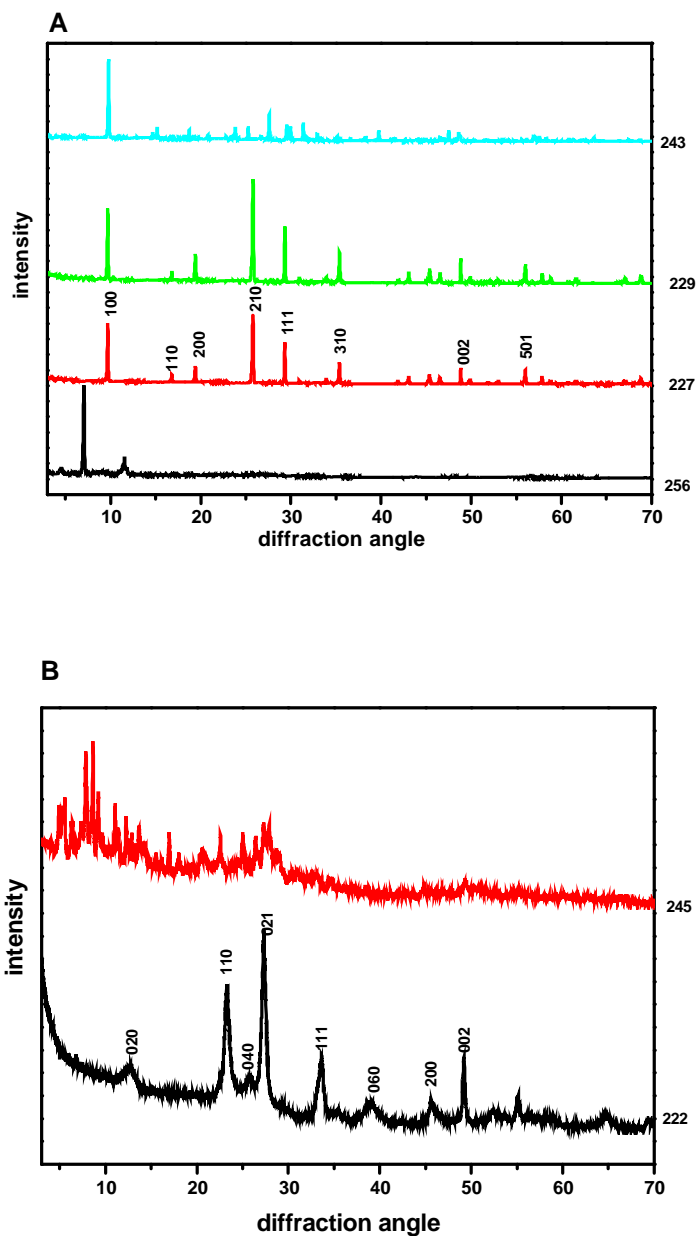
Figure 2.4: A XRD pattern of representative samples. 256, supramolecular phase from AHM; 227, hexagonal MoO$_3$ from AHM; 229, hexagonal MoO$_3$ from K$_2$MoO$_4$; 243, supramolecular from K$_2$MoO$_4$;

B 222, orthorhombic MoO$_3$ from Li$_2$MoO$_4$; 245, supramolecular compound

It is reported[46;78] that cation spaces could be either occupied by H$_3$O$^+$ or K$^+$. Depending on this crystal parameters will change. However, it cannot be ruled out that more phases are present. Increasing the acid concentration increases the amount of trimolybdate.

Raman

The main bands are observed at 949, 938, 909, 612, 372 and 217 cm^{-1}. Taking the intensity pattern into account it fits with the literature values reported for $K_2O * 3 MoO_3 * x H_2O$ (Fig. 2.5). However there is a slight, non-systematic shift in band positions. In the literature a triad of very sharp bands is reported. This triad is not well resolved when HNO_3 2 mol/l is used as precipitation agent and a further shoulder is detected at 873 cm^{-1}, which is not reported in the literature. The band detected at 1051 cm^{-1} is assigned to nitrate from the precipitation agent. Again an increase of the acid concentration leads to a purer product and the band positions fit exactly with the ones reported in the literature.
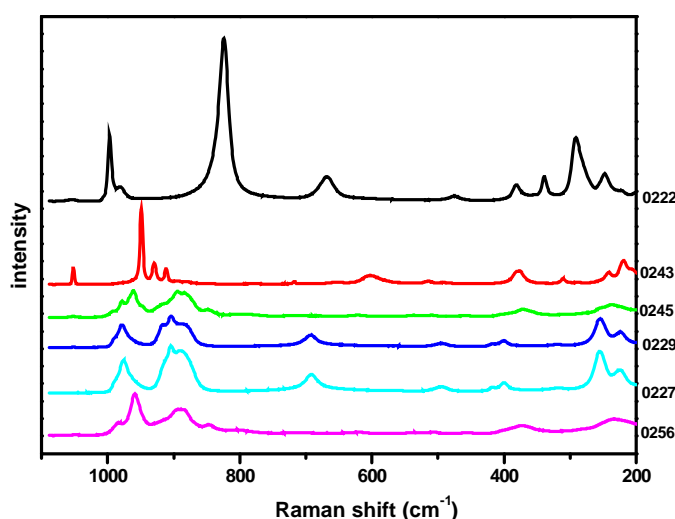
Figure 2.5: Raman spectra of representative samples. 256, supramolecular phase from AHM; 227, hexagonal MoO_3 from AHM; 229, hexagonal MoO_3 from K_2MoO_4; 245, supramolecular from K_2MoO_4; 243, trimolybdate; 222, orthorhombic MoO_3

DRIFTS

Bands are detected at 726, 804, 880, 955, 1337, 1447, 1633, 2170, 2383, 2754, 3298, 3532 cm^{-1}. The assignment of the water bands corresponds to the one done above for the orthorhombic MoO_3. At lower wavenumbers different bands are detected. Therefore IR can discriminate among these compounds (Fig. 2.9 and 2.10).

UV/Vis/NIR

NIR bands are detected at 1435 and at 1935 nm with quite low intensity. In addition two weak bands at 1790/1810 nm and stronger bands at 2000, 2095 and 2250 nm were detected. Besides a small LMCT centred at 284 nm and an Eg of 3.77 eV are observed (Table 2.4). The band gap energy in the sample prepared from 2 mol/l K_2MoO_4 with 2 (5) mol/l HNO_3 at 70 $^{\circ}$C is 3.77 eV. The sample prepared from the higher concentrated acid (5 mol/l) shows a band gap energy of 3.77 eV.

Thermal Analysis

Trimolybdate (Fig. 2.3, sample 243) reaches mass constancy at 130 °C. At this temperature a sharp endothermic signal is detected. A further endothermic signal appears at 333 °C. At around 420 °C the samples start to melt. The two samples do not show any decisive differences.
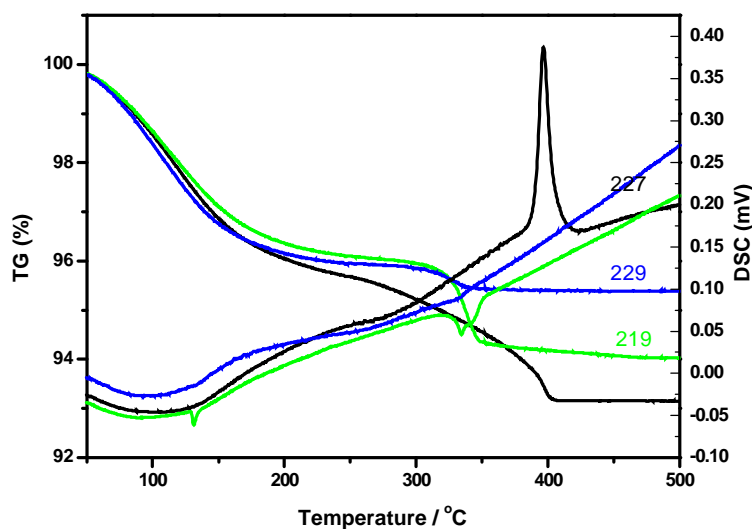
Figure 2.6: TG-DSC of 219, 229 and 227

2.3.3 Hexagonal MoO₃

Hexagonal MoO_3[79-82] is obtained with Na^+, K^+ and NH_4^+ as counter ion. It is either obtained by spontaneous precipitation at higher temperatures or by further heating of the

solution at pH = 1 to the boiling point. Finally hexagonal MoO_3 is only obtained from rather dilute molybdenum stem solutions.

Employing Na^+ as counter ion and a molybdenum and acid concentration of 2 mol/l respectively no reaction temperature yielded hexagonal MoO_3 spontaneously. After heating hexagonal MoO_3 was obtained (samples 252, 226, 255 and 231).

Potassium as counter ion yielded hexagonal MoO_3 when the molybdenum concentration was 0.28 mol/l and HNO_3 2.0 mol/l for the reaction temperatures 50 °C and 70 °C only after further heating (samples 219, 229, 247 and 233).
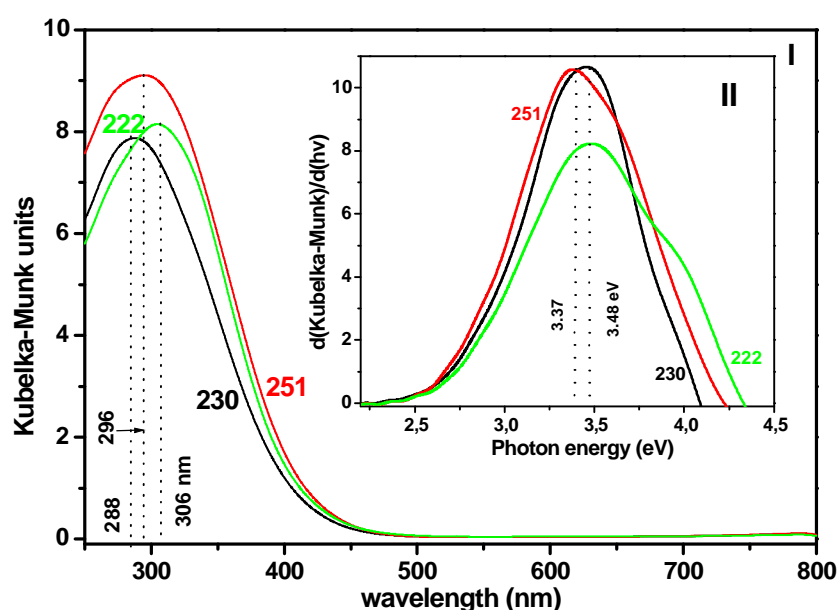
Figure 2.7: Spectroscopic characteristics of orthorhombic MoO_3, 251, 222 and 230. I. UV/Vis spectra; II. band gap energies Eg

Ammonia as counter ion yielded hexagonal MoO_3 with an AHM concentration 0.7 mol/l (Mo) and HNO_3 1 mol/l at 50 °C and at 70 °C after further heating (samples 227, 232 and 248).

pH dependency

Using Na^+ as counter ion the starting pH is 8.2 for the reaction at 30 °C (Fig. 2.8). Adding 2 mol/l HNO_3 leads to a pH drop. At around pH = 7.5 a buffering sets in, which is followed by a large pH drop again down to pH = 1. The other two reaction temperatures show a similar behaviour, however the starting pH is lower and the first
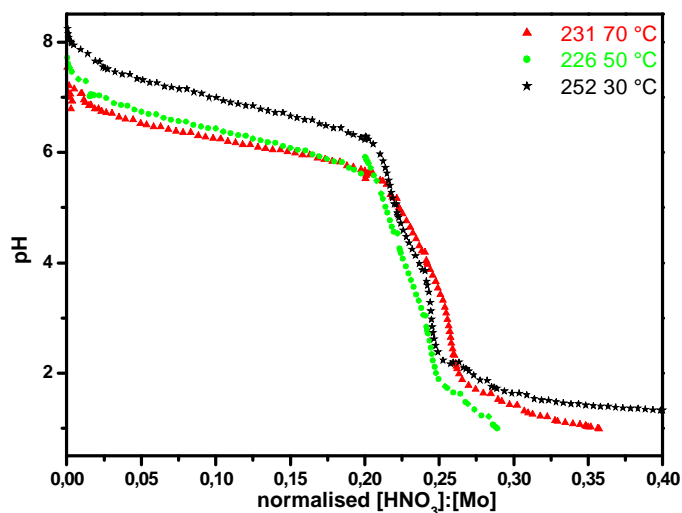
Figure 2.8: pH curve for samples (Na$_2$MoO$_4$ 2 mol/l, HNO$_3$ 2 mol/l) 252, 30 °C; 226, 50 °C; 231, 70 °C. Data normalised to molybdenum and acid concentration respectively

buffering takes place at around pH = 6.8. It is noteworthy that the sample prepared at 50 °C needs considerably less acid to reach the final pH. The highest amount of acid is needed for the sample prepared at 30 °C.

In the potassium case the reaction starts at around pH = 7. Buffering occurs at around pH = 6.5. Apart from that the curve is very similar to the one described above for Sodium. Again the reaction at 50 °C needs considerably less acid (Fig. 2.18).

The reaction is slightly changing with ammonia as counter ion because the starting compound is now the heptamolybdate ion rather than the mono molybdate ion. Therefore the reaction starts at around pH = 5.3. After that the pH is dropping fairly constantly until pH = 2 is reached. At this point the two pH traces separate. The reaction at 50 °C reaches pH = 1 fairly quickly whereas the solution at 70 °C shows a stronger buffering and needs much more acid (Fig. 2.14 and 2.19).

XRD

One representative diffraction pattern of the samples prepared from Na$_2$MoO$_4$ is shown in Fig. 2.4 A indexed according to PDF-39-35 and ICSD-38415. The pattern fits quite good to the one reported in the literature apart from a decisive broadening of the signal at 25.5 2 theta and some additional small signals in the region from 49.3 2 theta to 53.3 2 theta and at around 61 2 theta.

Potassium as counter ion produced clearly hexagonal MoO$_3$. The signals however possesses shoulders, consequently a second phase with different d-spacings might be present. Ammonia as counter ion yielded a similar result (Fig. 2.4 A).

Raman

The Raman spectra recorded from the hexagonal MoO_3 obtained from Na_2MoO_4, K_2MoO_4 and AHM shows bands at 978, 904, 884, 692, 494, 399, 255 and 229 cm^{-1}. Only minor shifts and changes in band shape occur. Representative spectra are shown in Fig. 2.5.

DRIFTS
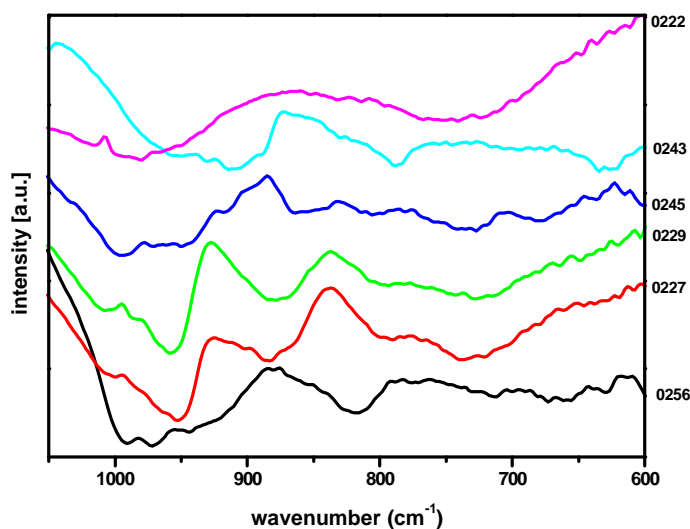
Figure 2.9: Diffuse reflectance fourier transform spectroscopy (DRIFTS) of representative samples. 256, supramolecular phase from AHM; 227, hexagonal MoO_3 from AHM; 229 hexagonal MoO_3 from K_2MoO_4; 245 supramoleculart from K_2MoO_4; 243, trimolybdate; 222, orthorhombic MoO_3

Depending on the counter ion small changes are observed. The main bands are detected at around 726, 804, 886, 955, 996 (sh), 1360, 1612, 3305, 3571 cm^{-1}. Especially the region below 1000 cm^{-1} does not fit exactly to literature values. However in the literature it is shown that not only Mo-O bond stretching and bending vibrations are detected but also H_2O liberational motions[75]. Therefore even the band positions in this region depend on the quantity of water and ammonia. However the main features match (Fig. 2.9 and 2.10).
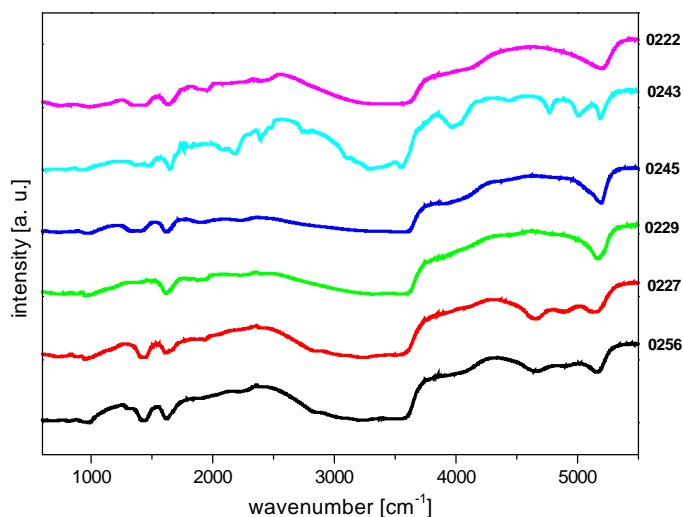
Figure 2.10: DRIFTS of representative samples. 256, supramolecular phase from AHM; 227, hexagonal MoO$_3$ from AHM; 229, hexagonal MoO$_3$ from K$_2$MoO$_4$; 245, supramolecular from K$_2$MoO$_4$; 243, trimolybdate; 222, orthorhombic MoO$_3$

UV/Vis/NIR

Table 2.4 shows the spectroscopic characteristics of samples prepared from 2 mol/l Na$_2$MoO$_4$ with 2 mol/l HNO$_3$ at 30 °C, 50 °C and 70 °C, which indicated different band positions depending on temperature. The spectrum of the sample prepared at 30 °C shows a LMCT band at about 320 nm. This band is red shifted by 8 nm in the spectrum of the sample prepared at 70°C and by 12 nm in the spectrum of the sample prepared at 50 °C. All three samples have the same Eg values of 3.27 eV (Table 2.4). In addition these samples exhibit a very similar behaviour in the NIR region. A very strong absorption band at 1955 nm, a small band at 1430 nm and relatively weak absorption bands at 1820 and 2280 nm appear, whereas the sample prepared at 70 °C leads to a spectrum with slightly higher band intensities. The spectra in the NIR range recorded of the compound prepared from Na$_2$MoO$_4$ are very similar, the main bands are detected at 1430, 1820, 1955 and 2280 nm. Whereas the sample prepared at 70 °C shows the biggest band areas. Band gap energies are very similar as well. For all three compounds 3.27 eV are found.

Switching to K$^+$ as counter ion the bands are located at 1435, 1820, 1935, 2090 and 2235 nm. The band gap energy amounts to 3.30 eV.

Finally the NIR bands for the ammonia-containing compound (0.7 mol/l AHM) are situated at 1440, 1570, 1945, 2040 and 2150 nm. The band gap energy is 3.35 eV for the hexagonal compound prepared at 50 °C and 3.36 eV for the one prepared at 70 °C.

Thermal Analysis
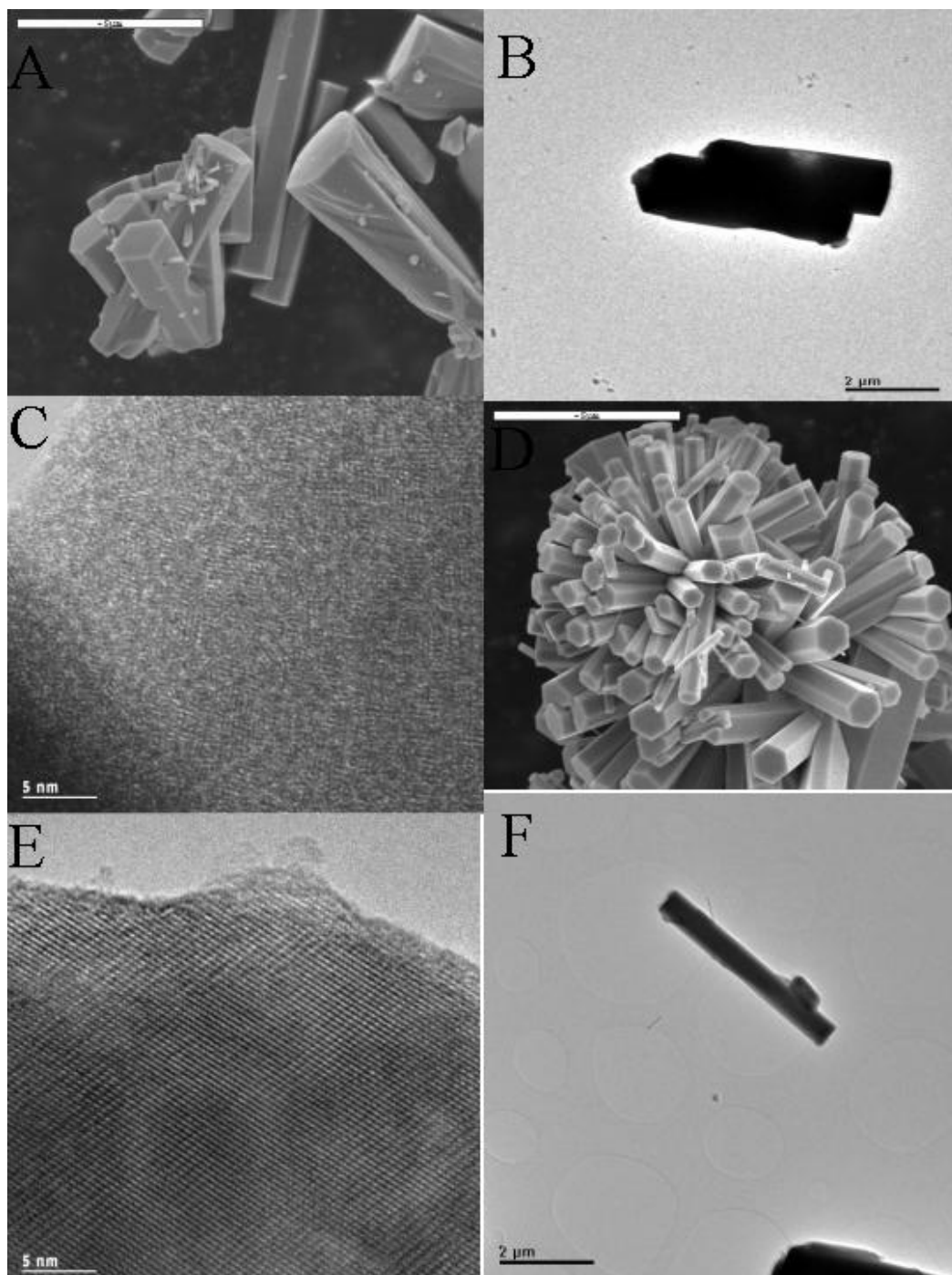
Figure 2.11: A) SEM of hexagonal MoO₃, 227; B) TEM, 227; C) HRTEM, 227; D) SEM, 130 large scale; E) HRTEM of 130; F) TEM 130
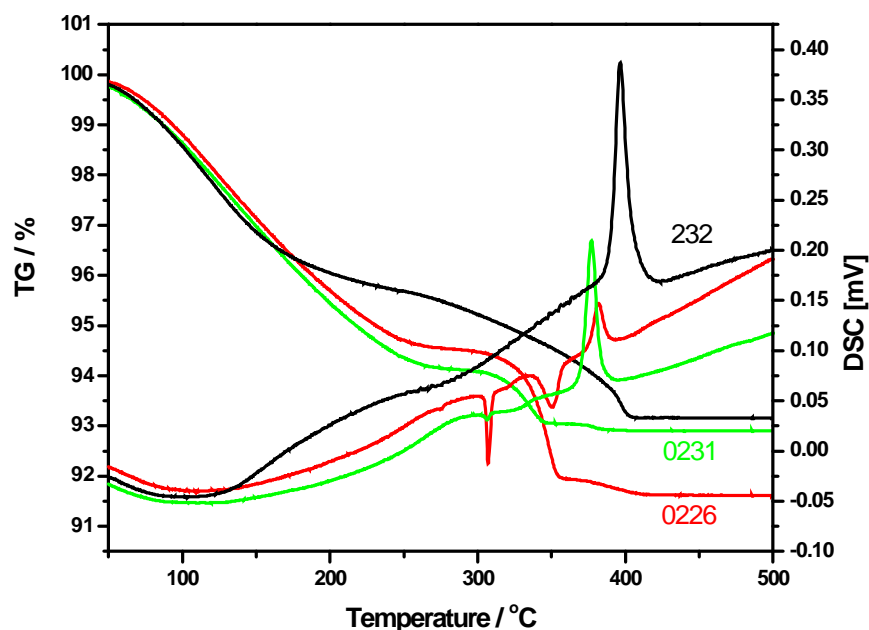
Figure 2.12: TG-DSC, sample 226, 231, 232

With the sodium-containing compound the 50 °C sample is showing the biggest mass loss (8.5 %) accompanied by a sharp endothermic signal at 350 °C (Fig. 2.12). All three samples show a sharp exothermic signal at 378 °C. A sharp endothermic signal is detected at 307 °C for the sample prepared at 30 °C and at 50 °C. The samples prepared at 30 °C and at 70 °C show a broad endothermic signal at 331 °C. The sample prepared at 30 °C evolves NO_X at 325 °C and at 380 °C. The 50 °C sample shows only one very large peak at 350 °C. The sample prepared at 70 °C looses NO_X at 340 °C and at 380 °C.

The potassium containing samples show a similar thermal behaviour. The overall mass loss of the sample prepared at 70 °C is 5 % and it is 6 % of the sample prepared at 50 °C. The TG-trace shows a step at around 100 °C. In between 190 °C and 320 °C the samples prepared at 50 °C and 70 °C are fairly mass constant and their TG traces run almost parallel. At temperatures higher than 320 °C a rapid mass loss (2 %) sets in which is related to an exothermic signal in the DSC curve in the case of the sample prepared at 50 °C.

Simultaneously, a trace of water and NO_X is detected in the MS. The sample prepared at 70 °C does not show a clear step and no characteristic signals in the DSC trace. At around 350 °C the evolution of water and NO_X is detected when the final phase transition to orthorhombic MoO_3 sets in. The final phase transition is shifted to lower temperatures compared to the hexagonal phase prepared with ammonia as counter ion.

The compound obtained from AHM exhibit an overall mass loss of 7 %. At 400 °C an exothermic event is recorded coinciding with the evolution of water and NO_X and a small final mass loss (less than 1 %). The mass loss does not show clear steps and the MS traces water and NO_x continuously (Fig. 2.6).

In a separate experiment the sample was heated to the temperature of the exothermic event and left at this temperature for one hour. During this procedure the sample transformed into orthorhombic MoO_3.
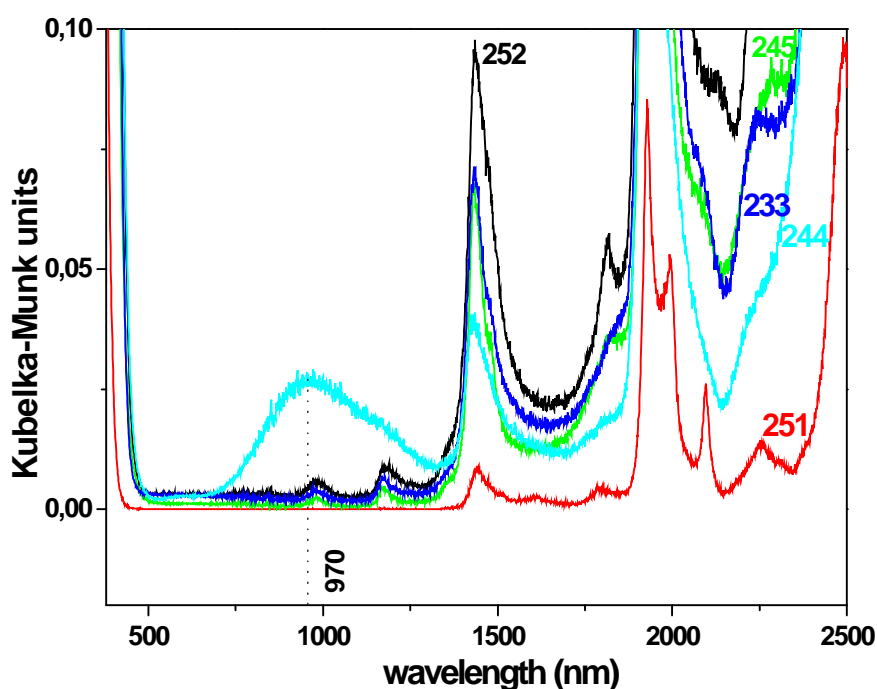
Figure 2.13: NIR bands of 252, 245, 233, 244, 251

SEM/TEM

The morphology of sample 227 is studied with SEM. A characteristic SEM of the sample is shown in Fig. 2.11 A, B, C. The sample consists of regular hexagonal rods with a length of several μm and a diameter ranging from 1-2 μm.

The particles reveal well-defined facets. However, smaller irregular particles are observed in the size range below 500 nm. The projected morphology of the hexagonal rods is recognised in TEM images such as Fig. 2.11.

The small particles are observed here as well. As the well-defined hexagonal shaped rods not are transparent for 200 keV electrons due to the thickness, lattice fringe imaging is concentrated on the small irregular shaped particles.
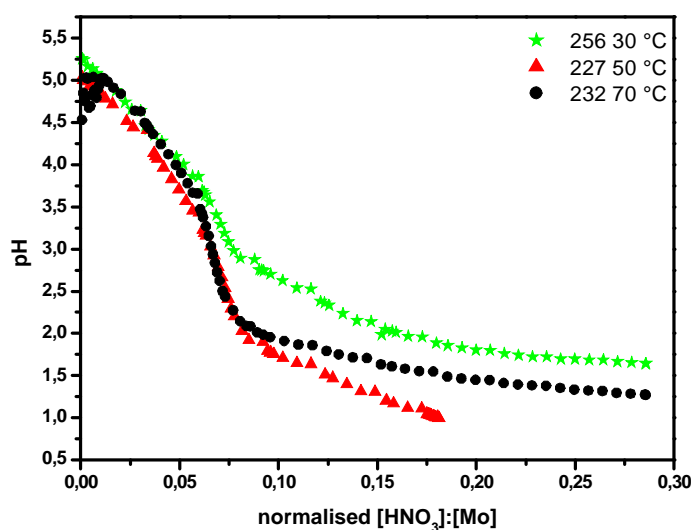
Figure 2.14: pH trace of 256, 227, 232. Data normalised to molybdenum and acid concentration respectively

In Fig. 2.11 a characteristic high-resolution image of the small, electron transparent agglomerates is shown. Randomly oriented clusters of molybdenum oxide reveal lattice fringes separated by characteristic distances of 0.34 nm and 0.37 nm. The whole area depicted in Fig. 2.11 seems to be crystalline but it is clear that it is an agglomerate rather than a single crystal.

TPRS

The most active material in this family is produced from the ammonium containing precursor. CO_2 production sets in at 330 °C. A decisive rise in activity is monitored at 420 °C. At 450 °C another plateau is reached and at 480 °C a maximum in activity is reached. The same material starts to produce acrolein at around 350 °C. The activity is rising with temperature only a small bend in the trace is observed at 370 °C (Fig. 2.20, Fig. 2.21, Fig. 2.22, Fig. 2.23).

The catalytic behaviour of the sodium containing hexagonal MoO_3 is much lower. However the first activity is registered at a quite low temperature 250 °C. At 330 °C and at 350 °C two local maxima are observed in a comparatively shallow trace. The maximum activity is found at 480 °C.
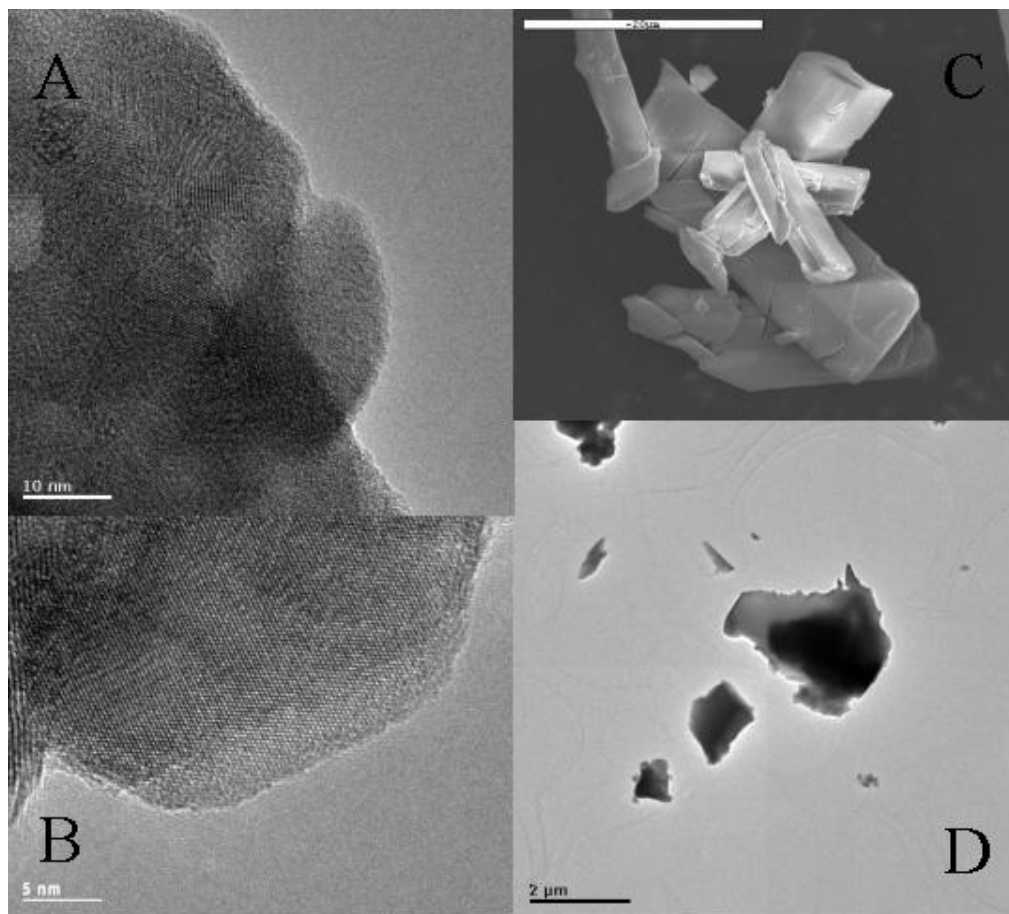
Figure 2.15: A) HRTEM, 74; B) HRTEM, 74; C) SEM, 74, D) TEM, 74

The potassium containing compound shows a very similar behaviour however the first local maximum is more pronounced and the second one is missing.

2.3.4 $Mo_{36}O_{112}^{8-}$ supramolecular molybdenum oxide

The supramolecular compound is obtained with ammonia or with potassium as counter ion. Usually low temperatures and high molybdenum concentrations need to be employed (sample 256, 257, 228, 258, 225, 223, 249, 250, 245, 253, 246).

Using potassium as counter ion the supramolecular compound is obtained with K_2MoO_4 0.28 mol/l and HNO_3 2.0 mol/l at 30 °C, K_2MoO_4 yields the supramolecular compound at 30 °C and at 50 °C the same is true when the acid concentration is increased to 5 mol/l.

Ammonia as counter ion (Fig. 2.14) yields the supramolecular phase when AHM 0.7 mol/l and HNO_3 1 mol/l is used at 30 °C. From a 1 mol/l AHM solution this phase is precipitated at 50 °C. Employing a 0.7 mol/l AHM solution and HNO_3 2 mol/l $Mo_{36}O_{112}^{8-}$ is obtained at 50 °C.
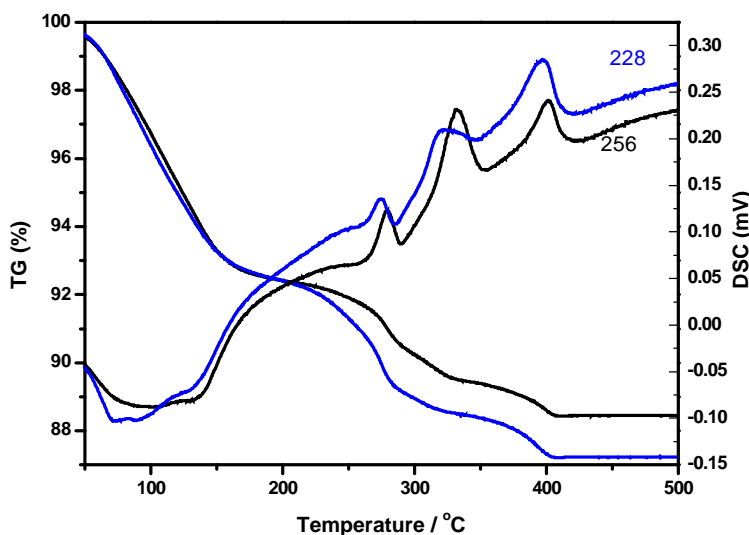
Figure 2.16: TG-DSC of 256 and 228

pH dependency

Using the 0.28 mol/l K_2MoO_4 at 30 °C the reaction starts at pH = 7. The titration curve is similar to the one leading to hexagonal MoO_3 with this concentration. However, in this case much more acid is needed to reach the final pH. The titration curves of the 2 mol/l solution titrated with the 2 mol/l HNO_3 start at pH = 7.5. The buffering regime at around pH = 7 is quite extensive and roughly the same amount of acid is needed to reach the final pH. The same shape is observed for the case 2 mol/l K_2MoO_4 5 mol/l HNO_3. The reaction at 30 °C needs less acid than the one at 50 °C to reach the final pH (Fig. 2.18).

With ammonia as counter ion (AHM 0.7 mol/l, HNO_3 1 mol/l) the reaction starts at pH = 5.3, the first buffering is less extensive and a comparatively big amount of acid is used. In principle the same applies for the other reactions (Fig. 2.14 and 2.19).

XRD

The supramolecular compounds obtained all showed a variety of signals in the early 2 theta range, all similar to the original single crystal pattern from Böschen *et al.* [32]. No sample matched that pattern exactly; the differences in the powder patterns could arise from different amounts of crystal water present in the precipitates.
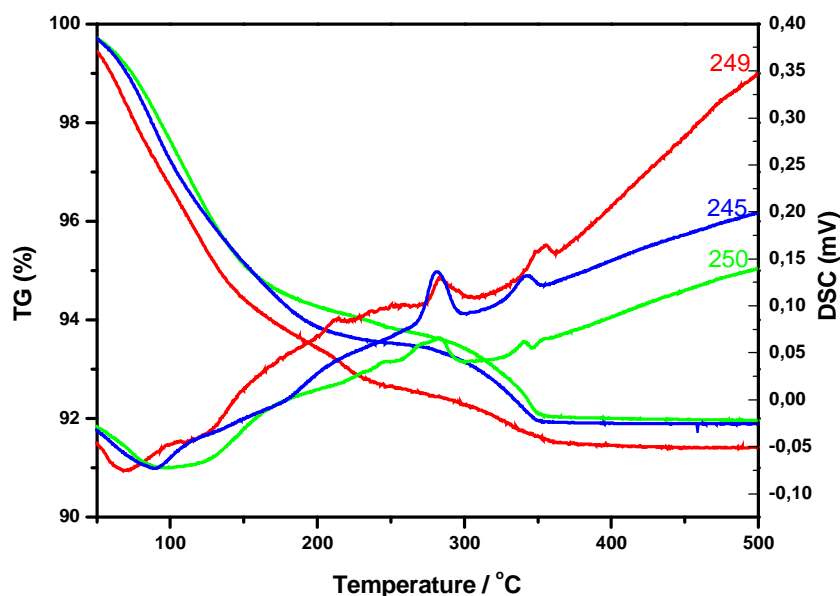
Figure 2.17: TG-DSC trace of 250, 245 and 249

In the potassium case one needs to distinguish among the products obtained from high and from low concentrations. Whilst the low concentration product shows the 100 % signal at 7 2 theta, the other products show various signals in this region and a 100 % signal is difficult to determine (details Fig. 2.4).

Raman

The bands for the potassium-containing product are situated at 963, 882, 373 and 229 cm^{-1} for the low concentration product. Compared to that the bands for the high concentration product are slightly shifted (961, 898, 372 and 240 cm^{-1}). However the differences in band shape and relative band intensities are even more decisive.

The ammonia-containing product shows bands at: 983, 959, 889, 372 and 234 cm^{-1}. This is in line with the bands reported in the literature. The samples show a large variation in relative band intensities in the region assigned to the terminal Mo=O stretching frequencies (Fig. 2.5).

DRIFTS
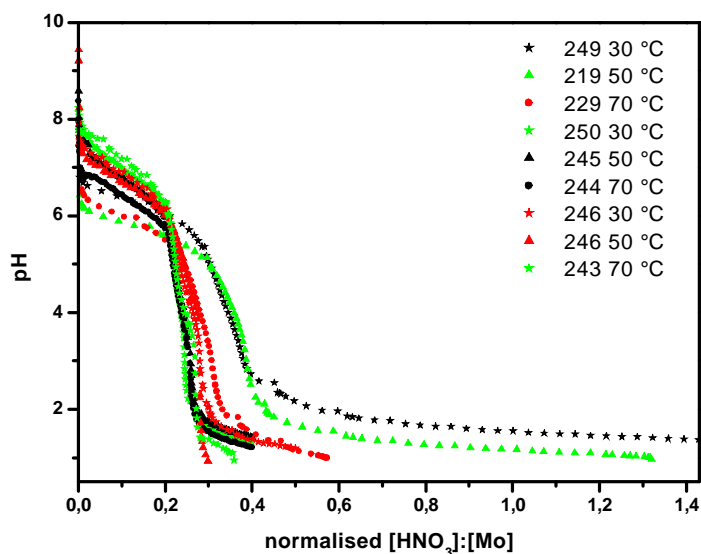
Figure 2.18: pH-trace 249, 219, 229; 253, 246, 243; 250, 245, 244. Data normalised to molybdenum and acid concentration respectively

Again small shifts depending on the counter ion are observed: 596, 658, 715, 818, 942, 967, 987, 1305, 1412, 1619, 3579 cm^{-1} (Fig. 2.9 and 2.10).

UV/Vis NIR

Looking at the NIR spectrum (Fig. 2.13) of the experiment carried out with the 2 (0.28) mol/l K$_2$MoO$_4$ solution and the 2 (5) mol/l HNO$_3$ it is to be seen that the compound prepared at 50 (30)°C shows in Table 2.5 the most intense water (NIR) bands at 1435 nm and at 1935 nm. The compound prepared at 30 °C exhibits slightly smaller bands. Band gap energies are is 3.30 eV and 3.30 eV. Switching from a 2 (0.28) mol/l acid (K$_2$MoO$_4$) to a 5 mol/l the water (NIR) bands do not change their behaviour and are still almost located at the same wavelengths. The band gap energy of both samples is found at 3.43 eV.
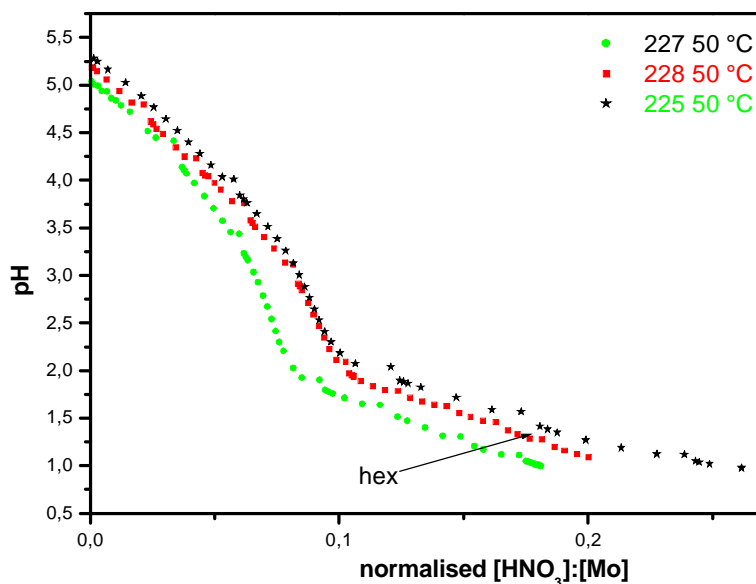
Figure 2.19: pH trace, 227, 228, 225. Data normalised to molybdenum and acid concentration respectively

For the compound prepared from 0.7 and 1 mol/l AHM bands in the NIR region are located at 1440, 1570, 1945, 2040 and 2150 nm. The first band, the third and the fourth are assigned to a surface OH group the second to H_2O and the last band is caused by ammonia. The LMCT band is blue shifted from 316 to 308 nm with increasing AHM concentration and the band gap energy is 3.46 eV (0.7 mo/l AHM) and 3.55 eV (1 mol/l AHM) as shown in Table 2.5.

Thermal Analysis

The supramolecular phase prepared at 30 °C (0.28 mol/l K_2MoO_4, HNO_3 2 mol/l) shows only two sharp steps in the TG-trace (100 °C, 322 °C), the overall mass loss is around 8 % (Fig. 2.17). The DSC curve indicates three small exothermic peaks at 213 °C, 286 °C and 355 °C. At the endothermic signal and the shoulder in the 100 °C region H_2O and OH is detected by MS. The occurrence of the first exothermic peak at 213 °C is linked with the evolution of OH and H_2O. Between the two signals at 286 °C and 355 °C (at 344 °C) a NO_X signal is detected by MS.

When the same experiment (Fig. 2.17) is performed with a solution containing 2 mol/l K_2MoO_4 the two supramolecular phases obtained at 30 °C and at 50 °C show almost identical TG traces (overall mass loss 8 %). Water is removed at 100 °C and this coincides exactly with the appearance of the endothermic signal including the shoulder, between 200 and 300 °C a creeping mass loss is detected. Another peak assigned to NO_X in the MS is detected at around 340 °C. After 350 °C mass constancy was

achieved. The 50 °C sample shows two distinct exothermic signals at 281 °C and at 343 °C. The gases evolved are the same as in the previous case and at the same temperatures. The 30 °C sample shows signals at the same positions but less distinct.

The same experiment is carried out only with a higher HNO_3 concentration of 5 mol/l. The TG-traces of the two supramolecular compounds are very similar to the ones described in the preceding paragraph. However the total mass loss of the sample prepared at 30 °C is comparatively high: 12 %. The sample prepared at 50 °C looses 10 % of its mass. Both samples show a broad endothermic DSC signal at 100 °C where water is released. At 130 °C both samples show a sharp endothermic signal, which is unrelated to any mass loss. At 278 °C an exothermic mass loss is detected and only at the endothermic signal at 340 °C a final mass loss is observed setting NO_X free.
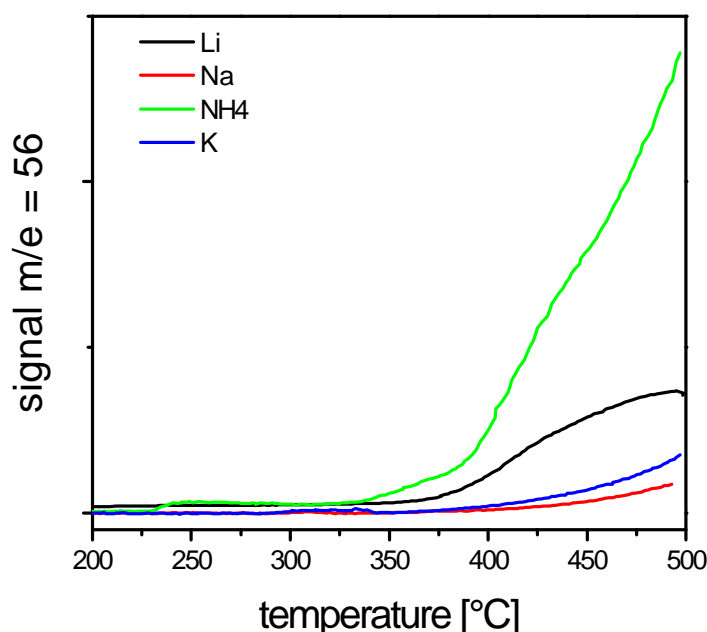
Figure 2.20: TPRS first cycle; showing the effect of counter ions in acrolein production

The compound obtained from the AHM solution 0.7 mol/l shows an endothermic event at around 100 °C, when a large amount of water is removed from the sample (ca. 7 %). After that a sequence of three exothermic events is registered at 279 °C, 332 °C and at 400 °C. Each of them connected with a mass loss and at each of them water and NOx are evolved. Total mass loss is 12 % (Fig. 2.16).

In a separate experiment samples were heated to the temperature of each event and then the temperature was kept constant for one hour. After this the sample was investigated

by Raman spectroscopy. It turned out that the supramolecular phase is transformed into hexagonal MoO_3 after the first exothermic event at 279 °C. No change in phase is observed after 332 °C. At 400 °C it transformed into orthorhombic MoO_3.

SEM/TEM

A representative SEM image is shown in Fig. 2.15 C. The particles observed in the SEM images are typically between 1 and 5 µm and show an elongated shape with facets. However, the facets are not perfect and some irregularities are observed. The molybdenum to oxygen ratio is found to be close to constant over the sample by EDX analysis (not shown here).

The SEM images reveal some smaller features (tenths of µm). These features are more visible in TEM images. In Fig. 2.15 D such an image is shown. The large somewhat irregular shaped particles are observed in projection in the images. Moreover is the carbon film covered with small (<200 nm) agglomerates.
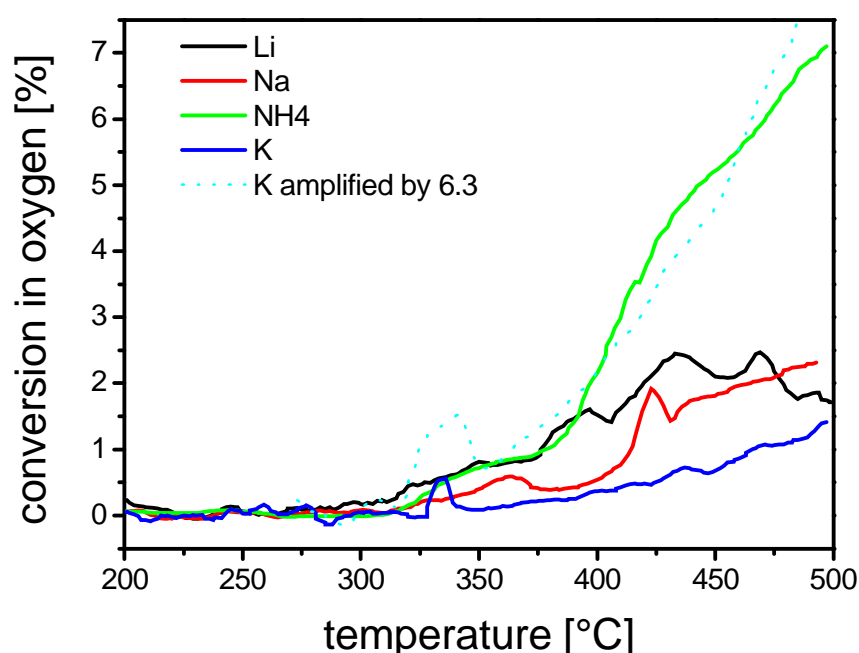
Figure 2.21: TPRS first cycle; showing the effect of counter ions in oxygen conversion

A typical high-resolution image of the small agglomerates is shown in Fig. 2.15 A and B. The image shows the sample consisting of small randomly oriented clusters revealing

lattice fringes encapsulated by amorphous/non-crystalline material. The lattice fringes are separated with a characteristic distance of 0.37 nm.

TPRS
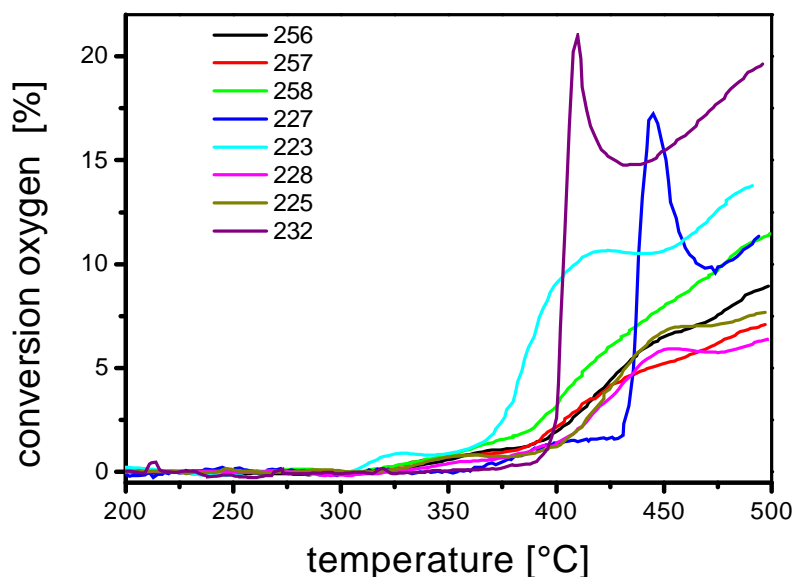
Figure 2.22: TPRS run first cycle; showing compounds prepared from AHM starting material; oxygen conversion

The most active material prepared for this investigation is the supramolecular compound (Fig. 2.22 and Fig. 2.23). Its CO_2 trace is characterised by a rather sharp local maximum at 230 °C. Catalytic activity rises steeply at 380 °C. Another local maximum at quite high level is observed at 430 °C. The highest overall activity towards CO_2 is seen at the end of the heating ramp.

Acrolein production starts at 380 °C and no preceding local maximum is observed. At 430 °C a turning point in the trace is observed. The maximum activity toward CO_2 is registered at the end of the heating ramp.

2.3.5 Up scaling

Preparation and pH-dependency

The hexagonal phase and the supramolecular phase were also synthesised in a 4 l reactor in order to test the effects of up scaling. The pH curves of two supramolecular samples that were precipitated in the different reactors under otherwise identical conditions display a very similar behaviour up to pH = 3, further down the `small scale´ sample showed an increased buffering region that can be associated with protonation reactions. After the titration the `large scale´ sample was allowed to age, as mentioned above. The Raman spectra showed identical positions for all major bands. XRD analysis showed both the characteristic signal for the supramolecular phase at 7 degrees 2 theta, but each sample showed a number of foreign signals.

Electron Microscopy and Electron Diffraction

Well-defined rods are observed in typical TEM images Fig. 2.11 of the hexagonal material obtained by the up scaling experiments. The typical hexagonal rods are around 5 µm in length and 0.5 µm wide. Smaller agglomerates are observed as well in the SEM images. However, the amount is much less than the amount observed in sample 227. The mixture of big and small rods is clearly visible in TEM images such as Fig. 2.11. The size of the big rod in Fig. 2.11 is 0.6 µm times 4.3 µm. The small rod located below the big one in Fig. 2.11 has the dimension 50 nm times 400 nm, corresponding to a volume approximately 1500 times less than the big rod. Lattice fringe imaging of the suitable particles shows big (>50 nm) regular crystals. A typical example of such a lattice fringe image is shown in Fig. 2.11. An FFT of the image is shown in Fig. 2.15. The dominant lattice fringes are separated with distances of 0.61 nm and 0.36 nm, respectively, in an angle of 70º. The outermost 0.5-1 nm do not show the same lattice fringes as the inner parts of the crystals.

The supramolecular particles obtained during the up scaling experiments (sample 74) are more regular shaped for the large precipitation batch sample compared to the small scale samples. This is observed in both SEM and TEM images. A characteristic TEM image of sample 74 is shown in Fig. 2.11. Both large (>1 µm) and small (<200 µm) agglomerates are observed in the images. However, the amount of smaller agglomerates

seems to be smaller and the shape better defined compared to sample prepared on a smaller scale.

HRTEM images of the smaller agglomerates found in sample 74 reveal randomly oriented 3-5 nm clusters embedded in non-crystalline material as shown in Fig. 2.11. The distance between the lattice fringes revealed in the clusters are found to 0.34 nm and 0.37 nm. The clusters seem to be more well-developed in this sample than in the small scale sample and the non-crystalline material less. Furthermore, larger (20-50 nm) well-crystalline particles are observed in the sample Fig. 2.11. A Fourier Transform of the crystal in shown in Fig. 2.15. The main features in the FFT correspond to lattice fringe distances of 0.53 nm and 0.40 nm in an angle of 40°. The outermost 0.5 nm of the crystal shown in Fig. 2.11 is observed to be a different structure than the rest of the crystal.

TPRS
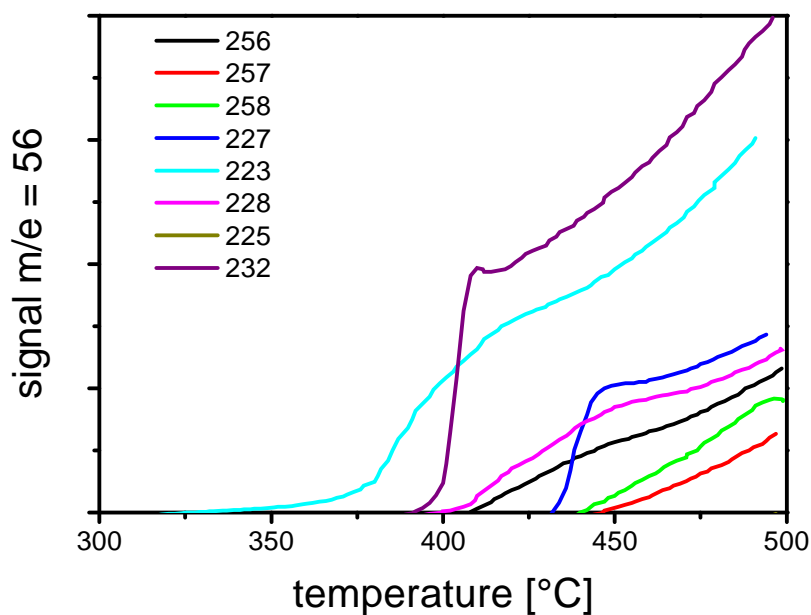
Figure 2.23: TPRS run first cycle; showing compounds prepared from AHM starting material; acrolein production

Two samples prepared under similar conditions are compared (Fig. 2.24). In both cases a 1 mol/l AHM stem solution was used and HNO_3 1 mol/l. The large scale sample was produced under preparative conditions including a 1 h aging time.

Looking at the CO_2 production the preceding local maximum is slightly shifted. Apart from that the two traces match exactly until 250 °C are reached. From that point on the large scale's trace is steeper and shows a marked plateau at 320 °C. The overall maximum is higher but reached at the same temperature. After that the activity towards CO_2 is declining. From 330 °C onwards the two traces match again. During the second cycle the activity is in the same range as at the end of the first one. However the activity of the small scale sample is higher.
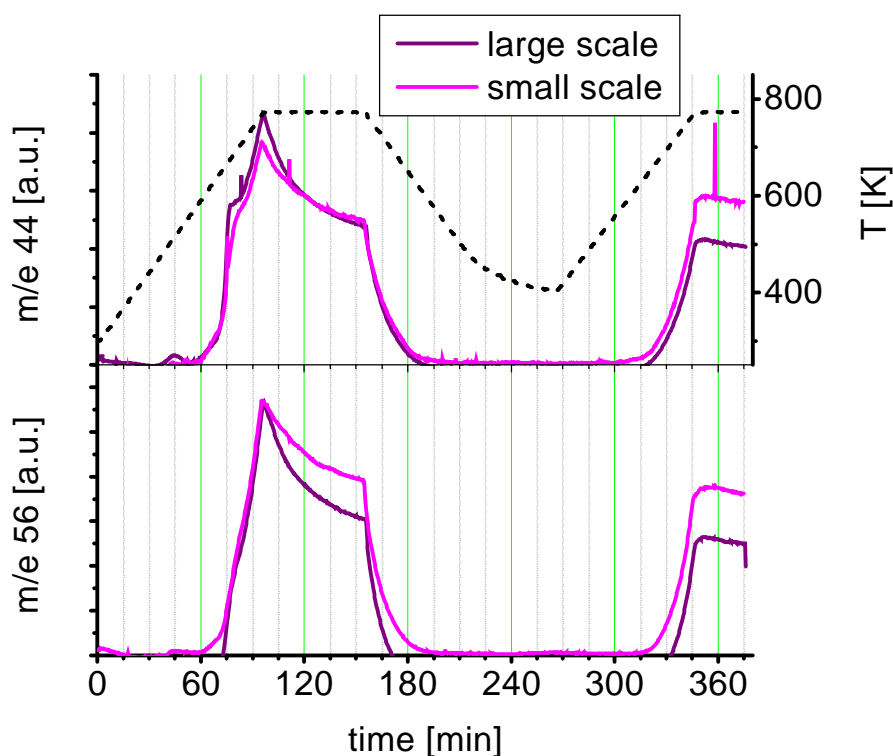
Figure 2.24: TPRS first and second cycle; showing the activity and selectivity of the large scale sample and the small scale sample

In the acrolein case the two traces match until the first maximum is reached. During the constant temperature period the large scale sample is declining faster. In the second cycle the range of activity is comparable to the end of the first one and again the small scale sample is more active than the large scale.

2.4 DISCUSSION

Principally the herein described method allows producing four different families of materials in a controlled manner. The assignment is based on integrative methods such as Raman spectroscopy and XRD. TEM shows that every sample contains differently sized and shaped particles with a high content of amorphous material. This is particularly important to be considered for any efforts to derive structure activity correlations. The presence of a non-uniform precipitate is easily understandable bearing in mind the multitude of parallel reactions that occur during the titration. An earlier
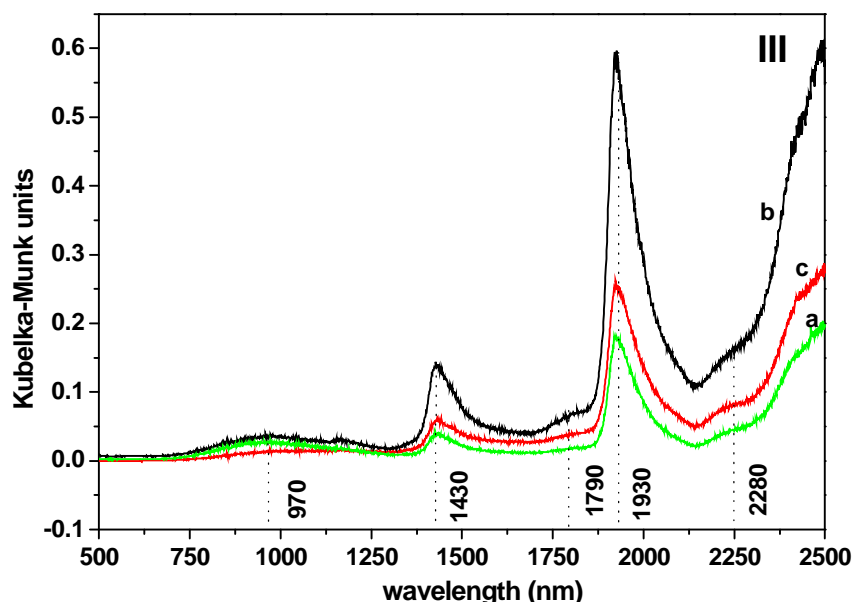
Figure 2.25: Spectroscopic characteristics NIR of orthorhombic
MoO_3 . 251, 222 and 230

Raman investigation[29] already identified two independent reactions, more are likely. A closer look at the Raman bands show identical band positions for each member of the same family but different intensities, again indicating the presence of more than one species. Another indicator for this is the band gap energies determined from the UV/Vis experiments. This is most likely one of the reasons of many contradictions in the literature concerning these materials.
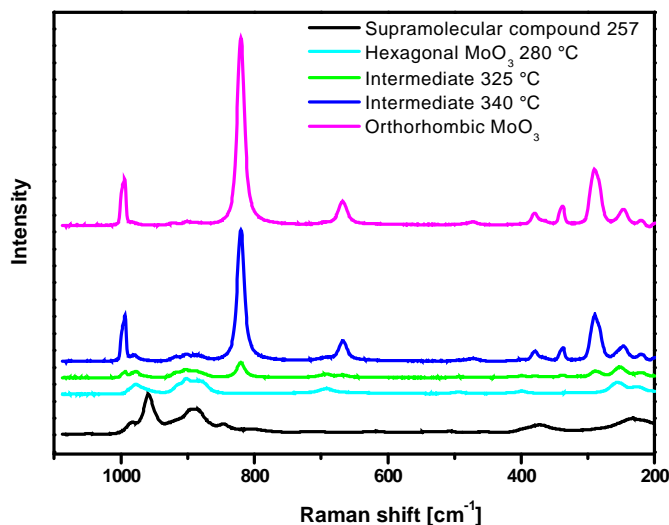
Figure 2.26: Raman investigation of TG post mortem samples at characteristic signals

MoO$_x$ spectra show NIR bands with different intensities, distinguishable LMCT bands and band gap energies (Eg) at RT. Based on the exact determination of such spectroscopic characteristics the following LMCT bands (nm) (I) and Eg's (eV) (II) are attributed to the above mentioned MoO$_x$ families: (I) 312 (NH$_4^+$), 319 (K$^+$); (II) 3.50 (NH$_4^+$), 3.43 (K$^+$) to supramolecular Mo$_{36}$; (I) 313 (NH$_4^+$), 312 (K$^+$), 327 (Na$^+$); (II) 3.35 (NH$_4^+$); 3.30 (K$^+$), 3.27 (Na$^+$) to hexagonal MoO$_3$; (I) 296 (Li$^+$); (II) 3.44 (Li$^+$) to orthorhombic MoO$_3$ and (I) 284 (K$^+$); (II) 3.77 (K$^+$) to trimolybdate MoO$_x$.

From a blue shift of the LMCT band in the series supramolecular/hexagonal $\rightarrow$ orthorhombic $\rightarrow$ trimolybdate and a decreasing broadening of this band it may be concluded that the cluster size decreases. All MoO$_x$ samples evolved NIR bands at 1435, 1940, and 2040 nm. They are assignable to an overtone mode of the OH stretching vibration and a combination mode of the OH stretching and bending vibration, respectively. Other NIR bands, e.g. those detected in MoO$_x$ samples prepared from AHM at 1570 and 2150 are caused by ammonia.

2.4.1 Effect of counter cation

Despite the inhomogeneity mentioned above, this work has clearly shown the considerable structure directing effects of counter cation. The influence of the counter cation is based on its size and other properties such as activity and ionic strength. Whilst only the big ions K^+ and NH_4^+ caused spontaneous precipitation, the presence of Li^+ and Na^+ required a heating period, leading to orthorhombic MoO_3 in case of Li^+ and to hexagonal MoO_3 in case of Na^+. The latter structure was initially reported by Krebs[31;83] and labeled as Mo_5O_{16}. Heating of K^+ and NH_4^+ containing material yields either the trimolybdate[43;78] or the hexagonal MoO_3 whereas ammonia yields only supramolecular or hexagonal MoO_3, as reported.

In order to assess the thermodynamic stability of the four different families it is assumed that there is the same general trend in solution and in solid material. Wienold *et al.*[84] carried out thermal decomposition of ammonium heptamolybdate. They showed that in kinetically determined steps the system turned into hexagonal MoO_3 and subsequently into orthorhombic MoO_3 at 350^oC. The last step was identified as thermodynamically favoured. If the formation of orthorhombic MoO_3 is also thermodynamically favourable in solution, the Na^+, K^+ and NH_4^+ counter cations prevent such formation by precipitation of other intermediate phases. Formation of such other phases would also be kinetically controlled, as also indicated by the large temperature dependence. As Li^+ is not able to force the precipitation of the hexagonal phase because of its lower activity the orthorhombic phase is formed.

In order to address the question about the role of the counter cations during the precipitation process Lehn´s definition of supramolecular chemistry as `chemistry beyond the molecule´ intermolecular forces such as van der Waals forces, London dispersion forces and hydrogen bonding becomes important. Further polarisability introduced in the HSAB concept needs to be applied. It is likely that the comparatively soft NH_4^+ could serve as an endo-template [85;86]. Fragments of the Octamolybdate will group around the ammonia and interlink. As soon as the particle size is big enough and a certain amount of species is formed, the solubility product is exceeded and precipitation of the hexagonal MoO_3 sets in[86]. A retro synthetic approach corroborates to this idea. Taking the ammonia inside the channel as a centre, only a few Mo-O-Mo bridges need to be broken to yield these nanocluster building blocks. A comparable mechanism should be possible with K^+, taking into account that this ion is very similar

in size and ionic strength to ammonia. However K^+ seems to be the limit for this mechanism because under some experimental conditions (high Mo concentration, high acid concentration, 70 °C and spontaneous precipitation) the layered trimolybdate structure is obtained. This trend is further followed as the smaller and harder ions Na^+ and Li^+ do not cause spontaneous precipitation, but rather hexagonal/ orthorhombic MoO_3 is formed after heating, as reported above. The smaller the ion the more difficult it becomes to build up a stable spherical wrapping, consequently layered structures are obtained from smaller ions and channel structures from bigger ones.

2.4.2 Effect of temperature and proton to molybdenum ratio

The obtained results show that temperature and the proton to molybdenum ratio are also important control variables. 50 °C is the most important boundary as the temperature dependent investigations show. Therefore at this temperature most likely the reaction mechanism is changing. High molybdenum concentrations and low temperature (30 °C) lead to a spontaneous precipitation of a supramolecular compound, which is very similar to the $Mo_{36}O_{112}$ reported by Krebs. Low concentration and high temperature leads to the formation of a hexagonal MoO_3[79-81] the same structure is reported by Krebs[83;87] and labelled as Mo_5O_{16}, orthorhombic MoO_3 or trimolybdate depending on the counter ion.

Up to pH = 3.5 the curves are identical and therefore the reaction mechanisms are alike. This seems to be plausible because at this stage most likely protonation of the heptamolybdate is taking place. This fits nicely to NMR data[67]. At around pH = 3 where the reorganization to the $Mo_{36}O_{112}$ sets in, the 30 °C curve is different to the other curves. Octamolybdate is reported to be the dominant species [63;65;88] [44;68;89] in this pH region. As transformation from octamolybdate into $Mo_{36}O_{112}$ requires many bonds to be broken and reassembled by polycondensation reactions the slow down in the pH drop seems plausible. At around pH = 2 another change in mechanism sets in. The 50 °C sample is acidified easily without yielding a precipitate. The 70 °C moves parallel to the 30 °C sample however at lower pH. It is likely that 50 °C is not enough to overcome the activation energy barrier to precipitate the hexagonal phase.

Using K_2MoO_4 as starting compound the coordination of the Mo is tetrahedral and the experiment starts at higher pH. As the curves show the starting pH is a function of the molybdenum concentration. As the first pH drop is very rapid the tetrahedral species is

not to be protonated. The first buffering region probably coincides with the formation of a heptamolybdate species. Again this event depends on molybdenum concentration. The following reaction pathway will be similar to the one described with ammonia as counter ion. It is noteworthy that trimolybdate is only obtained with high molybdenum and acid concentrations at higher temperatures.

According to Tytko the $Mo_{36}O_{112}$ is the major compound in solution at low pH and precipitates as soon as the solubility product is reached. It is remarkable that the connectivity has changed compared to the starting material[42]. In the AHM precursor only corner sharing octahedra are observed. In the $Mo_{36}O_{112}$ edge sharing connectivity prevails and the pentagonal bipyramid as structural motif, which appears in catalytic active material like Mo_5O_{14}, is formed[20;90;91]. Corner sharing also turns up in the hexagonal MoO_3.

2.4.3 Effect of water

Krebs points out that $Mo_{36}O_{112}$ is only stable in the mother liquor. Water is responsible for the hydrogen bonding which is probably the dominating coherent force in this molecule[32]. This phenomenon has been studied in detail in comparable compounds[54;86]. As soon as water is removed the compound will decompose. This explains the variation in XRD. Nevertheless the close similarity of the XRD to the reference and the exact agreement of the Raman band positions corroborates to the idea that the main structural motives prevail.

Investigating the reaction in the solid phase again the differences due to counter ions are striking. Using ammonia as a counter ion, the final transformation is taking place at 50 °C higher temperatures than in the potassium case. Therefore solid-state thermodynamics are clearly influenced by the nature of the counter ion.

Moreover the phase transformation using ammonia as counter ion will be very different because of the combustion of the ion. The large amount of water released at the first exothermic event is probably to some extend related to this combustion. The same holds true for the exothermic DSC signal. A good deal of heat is produced because of the combustion.

As NO_x is released at 3 different temperatures showing three clearly distinguishable DSC and MS peaks (water and NO_x data not shown) it is probably situated in two

different places. At the first event the ammonia serving as linker between supramolecular building blocks will be removed. After that ammonia is situated in the channels of the hexagonal MoO_3 and will only be removed at higher temperatures. The last NO signal is detected with the K^+ containing compounds as well. At this temperature the NO_3^- that was brought into the solution by the nitric acid is removed.

As a mass loss is detected in this region as well it is very likely that the phase transformation form the hexagonal phase to the orthorhombic MoO_3 is related to a removal of oxygen from the lattice or a further condensation. This idea is further supported by traces of water that are also detected.

Comparing the supramolecular compound obtained with K^+ as counter ion with the ammonia containing compound it becomes clear that the first transformation is also a condensation step. The water being released in this step by the K^+ containing compound cannot originate from a combustion process but from polycondensation. In this respect solid phase and aqueous chemistry run parallel because some activation barrier needs to be overcome to induce this process.

The similarities between the supramolecular phase and the hexagonal MoO_3 become very clear when the sample prepared from a 2 mol/l K_2MoO_4 solution is compared to the sample prepared from a 0.28 mol/l K_2MoO_4 solution. Mass loss and DSC trace are very similar. Therefore only the condensation process will vary slightly.

The water contents can be estimated from the NIR bands and from the TG-MS results for the Li^+, Na^+ and K^+ containing precursors. Compounds, which show a big mass loss, always have marked water bands. This correlation is not possible for the ammonia containing samples because the water and ammonia vibrations are combined.

The XRD pattern of the orthorhombic MoO_3 obtained from Li_2MoO_4 shows broad signals and a comparatively high background indicating low crystallinity. One reason for this is that the degree of polymerisation due to a condensation in water at the chosen conditions is too low to form big crystalline particles or the solubility product is reached too early. DSC and TG-MS clearly shows an ongoing polycondensation.

The sample prepared at 50 °C shows the biggest overall mass loss concerning water. However the first step where only associated water is removed is biggest as well. One reason for this is probably a high degree of protonation at the outer shell of the polymeric precursor in solution being a good docking place for hydrogen bonding to water molecules. Assuming that the second step is the water from the polycondensation

process the 50 °C sample looses 2.9 % in this step. For the 30 °C sample the same amount is calculated. Only for the 70 °C sample 3.2 % are calculated. Therefore in this sample more OH groups suitable for further condensation were created. Again a change in the reaction mechanism can be established.

Taking all these results together it can be concluded that at higher temperatures in solution the sites for protonation are changing and protonation is much more efficient. This idea is corroborated by the above described changes in the pH curves of the ammonia containing samples as a function of temperature.

2.4.4 Structure determination by XRD and TEM

Phase characterisation of materials by XRD is widely used. However, such integral techniques are insufficient to reveal the detailed local phase- and structure determination, which might be relevant for the purposes of the studied material, especially in catalysis. Lattice fringe images of sample 130, such as Fig. 2.11 show well-developed crystals, from which the relevant lattice plane distances can be measured. Several high-resolution images revealing lattice fringes acquired from sample 130 are analysed, and the measured lattice plane distances are compared with the corresponding XRD pattern. This is shown in Fig. 2.15 C. The XRD shows narrow distinct peaks coinciding with diffraction peaks calculated from the model structure of hexagonal molybdenum trioxide. The signal to noise ratio is very high and no additional features are observed between the well-defined peaks. The observed lattice plane distances measured in the high-resolution images are marked under the XRD pattern in Fig. 2.15 C. HRTEM images cannot and should not be used quantitatively, so the comparison is done qualitatively. Several lattice plane distances observed in the HRTEM images are not revealed in the XRD, indicating that the HRTEM images are acquired of crystalline structures which are not resolved by the integral technique of XRD. In Fig. 2.11 both a very big particle and a small particle are observed. The volume of the bigger particle is approximately three orders of magnitude larger than the volume of the smaller one. The XRD technique is volume sensitive and hence the structure of the largest volume is favoured in the XRD. The diffraction pattern of the structure of the smaller crystals is suppressed by the diffraction pattern of the large volume of big well-defined crystals in the sample. The local structure of the smaller particles in the sample might be highly relevant for the resulting structure of the active

catalysts, and should not be neglected. In order to validate the comparison between X-ray diffraction and diffraction of electrons in the sample, diffraction simulations are performed using X-rays and electrons. The simulated powder diffraction spectra of the hexagonal molybdenum trioxide model reveal exactly the same features for electron diffraction and X-ray diffraction, although slight changes in the intensities are observed.

The morphology of the biggest particles in the samples shows clear differences in the two families (hexagonal and supramolecular). The regular hexagonal rods with well-
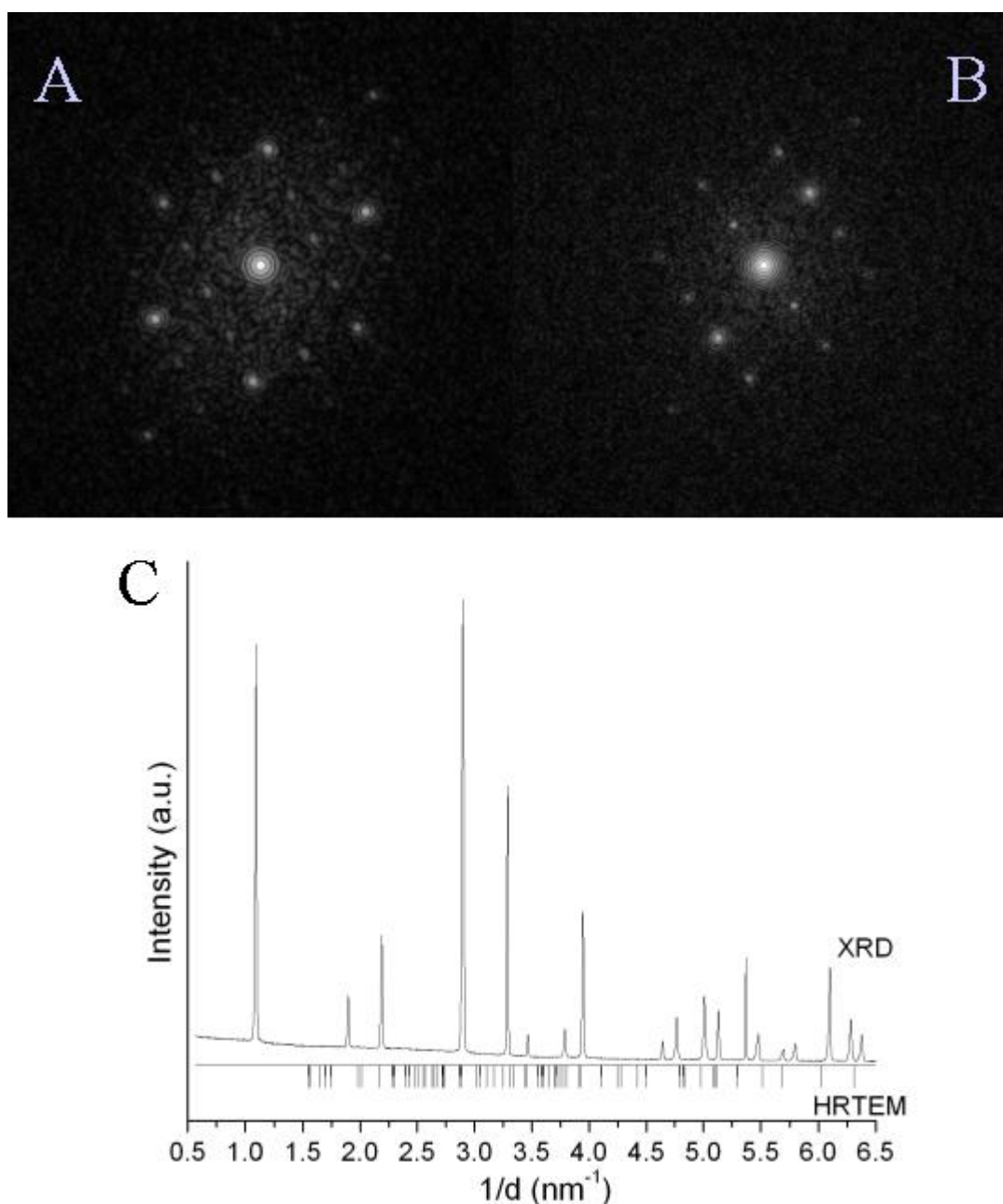
Figure 2.27: A FFT of 74, B FFT of 130, Comparison electron diffraction versus X-ray diffraction

defined facets observed in Fig. 2.11 are a further indication of the single crystalline hexagonal atomic structure of biggest particles in sample 227. The more irregular morphology of the largest particles observed in Fig. 2.11 might indicate a more complicated atomic structure or the fact that the biggest particles in the small scale sample are agglomerates of smaller crystals.

In the following the crystallographic structure of the studied samples will be discussed on the basis of the lattice fringe images acquired from area of the sample, which are electron transparent, i.e. thin agglomerates.

The samples precipitated in the small-scale set-up consist of randomly oriented clusters in the 3-5 nm scale, as shown in Fig. 2.11. The fact that lattice fringes are revealed indicates that the clusters are crystalline. The characteristic separations between the revealed lattice fringes are measured to 0.34 nm and 0.37 nm respectively. These separations coincide with the distance found between Mo atoms in edge-sharing and corner-sharing MoO_6 octahedra. The crystalline clusters in both sample 227 and the small scale sample are embedded in non-crystalline material, although this is more pronounced in the small scale. This non-crystalline material might very well contain the nitrogen, which is released during the activation of the catalyst. The clusters will then serve as building blocks for the final active structure of the catalyst.

Up scaling the precipitation process results in larger, more ordered crystalline structures. The structure shown in Fig. 2.11 is characteristic to sample 130 and shows a single crystal of more than 50 nm in size. Although the lattice fringe images acquired from sample 130 are insufficient to determine the structure of the crystalline material, it can be concluded that the resolved lattice fringes do not match the unit cell parameters of hexagonal or orthorhombic molybdenum trioxide. The outermost 0.5-1 nm of the single crystal do not reveal the well-defined lattice fringes found in the inner part of the crystal. This might be due to ill-defined lattice plane termination or to reconstruction at the surface due to oxygen vacancies caused by oxygen vaporisation into vacuum. The more ordered and bigger crystals are also observed in Fig. 2.11 A and B acquired from sample 74. The amount of non-crystalline material seems to be reduced in samples precipitated in bigger scale. Both sample 130 and sample 74 undergo longer aging times due to the up scaled precipitation, hence the system has more time to attempt the thermodynamically equilibrium state, resulting in larger more ordered structures.

2.4.5 Raman and DRIFTS

As Me-O distances and connectivity play an important role in the discussion of catalytic activity it is worthwhile having a closer look on Raman and DRIFTS. Starting with hexagonal MoO_3 (Fig. 2.28) with the point symmetry C_{6h} a band is reported at 976 cm^{-1}. This band is assigned to terminal Mo-O stretching $\nu(OMo)$; the bands at 904 cm^{-1} and at 889 cm^{-1} are assigned to bridging Mo-O-Mo $\nu(OMo_2)$ of corner sharing octahedra; the band at 691 cm^{-1} is assigned to a η 3 oxygen stretching frequency $\nu(OMo_3)$ of edge sharing octahedra; the bands at 494 cm^{-1}, 400 cm^{-1} and 317 cm^{-1} are assigned to the respective bending vibration $\delta(OMo_3)$; the band at 256 is assigned to the bending vibration $\delta(OMo)$. Finally the band at 224 cm^{-1} is assigned to $\delta(OMo_2)$.
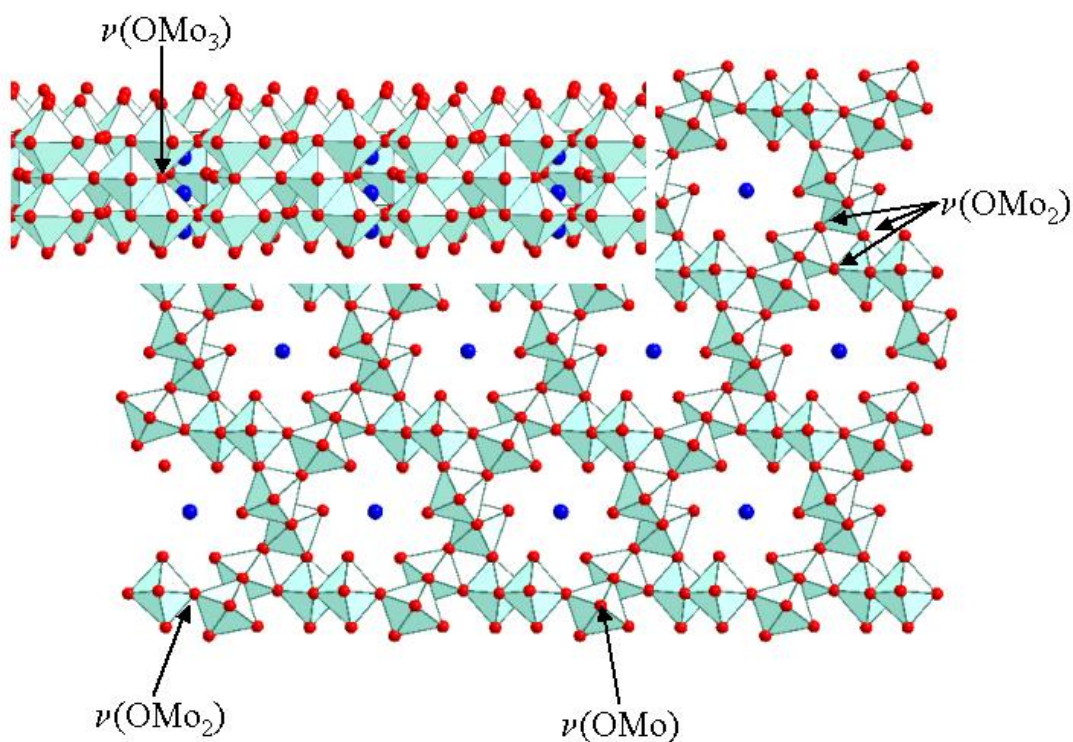
Figure 2.28: Hexagonal MoO_3, Assignment of Raman and IR modes

In orthorhombic MoO_3 with the point group D_{2h} the band assignment is as follows (Fig. 2.29). The band at 997 cm^{-1} is assigned to $\nu(OMo)$; the band at 824 cm^{-1} is assigned to $\nu(OMo_2)$; the bands at 668 cm^{-1}, 476 cm^{-1} and 379 cm^{-1} are assigned to $\nu(OMo_3)$; the band at 339 cm^{-1} is assigned to $\delta(OMo_3)$; the band at 291 cm^{-1} is assigned to $\delta(OMo)$; the band at 247 is assigned to $\delta(OMo_2)$[92-97].

IR bands were found at 743 cm^{-1} (not reported in the literature), at 840 cm^{-1} assigned to $\nu(OMo_2)$ and at 1000 cm^{-1} which is assigned to $\nu(OMo)$[98] [99;100]. Remarkably the Raman and IR-bands in orthorhombic MoO_3 are not equal. This could be explained by employing group theory. The space group is D_{2h} and in this case IR and Raman active modes do not coincide. Consequently Raman and IR excite totally different modes.
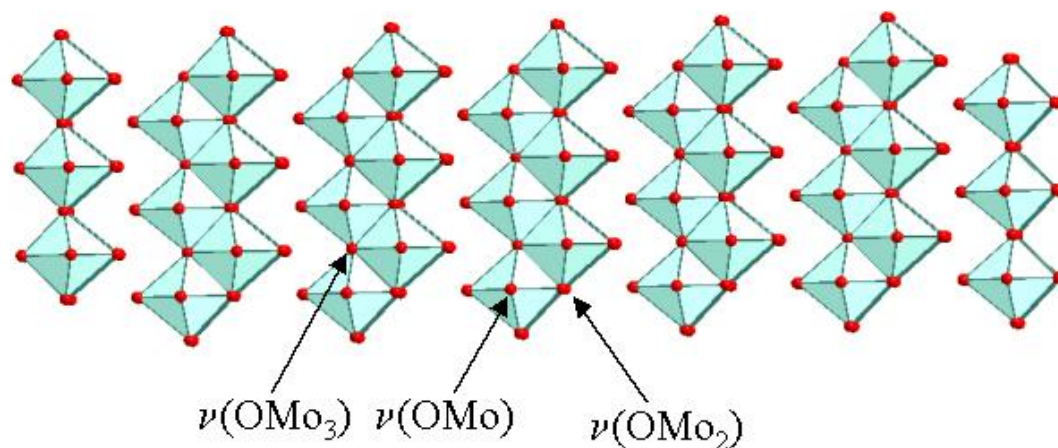
Figure 2.29: Orthorhombic MoO$_3$, Assignment of Raman and IR modes

2.4.6 TPRS

All tested molybdenum oxide samples show catalytic activity towards propene selective oxidation into acrolein, the degree of activity is strongly structure dependent. The main information of the TPRS can be extracted out of the traces emerging from the first heating. In this sequence, the precursor samples undergo decomposition and structural changes resulting from the thermal and atmospheric conditions they are exposed to.

The comparison of the samples under investigation elucidates the different activation (and deactivation) behaviour depending on structure and composition of the precursor. Most striking is the dependency on the cation linked to the starting molybdate material; the ammonium-derived samples show the highest activity.

As described above ammonia is the only counter ion which decomposes during heating. One reason for the comparatively low activity of the materials still containing counter ions could be the different phase changes as a function of temperature as shown in the TG-DSC experiment. Another reason might be a change in the defect structure of the material. During the ammonia combustion NO$_x$ is detected. This can lead to a partial auto reduction of the material and hence a different defect structure which is catalytically inactive. This is corroborated by Mc Carron Ill´s findings which show that

the position of ammonia in the channels of the hexagonal MoO_3 is shifted compared to Na^+ and K^+. Consequently the different interactions leading to different channel sizes and different defect structures[82]. The different band gap energies determined for materials produced from different counter ions also show that different defects prevail.

However, there is a general feature non-depending on the chemical composition stressing out the principal role of structural properties for heterogeneous catalysis. The samples classified supramolecular give rise to a first oxidation maximum centred at 230 °C arising from a very active and non selective oxygen species released from these samples while their structure is rearranged. The role of transient and metastable states in catalysis is further spotted by the observation, that all samples perform quite the same during the second heating.

It is further noteworthy that the acrolein trace of the supramolecular material (223) and the hexagonal MoO_3 (232) run almost parallel at temperatures higher than 400 °C. Consequently the reaction mechanism after a different activation behaviour is very similar. This is in line with the TG-DSC experiment the two traces are clearly different between 250 °C and 370 °C. Moreover the catalytic process is strongly dependent on the final phase transition because the catalytic activity is rising decisively in this region.

Compared to the above described material the hexagonal MoO_3 prepared at 50 °C shows a much higher onset temperature. As shown above the pH curve is very different as well. This proves that the details of the preparation process do matter. Differently protonated precursors will lead to a different nanostructure in the material and this results in a different catalytic behaviour.

The careful investigation of the precursors revealed that the integrative methods such as XRD, vibrational spectroscopy and thermal methods do not detect the smaller unidentified particles determined by TEM. The comparison of the large scale preparation to the smaller scale clearly showed different catalytic behaviour. The TEM investigation showed that the small scale preparation produced a larger extent of small particles. TPRS showed that this material deactivates more slowly and shows higher activity in the second cycle. Therefore these small particles could be the reason for catalytic activity. This could only be revealed in this comprehensive investigation taking the effect of up scaling into account.

Another reason – also detected by TEM – could be that catalytic activity is connected to a nano structuring of the material. Consequently a structural rearrangement or even

worse crystallisation in the thermodynamically most stable form or sintering needs to be avoided. This would be in line with earlier investigations showing that highly crystalline material usually possesses low activity[8].

It is important to note that in this investigation the catalytic activity of a system consisting only of molybdenum and oxygen can be altered over a wide scale only by controlling the defect - and nano - structure of the material. Haber[101] postulates that the introduction of Bi^{3+} in MoO_3 as a promoter generates a new active site responsible for hydrogen abstraction from hydrocarbons. Taking the results of this investigation into account such a change could also be achieved in a system without additives. The same holds true for Grasselli´s investigation[17-19].

Considering Haber´s data and the herein presented results it seems highly likely that catalyst optimization could be possible in a chemical simple system by careful control of the structure development during preparation and by controlling thermodynamic parameters such as reaction temperature and partial pressure of reactants and oxidizing reagents during activation and catalysis.

2.5 CONCLUSION

A number of nanostructured molybdenum oxides with high structural complexity has been successfully prepared. Characterization of the compounds has shown that material with the same structural features as the industrial material (e.g. pentagonal bipyramides or hexagonal channels) can be prepared without the need for any additive or promoter. All of the obtained material is active in selective oxidation of propene, same supramolecular samples even show comparable activities to the industrial material. No material is active as precipitated, but calcination transforms them into metastable active phase at about 300 °C, as seen from the TPRS experiments. Above 450 °C phase transformation into orthorhombic MoO_3 significantly reduces the catalytic activity. Whilst it is often reported that additives increase the catalytic activity, it is more likely that they merely stabilise the metastable Mo-O phase.

Many attempts have been carried out in the literature in order to develop structure activity correlations. This work has demonstrated that such correlations by integrative methods as XRD or Raman have to be treated with extreme caution, as the existence of many differently shaped and structured particles could only be observed with HRTEM.

The TPRS experiments show clearly that even a chemically simple system can be tuned by controlling its thermodynamic parameters. This opens two new pathways. First, catalytic reactions can be studied and understood on comparatively simple model catalysts. Second, catalysts can be optimised by varying and controlling thermodynamic parameters and not only by additives whose role often is obscure.

2.6 TABLES

Table 2.1: Precipitation conditions, (* S= supramolecular, H= hexagonal, T= trimolybdate, O= orthorhombic)

Sample Number	Conditions				
	Family*	counter-ion	Mo-concentration [mol/l]	HNO_3-concentration [mol/l]	Temperature / °C
0249	S	K^+	0.28	2	30
0219	H		0.28	2	50
0229	H		0.28	2	70
0250	S		2	2	30
0245	S		2	2	50
0244	T		2	2	70
0253	S		2	5	30
0246	S		2	5	50
0243	T		2	5	70
0286	S		0.28	5	30
0247	H		0.28	5	50
0233	H		0.28	5	70
0251	O	Li^+	0.28	2	30
0222	O		0.28	2	50
0230	O		0.28	2	70
0252	H	Na^+	2	2	30
0226	H		2	2	50
0231	H		2	2	70
0255	H		2	5	30
0256	S	NH_4^+	0.7	1	30
0227	H		0.7	1	50
0232	H		0.7	1	70

0257	S		1	1	30
0228	S		1	1	50
0258	S		1	5	30
0248	H		1	5	50
0225	S		0,7	2	50
0223	S		1	2	50

Table 2.2: Scale up

Sample Number	Conditions				
	Family*	counter-ion	Mo-concentration [mol/l]	HNO_3-concentration [mol/l]	Temperature / °C
0072	S	NH_4^+	1	1	35
0073	S	NH_4^+	1	1	35
0074	S	NH_4^+	0.5	1	35
0075	S	NH_4^+	0.5	1	35
0130	H	NH_4^+	0.2	1	35/80
0131	H	NH_4^+	0.2	1	35/80
0132	H	NH_4^+	0.1	1	35/80
0133	H	NH_4^+	0.1	1	35/80
0134	S	NH_4^+	2	1	35
0135	S	NH_4^+	2	1	35
0136	S	NH_4^+	1	1	35
0137	S	NH_4^+	2	1	35
0138	S	NH_4^+	2	1	35
0140	S	NH_4^+	1	1	35

Table 2.3: BET surface areas

Sample Nr.	cation	phase identification from Raman	Surface Area (m^2/g)
0219	K^+	Hexagonal MoO_3	1
0229	K^+	Hexagonal MoO_3	0.8
0250	K^+	Supermolecular compound	0.8
0245	K^+	Supermolecular compound	1.2
0244	K^+	Trimolybdate	3.7

0253	K$^+$	Supermolecular compound	0.7
0246	K$^+$	Supermolecular compound	1.5
0243	K$^+$	Trimolybdate	3.5
0254 (286)	K$^+$	Supermolecular compound	0.8
0247	K$^+$	Hexagonal MoO_3	1.1
0233	K$^+$	Hexagonal MoO_3	0.8
0230	Li$^+$	orthorhombic MoO_3	16.2
0226	Na$^+$	Hexagonal MoO_3	3.6
0255	Na$^+$	Hexagonal MoO_3	1.1
0231	Na$^+$	Hexagonal MoO_3	0.5
0228	NH$_4$$^+$	Supramolecular Compound	1.7
0131	NH$_4$$^+$	Hexagonal MoO_3	1.0
0137	NH$_4$$^+$	Supramolecular Compound	1.6
0139	NH$_4$$^+$	Supramolecular Compound	1.5
0140	NH$_4$$^+$	Supramolecular Compound	1.4
0142	NH$_4$$^+$	Supramolecular Compound	0.6

Table 2.4: UV/Vis data

molybdenum oxides			
counter ion	structure	band position/nm	Eg/eV
Li$^+$	orthorhombic	295 (a)	3.48 (a)
		304 (b)	3.37 (b)
		289 (c)	3.48 (c)
K$^+$	trimolybdate	284 (d)	3.77 (d)
		332 (e)	3.27 (e)
Na$^+$	hexagonal	328 (f)	3.27 (f)
		320 (g)	3.27 (g)
K$^+$	hexagonal	319 (h)	3.30 (h)
		305 (i)	3.30 (i)
		316 (k)	3.35 (k)

NH_4^+	hexagonal	316 (k)	3.35 (k)
K^+ NH_4^+	supramolecular hexagonal	310 (m)	3.30 (m)
K^+		284[sh] (n) 329[b] (n)	3.43 (n)
		308 (o)	3.43 (o)
NH_4^+	supramolecular	316 (p)	3.46 (p)
NH_4^+	supramolecular	277[sh] (r) 308[b] (r)	3.55 (r)

Table 2.5: NIR data

molybdenum oxides counter ion	structure								
Li^+	orthorombic	970[vw]	1430		1790	1930			2280
K^+	trimolybdate		1435		1790/ 1810	1930	2000	2095	2250
Na^+	hexagonal		1430		1820	1955			2280
K^+	hexagonal		1435		1820	1935		2090	2235
NH_4^+	hexagonal		1440	1570	1810	1945	2040	2150	
K^+	supramolecular		1435		1810	1935		2090	2235
K^+	supramolecular		1435		1790/ 1810	1930	2000	2095	2250
NH_4^+	supramolecular		1440	1570		1945	2040	2150	
NH_4^+	supramolecular		1440	1570		1945	2040	2150	

Table 2.6: Major Raman band positions and intensities

Sample Nr	Family		Raman bands wavenumber cm⁻¹						
249	S	Pos.	963	882	373	229			
		Int.	7674	5573	2247	3529			
219	H	Pos.	978	904	692	496	401	255	224
		Int.	3478	4875	2112	961	1333	4464	767
229	H	Pos.	978	904	692	493	401	254	224
		Int.	3355	4619	1913	719	1103	4237	881
250	S	Pos.	961	898	372	240			
		Int.	2871	2550	960	1519			
245	S	Pos.	961	894	371	237			
		Int.	3945	3867	1301	1950			

244	T	Pos.	1052	949	938	911	612	372	217
		Int.	808	3579	2673	1311	843	1519	2473
253	S	Pos.	960	899	372	238			
		Int.	2460	1587	594	970			
246	S	Pos.	961	897	372	238			
		Int.	4073	3385	1243	1829			
243	T	Pos.	1052	949	930	911	603	378	219
		Int.	2498	10972	3181	2397	1448	2113	3541
254	S	Pos.	962	898	371	241			
		Int.	3271	2748	1462	1805			
247	H	Pos.	980	904	693	401	254	224	
		Int.	4326	5929	2814	1429	6062	3085	
233	H	Pos.	977	904	692	494	400	254	224
		Int.	3923	5324	2304	982	1388	4830	2514
251	O	Pos.	997	825	668	381	339	292	247
		Int.	8702	20442	3375	2189	3279	8264	3773
222	O	Pos.	997	824	668	382	340	291	247
		Int.	9647	23411	3651	2489	3630	9262	4065
230	O	Pos.	997	825	668	382	339	291	249
		Int.	3651	9694	1545	998	1587	3759	1835
252	O	Pos.	977	902	692	492	398	256	227
		Int.	3772	6110	2365	902	1322	4667	3022
226	H	Pos.	979	902	692	493	398	256	228
		Int.	5033	7759	3205	1726	2150	5753	3970
231	H	Pos.	977	902	692	495	399	255	226
		Int.	1543	2382	914	370	534	1832	1178
255	H	Pos.	976	901	692	493	398	255	229
		Int.	3353	5739	2027	823	1220	4118	2838
256	S	Pos.	959	893	374	233			
		Int.	6085	3866	1535	2473			
227	H	Pos.	976	904	691	494	400	256	224
		Int.	4803	6823	2744	997	1593	6029	1597
232	H	Pos.	976	904	692	494	400	254	224
		Int.	5776	7834	3208	1270	1889	6716	1186
257	S	Pos.	960	884	372	230			
		Int.	931	661	265	417			
228	S	Pos.	959	893	375	237			
		Int.	3304	2196	845	1301			
258	S	Pos.	957	895	374	237			
		Int.	2030	1467	530	865			
248	H	Pos.	976	904	692	494	400	224	

		Int.	2126	2974	1285	456	703	1760
225	S	Pos.	960	893	373	237		
		Int.	4802	3098	1175	1865		

Table 2.7: XRD data

Cation	Sample Name	Phase	Peak Position	Intensity
K	249	Supramolecular	6.88	3498
			10.25	1639
			11.57	1684
			16.06	768
			22.16	765
			25.16	775
			27.11	940
	219	Hexagonal	9.67	10279
			16.77	1549
			19.4	4439
			25.78	15626
			29.31	8269
			35.38	4794
			43.08	1501
			45.39	2385
			48.84	3014
			56	3055
			57.87	1447
			61.67	873
			68.87	1465
	229	Hexagonal	9.66	12215
			16.77	1950
			19.4	4908
			25.79	16943
			29.32	9341
			30.95	1011
			35.39	5188
			43.07	1797
			45.4	2532
			48.84	4128
			56.03	3195
			57.87	1759

			67.13	989
250	Supramolecular		3.87	907
			7.24	1379
			8.59	2237
			11.24	2956
			13.03	1068
			14.2	870
			17.64	596
			19.51	613
			23.18	694
			25.16	596
			27.3	789
			29.43	661
			34.54	391
			37.47	346
			46.88	316
			56.02	261
245	Supramolecular		5.56	1313
			8.63	1926
			11.04	1248
			13.66	1004
			16.93	930
			20.57	766
			22.57	911
			25.01	930
			27.29	1037
			28.72	758
			32.53	519
			37.1	364
			42.84	299
			44.81	376
			47.94	313
			49.32	431
			54.71	306
			57.12	266
			59.31	272
			63.28	255
			65.46	239

244	Trimolybdate	9.77	6569
		11.77	1717
		15.17	1227
		16.56	903
		18.72	1077
		23.84	1580
		25.28	1450
		27.61	2117
		29.56	1553
		31.39	1406
		33.86	715
		39.78	867
		41.16	847
		44.12	470
		47.7	953
		48.8	683
		57	515
253	Supramolecular	5.94	1613
		8.44	2646
		11.19	2197
		13.29	878
		18.08	685
		19.92	661
		23.18	738
		23.55	877
		26.21	837
		29.45	746
		30.75	654
		34.07	483
		36.82	351
		41.87	283
		46.74	342
		49.71	355
		57.72	262
246	Supramolecular	5.54	1134
		6.89	1481
		8.61	1545
		12.23	1105
		12.86	873

			16.96	897
			20.48	702
			22.61	746
			26.75	799
			27.3	990
			28.78	684
			33.28	471
			33.81	406
			38.33	341
			38.82	319
			41.17	296
			44.83	332
			48.14	301
			49.26	329
			51.59	302
			54.65	259
			60.34	228
			61.19	208
			64.34	209
			66.43	190
			69.72	172
243		Trimolybdate	9.77	13269
			15.17	2213
			18.71	1934
			20.77	1115
			23.83	2170
			25.25	2469
			27.58	4512
			29.54	2811
			31.37	3081
			35.13	888
			39.74	1851
			47.51	1894
			48.61	1335
			56.94	1074
			63.61	759
254		Supramolecular	6.51	1677
			8.6	2507
			11.23	5825

			13.24	1294
			17.65	855
			19.51	864
			23.19	1037
			28.19	930
			29.49	834
			34.54	520
			37.48	432
			45.65	397
	247	Hexagonal	9.65	7016
			16.77	1292
			19.38	2755
			25.81	9273
			29.31	6272
			35.38	2933
			43.02	925
			45.32	1217
			48.88	3236
			56.01	2149
			58.77	628
			68.84	782
			79.22	545
			82.5	531
	233	Hexagonal	9.67	13527
			16.78	2122
			19.4	5611
			25.78	19242
			29.32	10308
			30.94	1153
			35.39	6077
			43.06	2132
			45.39	3059
			48.85	3853
			56.01	3646
			57.87	2085
			61.64	1113
			67.11	1183
Li	251	Orthorombic	12.73	712

			16.92	408
			19.31	399
			23.29	1519
			27.32	2310
			33.65	847
			39.11	443
			45.67	397
			49.25	874
			52.37	284
			55.11	452
			57.78	245
			64.71	263
			69.32	191
			78.83	200
	222	Orthorombic	12.79	808
			23.31	1679
			27.34	2285
			33.63	905
			39.14	421
			45.55	416
			49.2	886
			52.33	318
			55.11	466
	230	Orthorhombic	12.79	905
			23.26	1647
			27.34	2379
			33.58	884
			39.08	478
			45.52	427
			49.18	954
			52.19	305
			55.08	505
			64.63	297
Na	252	Hexagonal	9.61	9803
			16.69	1500
			19.29	3476
			25.61	8615
			29.31	6632

			35.31	3330
			42.83	1230
			45.13	1685
			48.96	2171
			56.04	1783
			57.6	1217
			68.72	787
226		Hexagonal	3.37	1686
			9.61	12939
			16.67	1954
			19.27	5226
			25.58	11394
			29.27	9605
			30.87	1003
			33.69	1397
			35.27	4824
			42.77	1591
			45.09	2754
			48.89	3587
			53.03	795
			55.96	3011
			57.54	1791
			66.95	844
			68.69	1562
231		Hexagonal	9.61	8617
			16.68	1319
			19.27	3172
			25.59	7620
			29.28	5842
			35.28	2989
			42.78	1157
			45.11	1717
			48.91	2125
			53.03	582
			55.99	2060
			57.56	1462
			61.21	544
			68.7	998
			86.55	528

	255	Hexagonal	9.61	7672
			16.7	1155
			19.28	3086
			25.59	6950
			29.28	5160
			35.28	2740
			42.79	942
			45.09	1371
			48.91	1808
			53.02	473
			55.98	1426
			57.57	920
			68.69	623
NH_4^+	256	Supramolecular	4.54	1727
			7.02	15128
			11.54	3377
	227	Hexagonal	9.66	9954
			16.78	1692
			19.39	3057
			25.78	11123
			29.31	6866
			35.38	3597
			43.05	1222
			45.37	1725
			48.85	2758
			56	2401
			57.86	1195
			61.67	627
			68.81	1122
	232	Hexagonal	25.78	12037
			29.32	7525
			35.38	4002
			43.03	1500
			45.34	1909
			48.87	2772
			56.03	2518
			57.87	1306

			61.59	730
			68.89	1109
257		Supramolecular	4.35	1678
			6.94	13840
			11.27	2690
			26.38	1154
228		Supramolecular	9.66	9954
			16.78	1692
			19.39	3057
			25.78	11123
			29.31	6866
			35.38	3597
			43.05	1222
			45.37	1725
			48.85	2758
			56	2401
			57.86	1195
			61.67	627
			68.81	1122
258		Supramolecular	6.94	4962
			9.33	1057
			11.54	1785
			26.44	743
248		Hexagonal	9.66	9367
			16.76	1713
			19.38	2712
			25.8	9555
			29.31	6768
			35.37	3708
			43.01	1364
			45.33	1783
			48.87	3856
			53.03	607
			56.02	2396
			57.87	912
			61.54	635
			68.87	990

			82.5	545
225	Supramolecular		4.35	2174
			6.94	13852
			10.81	3894
			26.09	1062

Reference List

[1.]   Kurtz, A. N., Cunningdam, R. W., and Naumann, A. W. Union Carbide Co. [US 4111983]. 1978.
       Ref Type: Patent

[2.]   Novak,   V.,   Sokol,   L.,   and   Jelinek,   J.   CS1207807B.   1981.
       Ref Type: Patent

[3.]   Bertolini, N. and Ferlazzo, S. Euteco Impianti S.p.A. [US 4289654]. 1981.
       Ref Type: Patent

[4.]   Kawajiri, T., Uchida, S., and Hironaka, H. Nippon Shokubai Kagaku. [EP 427 508 A1]. 1991.
       Ref Type: Patent

[5.]   Tenten, A., Martin, F.-G., Hibst, H., Marosi, L., and Kohl, V. BASF AG. [EP 668104 B1]. 1995.
       Ref Type: Patent

[6.]   Hibst,   H.   and   Unverricht,   S.   BASF   AG.   [DE   19815281   A   1].   1981.
       Ref Type: Patent

[7.]   G. Mestl, Ch. Linsmeier, R. Gottschall, M. Dieterle, J. Find, D. Herein, J. Jäger, Y. Uchida, R. Schlögl, *Journal of Molecular Catalysis* **2000,** *162* 455-484.

[8.]   O. Ovsitser, Y. Uchida, G. Mestl, G. Weinberg, A. Blume, J. Jager, M. Dieterle, H. Hibst, R. Schlögl, *J.Mol.Catal.A: Chemical* **2002,** *185* 291-303.

[9.]   M. Dieterle, G. Mestl, J. Jäger, Y. Uchida, R. Schlögl, *J.Mol.Catal.A: Chemical* **2001,** *74* 169.

[10.] Hatano,   M.   and   Kayou,   K.   [EP   318295].   1988.
       Ref Type: Patent

[11.] T. Ushikubo, K. Oshima, A. Kayou, M. Hatano, *Study of Surface Science and Catalylis*, (Eds.: C. Li, Q. Xin) Elsevier, Amsterdam **1997,** p. 473.

[12.] H. Watanabe, Y. Koyasu, *Applied Catalysis A-General* **2000,** *194* 479-485.

[13.] M. M. Lin, *Applied Catalysis A-General* **2003,** *250* 305-318.

[14.] M. M. Lin, *Applied Catalysis A-General* **2003,** *250* 305-318.

[15.] M. M. Lin, *Applied Catalysis A-General* **2003,** *250* 287-303.

[16.] M. Lundberg, M. Sundberg, *Ultramicroscopy* **2003,** *52* 429-435.

[17.] R. K. Grasselli, *Catal.Today* **1999,** *49* 141-153.

[18.] R. K. Grasselli, *Topics in Catalysis* **2001,** *15* 93.

[19.] R. K. Grasselli, *Topics in Catalysis* **2002,** *21* 79.

[20.] S. Knobl, G. A. Zenkovets, G. N. Kryukova, O. Ovitser, M. Dieterle, R. Schlögl, G. Mestl, *J.Catal.* **2003,** *215* 177-187.

[21.] L. Kihlborg, *Arkiv För Kemi Mineralogi och Geologi* **1963,** *21* 427-437.

[22.] L. E. Briand, W. E. Farneth, I. E. Wachs, *Catalysis Today* **2000,** *62* 219-229.

[23.] K. Chen, S. Xie, E. Iglesia, A. T. Bell, *Journal of Catalysis* **2000,** *189* 421-430.

[24.] K. Chen, S. Xie, A. T. Bell, E. Iglesia, *Journal of Catalysis* **2000,** 244-252.

[25.] K. Chen, A. T. Bell, E. Inlesia, *J.Phys.Chem.B* **2000,** *104* 1292-1299.

[26.] K. Chen, S. Xie, E. Iglesia, A. T. Bell, *Journal of Catalysis* **2000,** *189* 421-430.

[27.] K. Chen, S. Xie, A. T. Bell, E. Iglesia, *Journal of Catalysis* **2001,** *198* 232-242.

[28.] J. Haber, V. Turek, *Journal of Catalysis* **2000,** *190* 320-326.

[29.] K.-H. Tytko, B. Schönfeld, B. Buss, O. Glemser, *Angewandte Chemie* **1973,** *85* 305-307.

[30.] B. Krebs, I. Paulat-Böschen, *Acta Cryst.* **1976,** *B32* **1697**.

[31.] B. Krebs, I. Paulat-Böschen, *Acta Cryst.* **1982,** *B 38* 1710.

[32.] I. Paulat-Böschen, *J.C.S.Chem.Comm.* **1979,** 780.

[33.] H. Peters, L. Till, K. H. Radeke, *Zeitschrift fur Anorganische und Allgemeine Chemie* **1969,** *365* 14-21.

[34.] L. Cronin, P. Kögerler, A. Müller, *Journal of Solid State Chemistry - JSSCB* **2000,** *152* 57.

[35.] T. Yamase, P. V. Prokop, *Angew.Chem.Int.Ed.* **2002,** *114* 484.

[36.] J. J. Cruywagen, J. B. B. Heyns, *Inorganic Chemistry* **1987,** *26* 2569.

[37.] J. J. Cruywagen, *Advances in Inorganic Chemistry* **2000,** *49* 127.

[38.] J. J. Cruywagen, A. G. Draaijer, J. B. B. Heyns, E. A. Rohwer, *Inorganica Chimica Acta* **2002,** *331* 322.

[39.] I. Böschen, B. Buss, B. Krebs, O. Glemser, *Angew.Chem.* **1973,** *85* 409.

[40.] O. Glemser, W. Holznagel, A. Iftikhar, *Z.Naturforsch.* **1965,** *20b* 192.

[41.] O. Glemser, G. Wagner, B. Krebs, *Angew.Chem.* **1970,** *82* 639.

[42.] K.-H. Tytko, B. Schönfeld, B. Buss, O. Glemser, *Angew.Chem.Int.Ed.* **1973,** *12* 330.

[43.] K.-H. Tytko, B. Schönfeld, *Zeitschrift fur Naturforschung* **1975,** *30b* 471-484.

[44.] K.-H. Tytko, O. Glemser, *Adv.Inorg.Chem.Radiochem* **1976,** *19* 239.

[45.] K.-H. Tytko, G. Baethe, E. R. Hirschfeld, K. Mehmke, D. Stellhorn, *Z.Anorg.Allg.Chem.* **1983,** *503* 43-66.

[46.] K.-H. Tytko, G. Baethe, *Z.Anorg.Allg.Chem.* **1987,** *555* 85-97.

[47.] I. Lindquist, *Arkiv För Kemi Mineralogi och Geologi* **1950,** *2* 349.

[48.] I. Lindquist, *Arkiv För Kemi Mineralogi och Geologi* **1950,** *18* 325-341.

[49.] I. Lindquist, *Arkiv För Kemi Mineralogi och Geologi* **1950,** *2* 349.

[50.] I. Lindquist, *Acta Cryst.* **1950,** *3* 159.

[51.] M. T. Pope, *Progress in Inorganic Chemistry* **1991,** *39* 181.

[52.] M. T. Pope, A. Müller, *Angewandte Chemie* **1991,** *103* 56-70.

[53.] J. Aveston, E. W. Anacker, J. S. Johnson, *Inorganic Chemistry* **1964,** *3* 735-746.

[54.] H. D. Lutz, R. Nagel, S. A. Mason, A. Müller, H. Bögge, E. Krickemeyer, *J.Solid State Chemistry* **2002,** *165* 199.

[55.] A. Müller, E. Krickemeyer, M. Penk, V. Wittneben, J. Döring, *Angewandte Chemie* **1990,** *102* 85-87.

[56.] A. Müller, W. Plass, E. Krickemeyer, S. Dillinger, H. Bögge, A. Armatage, A. Proust, C. Beugholt, U. Bergmann, *Angewandte Chemie* **1994,** *106* 897-899.

[57.] A. Müller, F. Peters, M. T. Pope, D. Gatteschi, *Chem.Rev.* **1998,** *98* 239-271.

[58.] A. Müller, S. Sarkar, S. Q. N. Shah, H. Bögge, M. Schmidtmann, Sh. Sarkar, P. Kögerler, B. Hauptfleisch, A. X. Trautwein, V. Schünemann, *Angewandte Chemie* **1999,** *111* 3435-3443.

[59.] A. Müller, E. Krickemeyer, S. K. Das, P. Kögerler, S. Sarkar, H. Bögge, M. Schmidtmann, S. Sarkar, *Angew.Chem.* **2000,** *112* 1674-1676.

[60.] A. Müller, S. Q. N. Shah, H. Bögge, M. Schmidtmann, P. Kögerler, B. Hauptfleisch, S. Leiding, K. Wittler, *Angew.Chem.* **2000,** *112* 1677-1679.

[61.] A. Müller, S. K. Das, P. Kögerler, H. Bögge, M. Schmidtmann, A. X. Trautwein, V. Schünemann, E. Krickemeyer, W. Preetz, *Angewandte Chemie* **2000,** *112* 3556-3559.

[62.] D. Volkmer, A. Du Chesne, D. G. Kurth, H. Schnablegger, P. Lehmann, M. J. Koop, A. Müller, *J.Am.Chem.Soc.* **2000,** *122* 1995-1998.

[63.] V. W. Day, W. G. Klemperer, W. Shum, *J.Am.Chem.Soc.* **1977,** *99* 952.

[64.] V. W. Day, M. F. Fredrich, W. G. Klemperer, W. Shum, *J.Am.Chem.Soc.* **1977,** *99* **6146**.

[65.] W. G. Klemperer, *Angew.Chem.* **1978,** *17* 246.

[66.] W. G. Klemperer, W. Shum, *J.Am.Chem.Soc.* **1976,** *98* 8291.

[67.] O. W. Howarth, P. Kelly, L. Pettersson, *J.Chem.Dalton Trans.* **1990,** 81.

[68.] G. Johanson, L. Pettersson, N. Ingri, *Acta Chemica Scandinavica* **1979,** *A 33* 305-312.

[69.] G. Johanson, L. Teterson, N. Ingri, *Acta Chemica Scandinavica* **1979,** *A 33* 305-312.

[70.] M. Dieterle, G. Weinberg, G. Mestl, *Phys.Chem.Chem.Phys.* **2002,** *4* 812.

[71.] G. Mestl, *Ramanspektroskopische Charakterisierung von Oxidkatalysatoren*, Universität München, München **1994,** p. 1.

[72.] T. Ressler, O. Timpe, T. Neisius, J. Find, G. Mestl, M. Dieterle, R. Schlögl, *Journal of Catalysis* **2001,** *191* 75-85.

[73.] J. Melsheimer, M. Thiede, R. Ahamad, *Phys.Chem.Chem.Phys.* **2003,** *5* 4366-4370.

[74.] G. Mestl, T. K. K. Srinivasan, *Cat.Rev.Sci.Eng.* **1998,** *40* 451-570.

[75.] N. Sotani, *Bull.Chem.Soc.Japan* **1975,** *48* 1820-1825.

[76.] L. J. Bellamy, *The Infraredspectra of Complex Molecules*, Mathuen, London **1966,** p. 346.

[77.] B. Herzberg, *Molecular Spectra and Molecular Structure*, D. van Norstrand, New Jersey **1968,** p. 167.

[78.] B. M. Gatehouse, P. Leverett, *J.Chem.Soc.(A)* **1968,** 1398-1405.

[79.] N. A. Caiger, S. Crouch-Baker, P. G. Dickens, *J.Solid State Chemistry* **1987,** *67* 369-373.

[80.] J. D. Guo, P. Zavalij, M. S. Whittingham, *Eur.J.Solid State Inorg.Chem.* **1994,** *31* 833-842.

[81.] E. M. McCarron III, *J.Chem:Soc., Chem.Commun.* **1986,** 336.

[82.] E. M. McCarron III, D. M. Thomas, J. C. Calabrese, *Inorganic Chemistry* **1987,** *26* 370-373.

[83.] B. Krebs, I. Paulat-Böschen, *Acta Cryst.* **1976,** *B32* **1697**.

[84.] Wienold, J., **2003**.

[85.] F. Schüth, *Angew.Chem.Int.Ed.* **2003,** *42* 3604-3622.

[86.] A. Müller, F. Peters, M. T. Pope, D. Gatteschi, *Chem.Rev.* **1998,** *98* 239-271.

[87.] J. L. Garin, J. M. Blanc, *Journal of Solid State Chemistry - JSSCB* **1985,** *58* 98-102.

[88.] V. W. Day, M. F. Fredrich, W. G. Klemperer, W. Shum, *J.Am.Chem.Soc.* **1977,** *99* **6146**.

[89.] K.-H. Tytko, O. Glemser, *Adv.in Chem.Series* **1976,** *19* 239-315.

[90.] L. Kihlborg, *Arkiv För Kemi Mineralogi och Geologi* **1963,** *21* 427-437.

[91.] N. Yamazoe, L. Kihlborg, *Acta Cryst.* **1975,** *B31* 1666.

[92.] B. Chae, Y. M. Jung, X. Wu, S. B. Kim, *J.of Raman Spectroscopy* **2003,** *34* 451.

[93.] M. A. Py, K. A. Maschke, *Physica B* **1981,** *105* 376.

[94.] C. Julien, G. A. Nazri, *Solid State Ionics* **1994,** *68* 111.

[95.] G. A. Nazri, C. Julien, *Solid State Ionics* **1992,** *376* 53-56.

[96.] F. A. Cotton, R. M. Wing, *Inorganic Chemistry* **1965,** *4* 867.

[97.] L. Seguin, M. Figlarz, R. Cavagnat, J. C. Lassegues, *Spectrochimica Acta Part A-Molecular and Biomolecular Spectroscopy* **2222,** *51* 1323-1344, 1995.

[98.] I. R. Beattie, T. R. Gilson, *J.Chem.Soc.* **1969,** *A* 2322.

[99.] M. Fournier, C. Rocchicioli-Deltcheff, L. P. Kazansky, *Chemical Physics Letters* **1994,** *223* 297-300.

[100.] H. Jeziorowski, H. Knözinger, *Journal of Phys.Chem.* **1979,** *83* 1166.

[101.] J. Haber, E. Lalik, *Catalysis Today* **1997,** *33* 119-137.

3 In situ Raman investigation of the decreasing pH preparation method leading to various MoO₃ structures

3.1 INTRODUCTION

Precipitation is one of the major synthesis routines for molybdenum oxide based catalysts, because it is inexpensive and can be carried out industrially on a large scale. The most common precursor is ammonium heptamolybdate tetra hydrate, and the precipitating agent is often nitric acid, because all counter cations are nitrogen based and can be easily removed by subsequent calcination. However, in many cases not enough attention is drawn to the fact that the process of precipitation is crucially affected by a multitude of parameters, such as temperature, precursor and acid concentration or the nature of the counter cation. Reproducible results are only obtained if all these parameters are fully controlled. A large study recently showed that four different families of products can be obtained by just altering the parameters mentioned[1]. During the reaction many isopolymolybdates are formed as intermediates which are essentially pH-dependent and exist in equilibrium[2-14]. At low temperatures a $Mo_{36}O_{112}{}^{8-}$ like compound was obtained with ammonia heptamolybdate as precursor. At 70 °C hexagonal MoO_3 was obtained. At 50 °C depending on the concentration of the starting solution either $Mo_{36}O_{112}{}^{8-}$ or hexagonal MoO_3 could be obtained. The pH curves of the reactions at the different temperatures were different and therefore different formation mechanisms most likely prevail.

In order to achieve a rational catalyst preparation it is vital to know the reaction mechanism in solution. Very early investigations on aqueous molybdenum systems were carried out[15-17] in which determination of diffusion coefficients, UV/Vis and conductometric-, potentiometric-, and thermometric–titrations were used as main methods. Saski and Sillen[18] presented the first comprehensive potentiometric investigation. A milestone was the identification of the hepta and octa molybdate structures by X-ray single crystal analysis[19-21].

Another breakthrough was achieved by Aveston and Anacker[22] and Tytko and Glemser[23-25] by combining Raman spectroscopy and single crystal analysis which enabled them to correlate solid state structures with compounds in solution. As a result a distinction was made between the heptamolybdate that dominates between pH six and four, and the octamolybdate, which dominates, between pH four and two. Contributions to reveal details of the reaction mechanism were delivered by O-NMR spectroscopy[26-29]. Recently Cruywagen[30-32] published more potentiometric data and an computer aided evaluation. Further, a combination of X-Ray Scattering and Raman spectroscopy was applied[33].

Whilst the investigations mentioned above have brought many insights into the solution chemistry of the molybdate system, they have only limited significance for large scale catalyst preparation as almost all of these reactions were carried out at room temperature (whatever temperature this is), in low dilutions and further electrolytes such as $NaClO_4$ or $NaCl$ were added. Catalyst synthesis is commonly done at large scale, with high precursor concentrations, and the presence of chlorine is avoided. In addition there is a lack of in situ analysis that shows exactly the formation of precipitates out of octamolybdates. Therefore the study aims at bridging the gap between structural inorganic chemistry and catalyst preparation.

3.2 EXPERIMENTAL

Preparation

A starting solution was prepared by dissolving ammonium heptamolybdate tetra hydrate (AHM, Merck) in bidestilled water in order to obtain a Mo concentration of 0.7 mol/l. As precipitation agent HNO_3 1 mol/l was applied. Whilst the molybdate solution was stirred with a magnetic stirrer, constant temperature conditions were maintained by using a water bath. Acid was added in 5 ml portions with an automated titrator (Metrohm) and the pH measurement was performed with a pH electrode (Mettler Toledo) carefully calibrated to the respective reaction temperatures. Standards applied: pH = 2, 4, 7 (Merck).

Raman spectroscopy

Raman spectroscopy was performed on a Labram I (Dilor) instrument equipped with a confocal microscope (Olympus). A notch filter (Kaiser Optical) was applied to cut off the laser-line and the Rayleigh scattering up to 150 cm^{-1}. The spectrometer is equipped with a CCD camera (1024*298 diodes), which is Peltier cooled to −30 °C to reduce the thermal noise. A He-laser (Melles Griot) was used to excite the Raman scattering at 632 nm with a laser power of 1,4 mW. The following spectrometer parameters were used: microscope objective: 10; slit width: 400 μm (spectral resolution: 2.5 cm^{-1}), integration time: 30 s per spectrum and 10 averages. To get spectra from the solution the laser beam was redirected on the beaker with an optical angle. The laser beam was used as well to check for any Tyndall effect, which indicates particle formation in the solution.

3.3 RESULTS

The most decisive spectral changes in this investigation were observed between 740 and 1000 cm^{-1}. Whilst the region between 740 and 800cm^{-1} is associated with Mo-O-Mo bridging modes the region between 800 and 1000 cm^{-1} is assigned to terminal Mo-O stretching frequencies[3].

3.3.1 Reaction at 30 °C

The starting pH of the reaction is 5.5 and the respective Raman spectrum (Fig. 3.1) shows bands at 943, 898, 560, 362 and 219 cm^{-1}. At pH 5.0 the band positions are still the same however the intensity of the bands at 943 and 898 cm^{-1} has decreased considerably.

At pH 4.5 the former band at 898 cm^{-1} has turned into a shoulder and its position is slightly shifted to higher wavenumbers. The band at 943 cm^{-1} has now shifted to 948 cm^{-1}. At pH 4.0 the band has a lower maximum height but it is broader. Its centre is now situated at 950 cm^{-1}. This tendency is continued at pH 3.5. However it is noteworthy that a shoulder develops at 970 cm^{-1} pointing to the existence of β octamolybdate[34].

At pH 3.0 a band is detected at 959 cm^{-1}, commonly assigned to α octamolybdate[34]. This band shows a weak shoulder at 953 cm^{-1} and a more pronounced one at 921 cm^{-1}. Another band appears at 970 cm^{-1}. At pH 2.5 the band at 959 and 970 cm^{-1} still prevails the other spectral features underwent an up shift of 2 cm^{-1}. These two bands

however are not very clearly separated. Therefore it could be interpreted as a single band at 964 cm^{-1} which is split. This situation prevails until pH 1.5 is reached at this pH the Tyndall effect starts to appear, which indicates formation of solid particles in the solution.
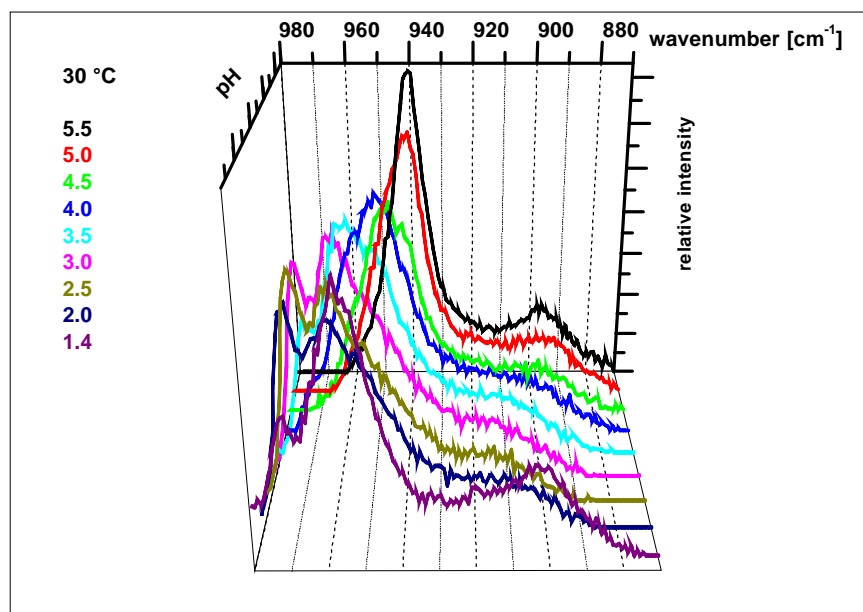
Figure 3.1: In situ Raman investigation at 30 °C

At pH 1.4 bands are detected at 983 (sh), 970, 955 902 and 854 cm^{-1}; the reaction mixture is slightly cloudy. At pH 1.3 precipitation occurred coinciding with a total decline in resolution. A similar effect was observed by Mestl[35]. Looking at the bands at lower wavenumbers the band at 362 cm^{-1} underwent an up shift and decreased in intensity. The band at 219 cm^{-1} decreased as well in intensity but shifted to lower wavenumbers.

3.3.2 Reaction at 50 °C

The reaction at 50 °C starts with pH 5.17 and bands are detected (Fig. 3.2) at 943, 898, 560, 455, 362, 219 cm^{-1}. Apart from the band at 455 cm^{-1} this matches with the experiment carried out at 30 °C. At pH 4.5 the main band has shifted to 945 cm^{-1} its height is decreased and it has broadened and at 897 cm^{-1} only a shoulder is detected.
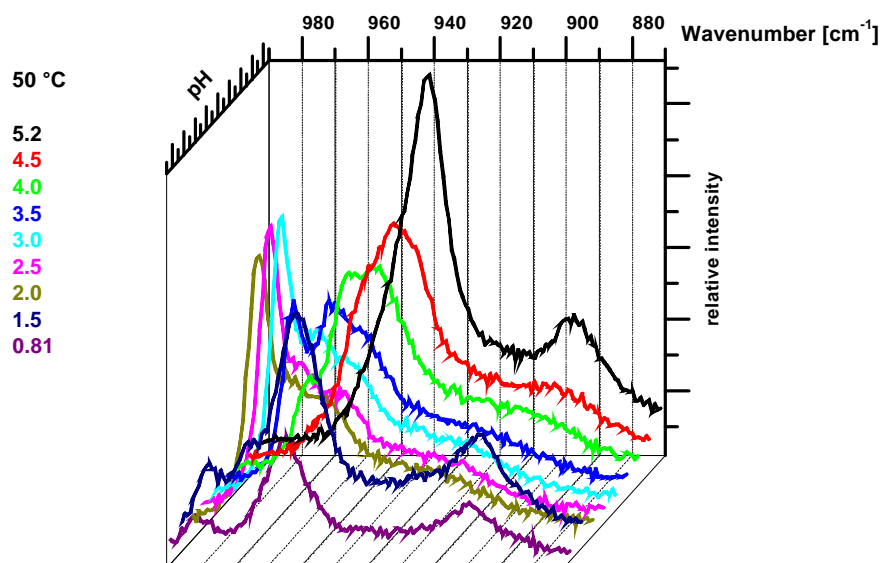
Figure 3.2: In situ Raman investigation at 50 °C

At pH 4.04 a shoulder appears at 970 cm^{-1} the main band starts to split and shows two signals at 956 and at 949 cm^{-1}, the shoulder at 896 cm^{-1} has lost intensity again. At pH 3.51 a marked band has developed at 970 cm^{-1}. Further bands a registered at 961, 954 (sh), 925 (sh) and 853 cm^{-1}. At pH 2.99 the band positions are still the same. The band at 970 cm^{-1} however has gained more intensity. Until pH = 2.06 is reached the situation stays the same. At this pH the first Tyndall effect is observed. The spectrum is changing at pH = 1.51. Bands are found at 981 cm^{-1} (assigned to the presence of $[Mo_{36}O_{112}]^{8-}$), 970 (sh), 955 and 900 cm^{-1}. At pH 1.09 the same spectrum is recorded but the intensities are lower. At pH = 0.81 precipitation sets in.

3.3.2 Reaction at 70 °C

At 70 °C the reaction starts at pH 5.0 bands are (Fig. 3.3) detected at 953 (sh), 943, 898, 560, 362, 254 (sh) and 220 cm^{-1}. At pH 4.5 the situation has changed. Bands are recorded at 955, 947 and at 896 cm^{-1}. At pH 4.0 the intensity is increasing and bands are situated at 969, 961 (sh), 956, 950 (sh) 946, 939 (sh) and 908 cm^{-1}. At pH 3.5 the band at 969 cm^{-1} is gaining intensity the one at 956 does not considerably change and the band at 946 cm^{-1} diminishes.
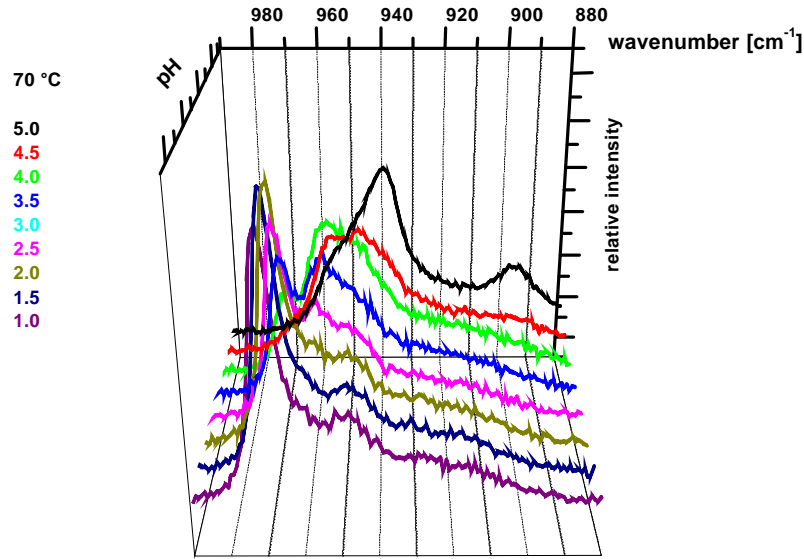
Figure 3.3: In situ Raman investigation at 70 °C

At pH = 3.0 the above described trend prevails. The spectra at pH = 2.5, 2.0 and 1.5 are almost identical. They are characterised by bands at 970, 948, 920 (sh) and 847 cm^{-1}. At pH = 1 precipitation sets in.

3.4 DISCUSSION

Although the solution chemistry of molybdates has been very well studied in the past, this work is the first to present an in situ study of the system at different temperatures. A summary of the findings is displayed in Fig. 3.5.

$$Mo_7O_{24}^{6-} + H^+ \qquad \leftrightarrow \qquad HMo_7O_{24}^{5-} \qquad (1)$$

$$MoO_4^{2-} + Mo_7O_{24}^{6-} + 2H^+ \qquad \leftrightarrow \qquad H_3Mo_8O_{28}^{5-} \qquad (2)$$

$$H_3Mo_8O_{28}^{5-} + H^+ \qquad \leftrightarrow \qquad Mo_8O_{26}^{4-} + H_2O \qquad (3)$$

$$4\,Mo_8O_{26}^{4-} + 4MoO_4^{2-} + 16H^+ \qquad \leftrightarrow \qquad Mo_{36}O_{112}^{8-} + 8\,H_2O \qquad (4)$$

$$5Mo_8O_{26}^{4-} + 4H^+ \qquad \leftrightarrow \qquad 8Mo_5O_{16}^{2-} + 2\,H_2O \qquad (5)$$

$$Mo_8O_{26}^{4-} + MoO_4^{2-} \qquad \leftrightarrow \qquad 3Mo_3O_{10}^{2-} \qquad (6)$$

$$Mo_8O_{26}^{4-} + 4H^+ \qquad \leftrightarrow \qquad 8MoO_3 + 2\,H_2O \qquad (7)$$
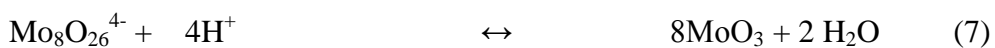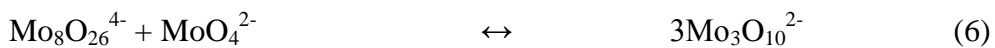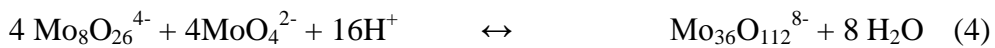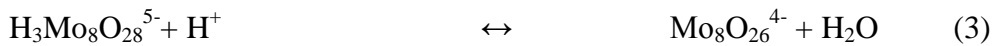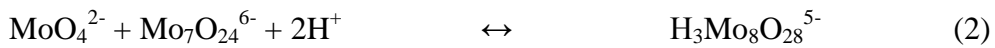
The equations show the net reactions that occur during titration of the molybdate solutions. For a closer evaluation of the pH curves the following assumptions have to be taken into account. The solution consists of many different entities like monomolybdates, which are present over the whole range of pH. The species mentioned above are dominant at relevant pHs, transformation from one species into the other occurs via three steps. The mechanism includes protonation and condensation reactions, further it can be assumed that MoO_6 entities are always detached and reattached.

The first three steps describe the transformation from hepta to octamolybdate. The first step involves protonation of the heptamolybdate ion (1), which causes instabilities of the system. Detachment and reattachment of MoO_4 units lead to (2) as net reaction, a subsequent condensation reaction leads to octamolybdate (3). It has been mentioned earlier, that at least three different octamolybdate isomers are present in solution. Whilst the α octamolybdate is present a pH = 2.7, the β octamolybdate is present at lower pH, and the γ octamolybdate is formed as intermediate step between the α and β form (Fig. 3.4).

As the pH curves are more or less similar up to pH = 2.5 it can be assumed that every reaction path has the octamolybdate as intermediate step. The further reaction path is controlled by the external factors mentioned above like temperature, reactant concentrations or nature of counter cation.

The pathway with the lowest activation barrier might be polycondensation, as this allows distribution of the negative charge across many MoO_6 units. The equation (4) will be shifted to the right if either the amount of molybdate or acid is large, further the presence of a sufficiently large counter cation is required. Higher temperature causes polycondensation of a lower extent, and reaction (5) is pursued, leading to the hex phase.

It is well established that the dominating molybdate species in a solution between pH = 6 and 3.5 is the heptamolybdate ion. The Raman spectra presented in this work clearly support this assignment, as the major band at 943 cm^{-1} was assigned to the terminal terminal Mo-O ν(MoO) frequency of heptamolybdate (C_{2v}) in many publications[22][36]. Only Ueda observed this band at 939 cm^{-1}, but this small shift may just arise from different pH or temperature conditions.
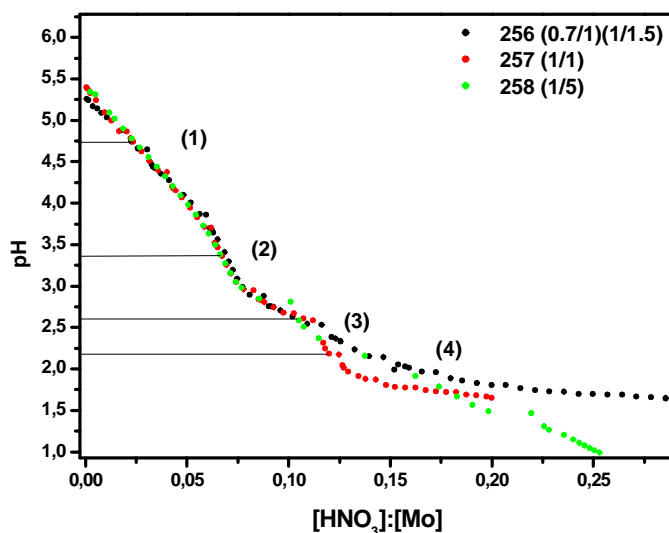
Figure 3.4: pH-trace; interpretation of equivalence points

It has been reported earlier, that increasing amounts of protons lead to protonation and condensation reactions[37]. In the Raman spectrum protonation will cause a decrease in intensity of the terminal Mo-O vibration, and condensation will cause a shift in band position. Indeed both phenomena have been observed. Further, a correlation between the effects observed in the Raman spectra and the pH curve, that was published earlier by the above authors can be made.

Protonation corresponds to a large buffering section in the pH curve and condensation to a drop in pH. The first major condensation product is the octamolybdate, a mechanism for that has been reported in the literature[31;38;39]. Many octamolybdate isomers are reported to exist in equilibrium, whilst the α-octamolybdate is reported to be the dominating species at around pH = 2.7, acidification is reported to shift the equilibrium to the β molybdate[34]. There are many publications about the mechanism of isomerization between the α and the β form[26;40-42] although there is no convincing explanation about the factors that favour isomerisation. Bridgeman assessed the thermodynamic stability of the two isomers by carrying out DFT calculations. He reported that the α octamolybdate is more thermodynamically stable than the β form, because of unfavourable steric interactions of the β form. Therefore it can be concluded that the isomerisation process is kinetically controlled.

A mechanism for the isomerisation process has been postulated by Klemperer et al.[26] with an intermediate γ octamolybdate. Whilst this isomer has been found in the solid state[34] it has been not observed in solution in any large quantities, therefore it can be considered as rather unstable. In any way, transformation of the α into the β

form requires breaking of at least two bonds. It is postulated by a number of authors [43], that is process is enhanced by creation of hydrogen bonds of the type N-H...O-Mo. A decrease in pH would drastically enhance the strength of this bond, therefore the process of transformation into the β form would be enhanced. In addition this transformation via bond breaking is expected to have a considerable activation barrier, hence a raise in temperature should ease the isomerisation process. Both effects are observed in the Raman spectra presented.

The drastic temperature effect on the precipitation products has been reported recently [44]. Whilst at 30 °C a smooth transformation into the supramolecular Mo_{36} species is observed, at 70 °C the β octamolybdate is still the dominant species at pH = 1. The β octamolybdate is assigned as precursor for formation of the hexagonal phase, but as this process requires massive bond breaking and reassembling, as the β form has only edge sharing connections, whilst the hexagonal precipitate has many corner sharing connection. Again, the activation barrier has to be overcome by high temperature. The fact that no precipitation of the supramolecular compound was observed might be explained by the non existence of the α octamolybdate, which is largely present at lower temperatures. The α form might either be a direct precursor or at least a necessary compound for the Mo_{36} formation. If that is to be the case, then the ratio of α to β octamolybdate, which is temperature dependent, determines also the nature of the final precipitate.

A more quantitative interpretation of the Raman spectra is difficult for as there may be many more molybdate species present in solution. The fact that no isosbestic points were found supports this assumption[23]. Even more, neither the hexagonal phase nor the supramolecular phase can be formed just out of octamolybdates, therefore other intermediates need to appear.

Taking all this findings into account the variation of reaction temperature shifts the equilibrium between the $\alpha\text{-}Mo_8O_{26}^{4-}$ and the $\beta\text{-}Mo_8O_{26}^{4-}$ species. The location of this equilibrium seems to determine the product obtained. All this can be very clearly seen by the in situ Raman experimentation.

3.5 CONCLUSION

The in situ Raman data presented in this work has clearly demonstrated the severe temperature effect on the nature of molybdate species in solution. Although the temperature steps chosen in this work are rather large (20 °C), it must be assumed that even a couple of degrees can significantly alter the ratio of species in solution. The numerous preceding work in this field has to be re-evaluated in the light of the results presented. Earlier pH studies, that showed different reaction mechanisms, which occurred at different temperatures are confirmed by the results presented.
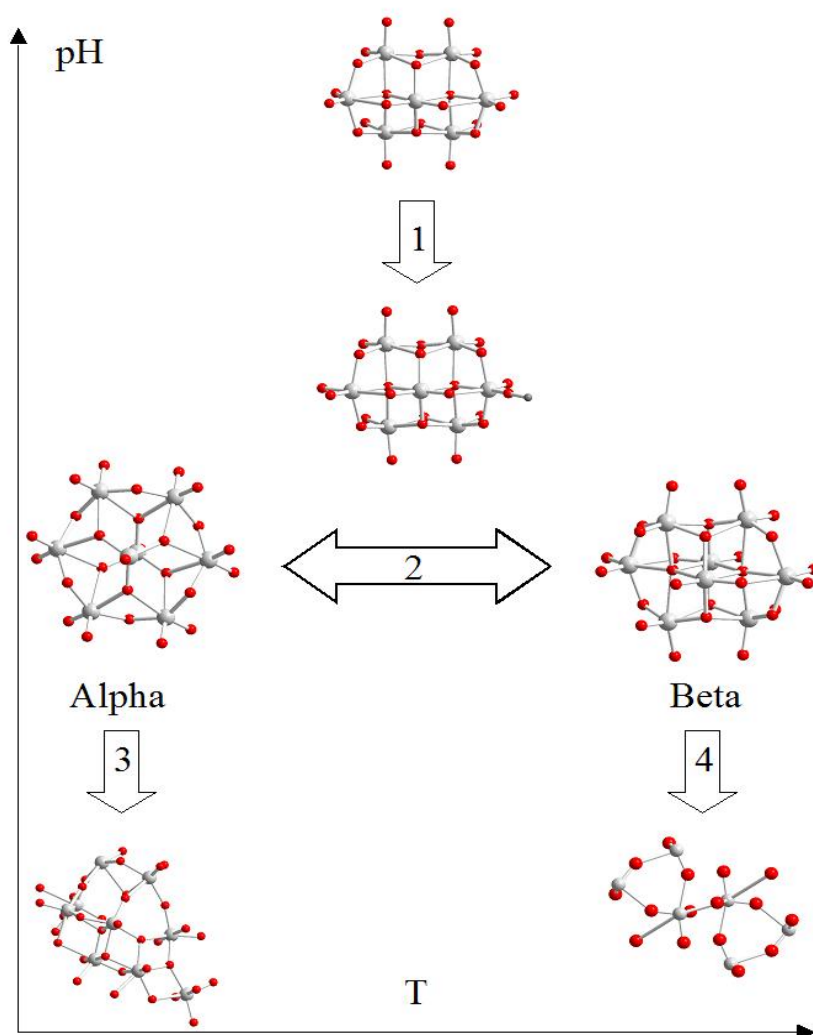
Figure 3.5: Dominant species in solution, dependent on temperature and pH. Step 1: Protonation of the heptamolybdate ion. Step 2: T dependent isomerisation. Step 3: Precipitation of a supramolecular Mo_{36} compound. Step 4: Kinetically controlled Precipitation of hex. MoO_3

Reference List

[1.] S. Knobl, O. Timpe, Niemeyer D., S. B. A. Hamid, R. Schlögl, *J.Catal.* **2004.**

[2.] A. Müller, F. Peters, M. T. Pope, D. Gatteschi, *Chem.Rev.* **1998,** *98* 239-271.

[3.] G. Mestl, T. K. K. Srinivasan, *Cat.Rev.Sci.Eng.* **1998,** *40* 451-570.

[4.] M. T. Pope, *Progress in Inorganic Chemistry* **1991,** *39* 181.

[5.] M. T. Pope, A. Müller, *Angewandte Chemie* **1991,** *103* 56-70.

[6.] L. Cronin, P. Kögerler, A. Müller, *Journal of Solid State Chemistry - JSSCB* **2000,** *152* 57.

[7.] M. I. Khan, A. Müller, S. Dillinger, H. Bögge, Q. Chen, J. Zubieta, *Angewandte Chemie* **1993,** *105* 1811-1814.

[8.] H. D. Lutz, R. Nagel, S. A. Mason, A. Müller, H. Bögge, E. Krickemeyer, *J.Solid State Chemistry* **2002,** *165* 199.

[9.] A. Müller, E. Krickemeyer, M. Penk, V. Wittneben, J. Döring, *Angewandte Chemie* **1990,** *102* 85-87.

[10.] A. Müller, W. Plass, E. Krickemeyer, S. Dillinger, H. Bögge, A. Armatage, A. Proust, C. Beugholt, U. Bergmann, *Angewandte Chemie* **1994,** *106* 897-899.

[11.] A. Müller, S. Q. N. Shah, H. Bögge, M. Schmidtmann, P. Kögerler, B. Hauptfleisch, S. Leiding, K. Wittler, *Angew.Chem.* **2000,** *112* 1677-1679.

[12.] A. Müller, S. K. Das, P. Kögerler, H. Bögge, M. Schmidtmann, A. X. Trautwein, V. Schünemann, E. Krickemeyer, W. Preetz, *Angewandte Chemie* **2000,** *112* 3556-3559.

[13.] A. Müller, S. Sarkar, S. Q. N. Shah, H. Bögge, M. Schmidtmann, Sh. Sarkar, P. Kögerler, B. Hauptfleisch, A. X. Trautwein, V. Schünemann, *Angewandte Chemie* **1999,** *111* 3435-3443.

[14.] A. Müller, R. Rohlfing, J. Döring, M. Penk, *Angewandte Chemie* **1991,** *103* 575-577.

[15.] G. Jander, K. F. Jahr, W. Heukeshoven, *Zeitschrift fur Anorganische und Allgemeine Chemie* **1930,** *194* 383-428.

[16.] A. Rosenheim, *Zeitschrift fur Anorganische und Allgemeine Chemie* **1916,** *96* 139.

[17.] O. Glemser, W. Holznagel, A. Iftikhar, *Z.Naturforsch.* **1965,** *20b* 192.

[18.] Y. Sasaki, L. Sillén, *Arkiv För Kemi Mineralogi och Geologi* **1968,** *29* 253.

[19.] I. Lindquist, *Arkiv För Kemi Mineralogi och Geologi* **1950,** *18* 325-341.

[20.] I. Lindquist, *Arkiv För Kemi Mineralogi och Geologi* **1950,** *2* 349.

[21.] I. Lindquist, *Acta Cryst.* **1950,** *3* 159.

[22.] J. Aveston, E. W. Anacker, J. S. Johnson, *Inorganic Chemistry* **1964,** *3* 735-746.

[23.] K.-H. Tytko, B. Schönfeld, B. Buss, O. Glemser, *Angewandte Chemie* **1973,** *85* 305-307.

[24.] K.-H. Tytko, B. Schönfeld, *Zeitschrift fur Naturforschung* **1975,** *30b* 471-484.

[25.] K.-H. Tykto, G. Petridis, B. Schönfeld, *Z.Naturforsch.* **1980,** *35b* 45-56.

[26.] V. W. Day, W. G. Klemperer, W. Shum, *J.Am.Chem.Soc.* **1977,** *99* 952.

[27.] V. W. Day, M. F. Fredrich, W. G. Klemperer, W. Shum, *J.Am.Chem.Soc.* **1977,** *99* **6146.**

[28.] W. G. Klemperer, *Angew.Chem.* **1978,** *17* 246.

[29.] O. W. Howarth, P. Kelly, L. Pettersson, *J.Chem.Dalton Trans.* **1990,** 81.

[30.] J. J. Cruywagen, J. B. B. Heyns, *Inorganic Chemistry* **1987,** *26* 2569.

[31.] J. J. Cruywagen, *Advances in Inorganic Chemistry* **2000,** *49* 127.

[32.] J. J. Cruywagen, A. G. Draaijer, J. B. B. Heyns, E. A. Rohwer, *Inorganica Chimica Acta* **2002,** *331* 322.

[33.] G. Johanson, L. Pettersson, N. Ingri, *Acta Chemica Scandinavica* **1979,** *A 33* 305-312.

[34.] S. Himeno, H. Niiya, T. Ueda, *Bulletin of the Chemical Society of Japan* **1997,** *70(3)* 631-637.

[35.] G. Mestl, *J.of Raman Spectroscopy* **2002,** *33* 333-347.

[36.] K.-H- Tytko, G. Petridis, B. Schönfeld, *Zeitschrift fur Naturforschung* **1980,** *35b* 45-56.

[37.] S. B. A. Hamid, D. Othman, N. Abdullah, O. Timpe, S. Knobl, Niemeyer D., R. Schlögl, *Topics in Catalysis* **2003,** *24* 87-95.

[38.] K.-H. Tytko, O. Glemser, *Adv.in Chem.Series* **1976,** *19* 239-315.

[39.] K.-H. Tytko, O. Glemser, *Adv.Inorg.Chem.Radiochem* **1976,** *19* 239.

[40.] W. G. Klemperer, W. Shum, *J.Am.Chem.Soc.* **1976,** *98* 8291.

[41.] A. Bridgeman, G. Cavigliasso, *Inorganic Chemistry* **2002,** *41* 3500-3507.

[42.] A. Bridgeman, *J.Phys.Chem.* **2002,** *106* 12151-12160.

[43.] X.-J. Wang, B.-S. Kang, C.-Y. Su, K.-B. Yu, H.-X. Zhang, Z.-N. Chen, *Polyhedron* **1999,** *18* 3371-3375.

[44.] S. Knobl, O. Timpe, N. Abdullah, D. Othman, Niemeyer D., S. B. A. Hamid, R. Schlögl, *Journal of Catalysis* **2004,** *submitted* .

4 Nanoclusters as Precursors to (MoVW)$_5$O$_{14}$: In situ and chemical characterisation of the systems of a single phase oxidation catalyst

4.1 INTRODUCTION

Selective partial oxidation of hydrocarbons is an important synthesis step for about 25% of all organic products that are produced worldwide[1]. Particularly important reactions are the oxidation of propane/propene to acrolein and acrylic acid. The common catalyst material used for these reactions involves vanadium and tungsten doped molybdenum oxides[2-8]. Therefore considerable efforts have been made to resolve the structure of the catalytically active phase, as this would be of enormous economic and scientific benefit. Mestl *et al.*[9-11] observed a Mo$_5$O$_{14}$ type single phase emerging during oxidation of ethanol, acrolein and propene over mixed VWMo oxide and this structure was assigned to the active phase of the catalyst.

The structure of the individual Mo$_5$O$_{14}$ was discovered first by Kihlborg[12]. The main structural motif of Mo$_5$O$_{14}$ is a pentagonal bipyramidal coordination. The same motif has also been observed by Müller[13] and identified as an important building block[14] for formation of large polymolybdates (keplerates, >500 atoms), in which these pentagonal bipyramidal units are linked and placed at the 12 corners of an icosahedron, and also by Böschen *et al.* in K$_4$Mo$_{36}$O$_{112}$ *8 H$_2$O[15;16]. Even in the photochemical molybdenum blues reaction this motif is discussed[17]. It is also known that binary Mo based oxides doped with V, Nb, W or Ta[18;19] possess a structure similar to Mo$_5$O$_{14}$. Knobl *et al.*[20] described the preparation of single phase (MoVW)$_5$O$_{14}$, which was achieved by spray drying of a mixture of ammonium heptamolybdate (AHM), ammonium metatungstate (AMT) and vanadyl oxalate solutions followed by thermal treatment. Raman spectroscopy of the solution of the (MoVW)$_5$O$_{14}$ precursor showed bands that were assigned to terminal M=O and bridging M-O-M vibrations characteristic of polyoxo metallates. No reference was made to the element and oxidation state of these bridges. Structure and composition of the pure Mo, W and V complexes as well as those of the mixed V-Mo, W-Mo species in the solutions have been studied at the wide ranges of pH and component ratio[13;21-26].

However, the nature of the species of ternary VWMo obtained from the mixed solution of AHM, AMT and vanadyl oxalate is still obscure.

The aim of the present study is to analyse the species in the precursor solution of $(MoVW)_5O_{14}$ and to investigate the role of vanadium and tungsten concerning structure development. UV/Vis, ESR and ^{95}Mo NMR spectroscopy have been applied to get more information about complexes developed in the precursor solution and hence about the reaction scheme leading to the formation of the complex oxide phase.

4.2 EXPERIMENTAL

The precursor for the single phase Mo_5O_{14} type catalyst was prepared according to Knobl et al.[20] by mixing aqueous solutions of ammonium heptamolybdate (AHM with Mo concentration of 0.963 mol/l), ammonium metatungstate (AMT with W concentration of 0.271 mol/l), and vanadyl oxalate (V concentration of 0.84 mol/l), so that an atomic ratio between Mo, V and W will be equal to 0.68:0.23:0.09.

After mixing all parent solutions, concentrations of Mo, W and V became equal to 0.52, 0.07 and 0.175 mol/l, respectively. The pH of the mixed precursor solution became equal to 3.5. For comparison some single and binary mixed aqueous solutions have been also prepared with the same element concentrations as in mixed solution. Binary AHM and AMT aqueous solutions with ratio of W/(W+Mo) equal to 9% and with concentration of 0.52 mol/l Mo and 0.07 mol/l W were prepared. The pH of the single and binary solutions was close to 5.1. For some UV/Vis and NMR experiments the pH was lowered to 3.5 by adding oxalic acid. Another set of the model binary solutions between AHM and vanadyl oxalate with different ratios of V/(V+Mo) equal to 4.6, 9.2, 13.8, 18.4, 23% and concentrations of Mo and V in the binary solution equal to 0.52 mol/l and 0.03, 0.07, 0.10, 0.14, 0.17, respectively, was synthesised. The pH of these binary solutions depends strongly on the V content.
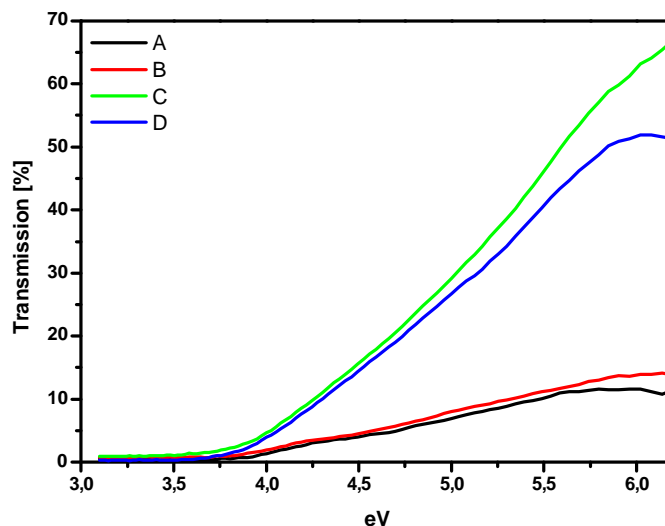
Figure 4.1: UV/Vis spectra of AHM and AHM+AMT solutions in the ligand-metal charge transfer region at different pH values: A. AHM at pH = 5.1, B. AHM+AMT at pH = 5.1, C. AHM+AMT at pH = 3.5, D. AHM at pH = 3.5

Further experiments concerning pH and conductivity measurements as well as in situ UV/Vis spectroscopy were carried out in a computerised preparation machine. The addition of the vanadyl oxalate solution into the AHM solution was carried out by Ismatec micro pumps, the data recording is done by a computer at a sampling rate of 1 Hz. The pH electrodes and conductivity probes are calibrated to respective temperatures. After mixing was finished the prepared solution underwent a heating to 353K for one hour.

UV/Vis spectroscopy was carried out on a UV-2501 PC Shimadzu instrument. Whilst a 0.001 mm quartz cuvette was used for the region 3.7 eV to 6.2 eV, the spectral range from 1.8 eV to 5 eV was investigated by using a 0.006 mm quartz cuvette. Fibre reflection UV/Vis spectroscopy was performed on a Ocean Optics SD 2000 spectrometer equipped with a 600 lines/mm grating. As reflectant boron nitride (BN) [Alfa Aesar, hexagonal, 325 mesh, ~78 µm] was chosen.

The fibre has got a 8 around 1 configuration and a halogen lamp was used as light source. The spectrometer was calibrated to a solution containing 10 g BN per one litre of water. The calibration was done in the reaction vessel under reaction conditions. Outside light was excluded by foil coverage. The reaction mixture (composition see above) contained the same amount of BN. Comparison between the traditional transmission spectra and the reflectance in-situ spectra shows identical band positions. Some intensities are inverted

due to crystallisation onto the BN particles but this should not derange the reaction pathway because without BN an inhomogeneous crystallisation prevails.

The ESR spectra were obtained with a Bruker ESP-500 spectrometer with 100 kHz field modulation. The spectra were recorder at 77K. A g-factors were determined using DPPH as a standard. The accuracy of the g-factors measurements was not higher than 0.01. The line width was measured with the accuracy 10 G (10 G=1 mT).

The number of VO^{2+} ions was determined by a method of double integration of the experimental first derivative spectrum previously described by Blumenfeld *et.al.*[27] and by comparison of the spectral intensity of each sample with a calibration curve obtained by recording the spectral intensity of several solutions of VOC_2O_4. In the range of concentration adopted the calibration was linear.

[95]Mo NMR spectra have been recorded on an MSL-400 Bruker spectrometer at a frequency 26.08 MHz, with 20 KHz sweep width, 20 μs pulse width and 1 s interpulse delay using 1M Na_2MoO_4 as an external standard.

4.3 RESULTS

4.3.1 UV/Vis spectroscopy

Fig. 4.1 shows UV/Vis spectra obtained in the 3.7-6.2 eV region of the ligand-metal charge transfer for the pure AHM and mixed binary (AHM+AMT) solutions prepared at different pH values. Acidification of the AHM solution to 3.5 pH by adding oxalic acid led to a significant increase in absorption in the ligand-metal charge transfer region. This effect can be assigned to protonation of the heptamolybdate species as well as to the structural rearrangements leading to the formation of octamolybdates.

Indeed the species $(HMo_7O_{24})^{5-}$ has been reported at pH = 2.5[22], also a similar effect was observed on calculated spectra[29]. Favourable sites for protonation of the $[Mo_7O_{24}]^{6-}$ ions are the twelve terminal oxygen atoms of the complex[37;38]. In this pH range the reaction to $[Mo_8O_{26}]^{4-}$ occurs[24;25;47;48;41-45;50]. Addition of AMT to AHM to a ratio of 9% (W/(W+Mo)) also increased the intensity of absorption; this effect was small at pH = 1 and became larger at pH = 3.5. The doubly protonated metatungstate ion $(H_2W_{12}O_{42})^{10-}$ is reported to be the major species at pH = 3.5[24].

Addition of acidic vanadyl oxalate to AHM led to the decrease of pH and an increase in intensity of the band (Fig. 4.2): again an effect largely due to protonation of the Mo-O species and/or transformation of the heptamolybdate into octamolybdate. The maximum intensity was achieved at 4.6 % of V/(V+Mo), further addition resulted in a slight decrease in intensity. Addition of AMT re-increased the intensity (Fig. 4.2).

For all binary V-Mo solutions the d-d transitions at 2 eV and 1.6 eV that are characteristic for vanadyl species[28-29] are observed though their positions are slightly shifted into lower eV values (see curves in Fig. 4.3 and 4.4). This fact may indicate the interaction of vanadyl ion with Mo complex. After adding vanadyl oxalate to the ratio of 4.6 % in (V/V+Mo) a broad band lying between 2.2 and 2.4 eV appeared. At 18.4 % vanadyl oxalate (V/V+Mo) this band was gaining intensity.
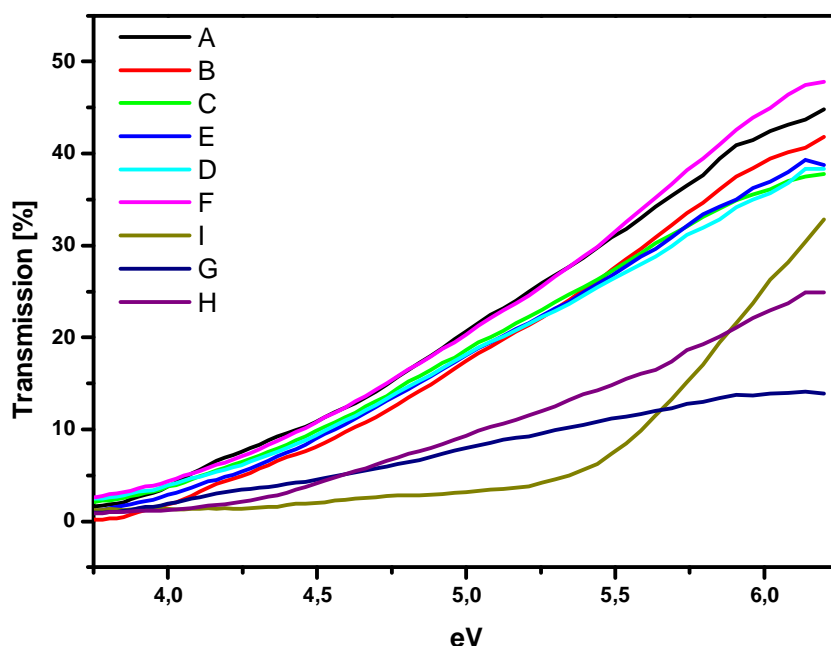
Figure 4.2: UV/Vis spectra of the pure AHM (G), AMT (H), Vanadyl oxalate (I), mixed V/V+Mo at different vanadium concentration (A: 4.6, B: 9.2, C: 13.8, D: 18.4, E: 23%) and ternary ($Mo_{0.68}V_{0.23}W_{0.09}$) (F) solutions in the ligand-metal charge transfer region

It can be assigned towards heteronuclear ligand-metal charge transfer transitions between V and W or Mo[30], meaning the creation of a Mo-O-V type bridge. Such a bridge is

formed by condensation reactions between the protonated W-doped heptamolybdate $[HMo_7O_{24}]^{5-}$ or octamolybdate $[HMo_8O_{26}]^{3-}$ and the vanadyl oxalate.

Addition of AMT did not change the shape of the spectral features, whereas the intensity of the signal has diminished. Addition of tungstate to the mixed AHM/vanadyl oxalate solution enhances both the band assigned to protonation and the band assigned to condensation, these processes are increased by tungstate addition.

4.3.2 Conductivity measurements
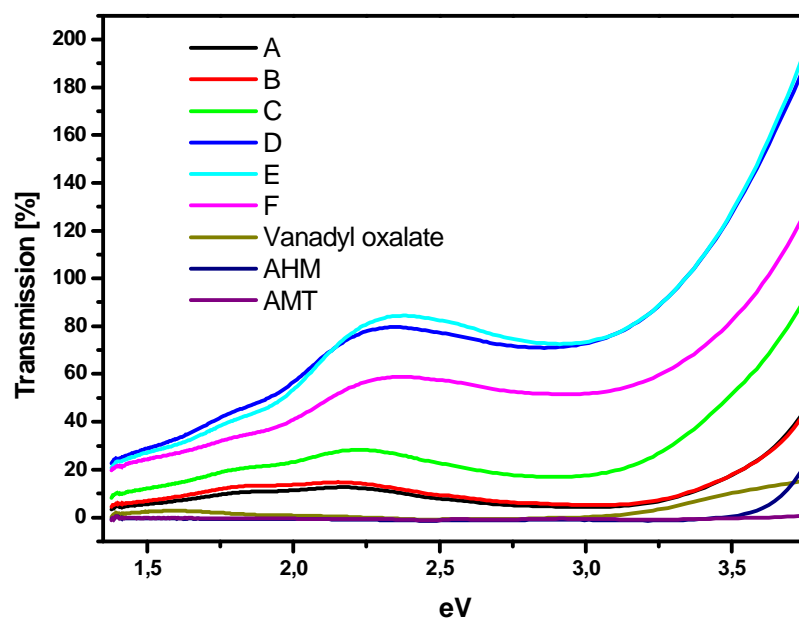
Figure 4.3: UV/Vis spectra of pure AMT, mixed V/V+Mo at their different ratios (A: 4.6, B: 9.2, C: 13.8, D: 18.4, E: 23%) and ternary ($Mo_{0.68}V_{0.23}W_{0.09}$) (F) solutions in d-d transition region

This model is further supported by pH and conductivity measurements. Fig. 4.5 shows the conductivity displayed against the pH. Acidification of the heptamolybdate caused by addition of the vanadyl oxalate solution leads at first to an increase in conductivity. Such a behaviour is expected because of additional fast charge carriers such as protons. The conductivity reaches a maximum at pH=4.5, further vanadyl oxalate addition causes a

decrease in pH: This effect can only be attributed to a substantial decrease in the number of charge carriers by condensation reactions.

Addition of AMT solution causes a further substantial decrease in conductivity and therefore enhanced condensation. However, changes in concentration and therefore different activity of the respective species and different hydratisation leading to altered conductivities needs to be taken into account. Different speeds of vanadyl oxalate and AMT addition show different pH conductivity curves. This is a strong indicator, that the protonation and condensation/polymerization processes are kinetically controlled.

4.3.3 ^{95}Mo NMR spectroscopy

It is well established that polynuclear anionic molybdenum oxocomplexes are formed upon acidification of the aqueous solutions of MoO_4 tetraoxoanions[31;32].
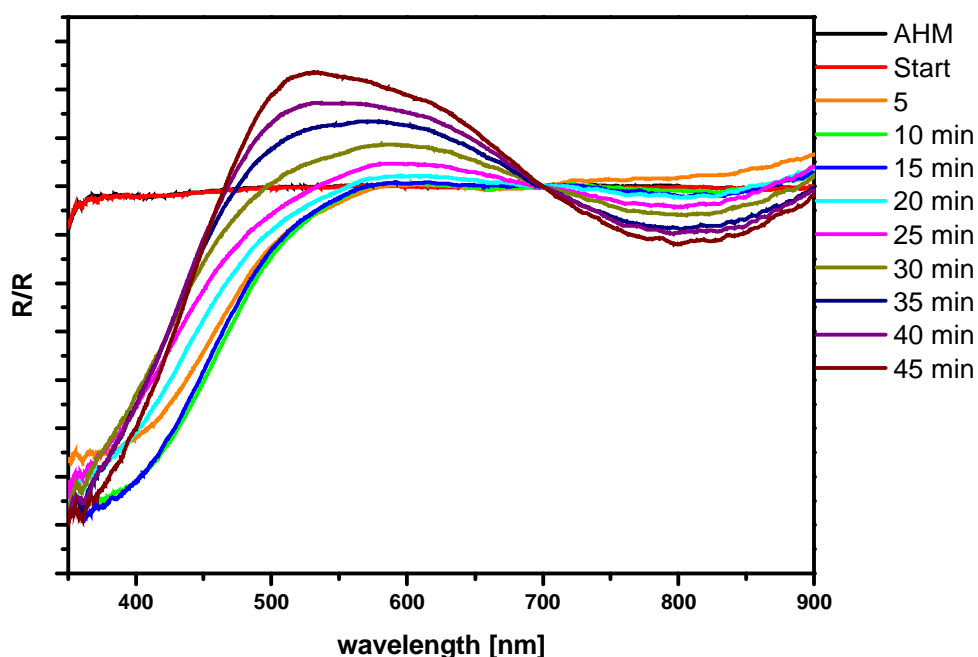
Figure 4.4: In situ UV/Vis characterization; Addition of Vanadyl oxalate (black) and AMT (grey) to AHM; speed of addition 92 ml/min, speed of stirring 200 t/min, spectrum gaining intensity with increasing amount of Vanadyl oxalate

Polycondensation reaction is described as:

$$[MoO_4]^{2-} \longrightarrow [Mo_8O_{26}]^{4-}. \longrightarrow [Mo_7O_{24}]^{6-}$$
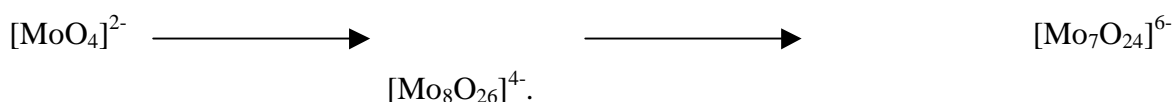
The composition of the polyanions in the solution depends on the acidification degree[24-26;46;47-49]. NMR spectroscopy gives a direct evidence for the type and composition of the polynuclear species. Thus, the ^{95}Mo NMR spectrum of $[Mo_7O_{24}]^{6-}$ consists of two peaks at 200 and 32 ppm with the intensity ratio of 1:6[23;33;38;39]. The spectrum of $[Mo_8O_{26}]^{4-}$ in the aqueous solution represented by two peaks situated at about 100 and 10 ppm[32;38].
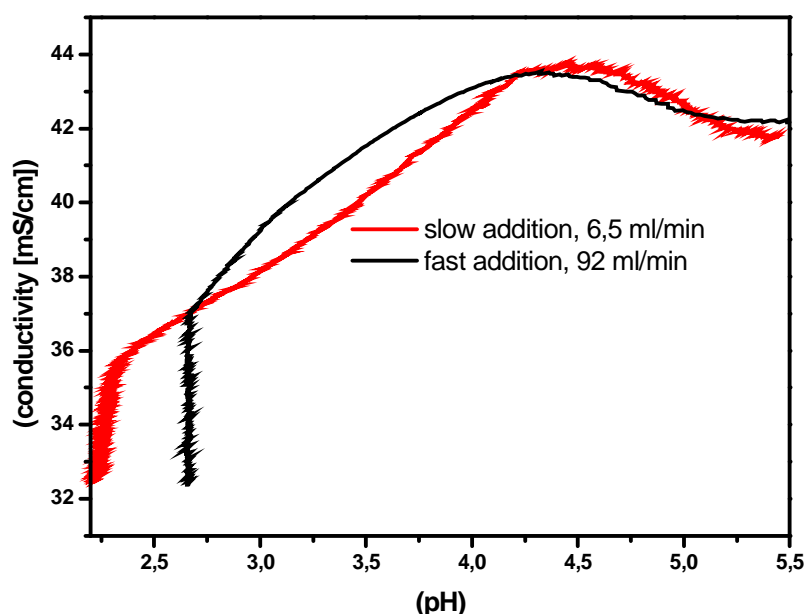
Figure 4.5: Conductivity against pH. Addition of Vanadyl oxalate and AMT to AHM; speed of addition 6.5 ml/min and 92 ml/min, speed of stirring 200 t/min

Fig. 4.6 shows the ^{95}Mo NMR spectrum of the AHM precursor solution. By the position of two peaks (32.8 and 210 ppm) visible in the spectrum (curve 1) species in this solution are identified as those of $[Mo_7O_{24}]^{6-}$ that are in line with the literature data. After addition of AMT to AHM an additional peak with 24.5 ppm appears in the NMR spectrum, at the same time, the position of the peak at about 32 ppm does practically not change (see curve B in Fig. 4.6).

Earlier data[23;32-33] indicates that Mo^{6+} could be substituted by W^{6+} and form mixed heptametalates of $[Mo_7O_{24}]^{6-}$ type in the weak acidic solutions with a pH between 6 and 4. This complex is stable at the wide range of the ratios between the components ($Mo_{7-x}W_xO_{24}$ with x=1-6). In the binary solution under study the ratio between Mo and W is equal to 7.5 that is why two peaks are observed in the spectra: the bigger one corresponds to the pure $[Mo_7O_{24}]^{6-}$ complexes, and the smaller one arises due to the appearance of the same species promoted by tungsten.

After addition of the vanadyl oxalate to the binary solution the shape of the NMR spectrum has drastically changed. The peak at 210 ppm disappeared from the spectrum; the broadened band at about 99 and peak at 4.3 ppm became visible (curve D). The band position fits more closely to $[Mo_8O_{26}]^{4-}$ rather than $[Mo_7O_{24}]^{6-}$ [32;38].
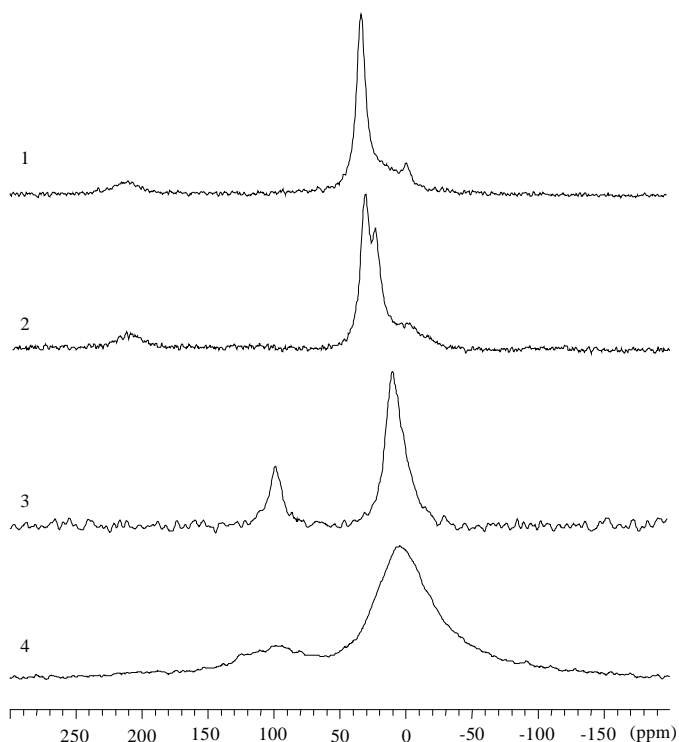
Figure 4.6: **^{95}Mo NMR spectra of AHM (1), binary AHM+AMT (2), $[Mo_8O_{26}]^{4-}$ species (3) and ternary ($Mo_{0.68}V_{0.23}W_{0.09}$) (4) solutions**

The broadening of the signals in the NMR spectrum of the ternary mixed solutions in comparison to the peaks obtained from the pure octamolybdates can be attributed to the effects caused by tungsten doping and by the interaction with VO^{2+} ions. This suggestion is further supported by the fact that no NMR spectrum of the ternary mixed solution peaks responsible for the metatungstates which form in this pH range is observed.

4.3.4 ESR spectroscopy

ESR spectroscopy performed at 77 K and a room temperature did not reveal the presence of Mo^{5+} and W^{5+} in the parent AHM and mixed binary and ternary solutions which indicates that they are all in a diamagnetic oxidation state (6+). Fig. 4.7 shows ESR spectra of the V-Mo solutions with different vanadium concentration and the final ternary mixed solution.

This spectrum is characterised by hyperfine splitting and parameters of $g_{II} = 1.93$ $A_{II} = 200$ Gs and $g_{\perp} = 1.975$ $A_{\perp} = 77$ G which has been assigned to the isolated vanadyl ions in the distorted octahedral environment[34;35]. However, additional peaks of the low intensity closely situated at the parallel components of the hyperfine splitting are observed in the ESR spectrum (see Fig. 4.7).
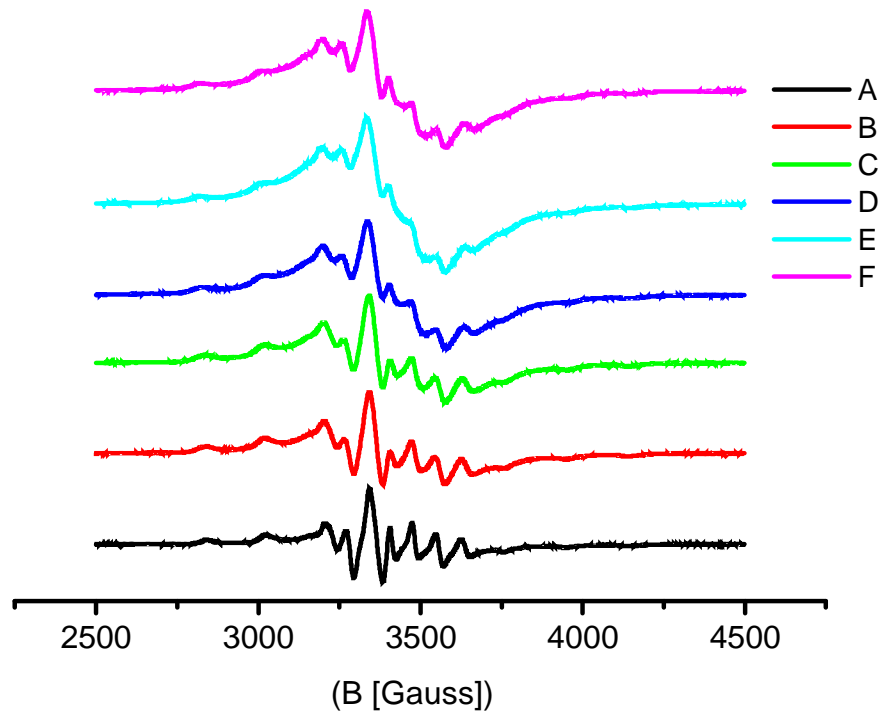
Figure 4.7: ESR spectra of the binary AHM and vanadyl oxalate solutions containing the following ratios of V/(V+Mo): 4.6% (A) 9.2% (B) 13.8% (C) 18.4% (D) and 23 % (E) and mixed VMoW solution (F). DPPH was taken as standard

These lines could be assigned to the vanadyl ions (VO^{2+}) but due to the low intensity of additional maxima exact spectral parameters of this type could not be evaluated properly.

After increasing the vanadium content in the solution (over 13.8 %) the appearance of the slightly anisotropic and broad line with $g_{eff} = 1.96$ and $g_{II} < g_{\perp}$, along with the earlier observed spectrum, are registered by ESR. Similar spectra are observed for the MoVW mixed solution (see Fig. 4.7) and the concentration of the isolated vanadyl ions in the MoVW solution does not exceed 10 %.

Broadening of ESR signals may be caused by the formation of associated V^{4+} ions. According to[40] in the case of the formation of associated species $g_{eff} \cong 1/3 [g_{II}+2g_{\perp}]$, and this ratios is valid for ESR spectrum of complex solution. Therefore, we suggested that a broad and anisotropic ESR signal observed for the ternary solution could be assigned to the associated vanadyl ions in the distorted octahedral coordination.

From the other side, it is well known[61] that magnetic exchange in $-VO^{2+}$-O-VO^{2+}-assosiates is so strong that ESR spectra from these species are practically not observed, e.g. in V_2O_4. Due to this fact one of the explanations of the broadening of ESR spectrum given in Fig. 4.7 is associated with a possible presence of species of VO^{2+}-O-Mo^{6+}-O-VO^{2+} -type with magnetic exchange through diamagnetic Mo^{6+} ions in the solutions.

This interaction of VO^{2+} species through Mo^{6+} ions is weaker than that between pure vanadyl ions but is strong enough to broaden the ESR spectrum. The interpretation is in line with UV/Vis spectroscopic data and conductivity measurements indicating the formation of Mo-O-V type bridges.

4.4 DISCUSSION

This work shows the highly complex interaction between the initial compounds AHM, AMT and vanadyl oxalate. During the mixing process several reactions are happening simultaneously and lead to an important precursor for the final Mo_5O_{14} structure. Although the current literature describes either only the binary systems Mo-V and Mo-W [51;24-26;52-57], a reaction mechanism can be set up that is based on the current literature as well as on the UV/Vis, conductivity, ESR and ^{95}Mo NMR measurements shown in this work.

UV/Vis spectroscopy and the conductivity experiments have shown that addition of vanadyl oxalate to ammonium heptamolybdate leads to kinetically controlled protonation- and condensation reactions.

$$[Mo_7O_{24}]^{6-} + H^+ \xrightarrow{\ k_1\ } [HMo_7O_{24}]^{5-} \text{ (Protonation)}$$

$$8[Mo_7O_{24}]^{6-} + 20H^+ \xrightarrow{\ k_2\ } 7[Mo_8O_{26}]^{4-} + 10H_2O \text{ (Octamolybdate formation)}$$

$$2n[HMo_7O_{24}]^{5-} + nVO^{2+} \xrightarrow{\ k3\ } [Mo-O-(VO)-O-Mo]_n + nH_2O \text{ (Condensation)}$$

$$2n[HMo_8O_{26}]^{3-} + nVO^{2+} \xrightarrow{\ k4\ } [Mo-O-(VO)-O-Mo]_n + nH_2O \text{ (Condensation)}$$
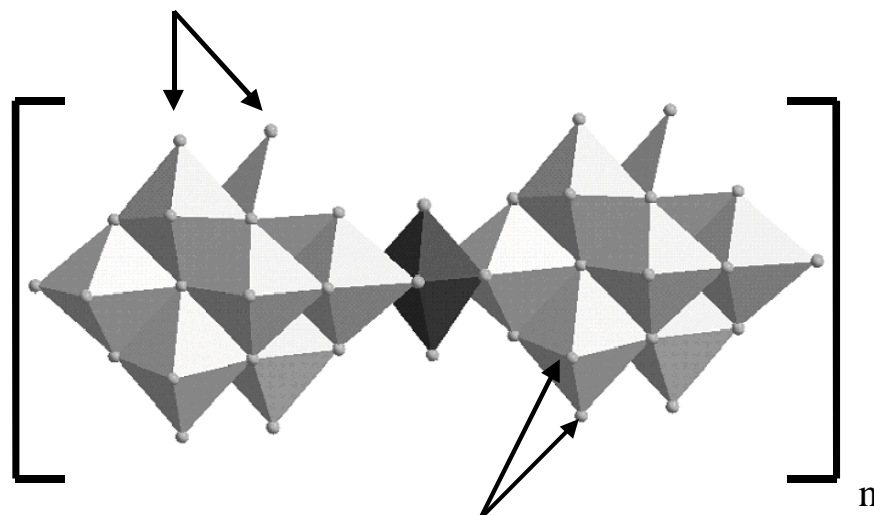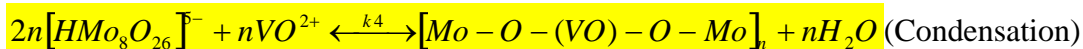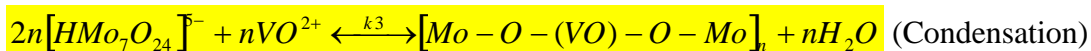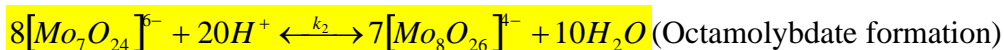
Figure 4.8: Connection between the octamolybdate units. The arrows denote further terminal oxygen atoms, where additional vanadyl groups can connect

Addition of the vanadyl oxalate is the rate-determining step. Whilst quick addition leads to higher polymerisation/condensation products, slower addition leads to a higher proton concentration (lower pH), as observed (Fig. 4.5). In parallel protonated AHM is transferred into octamolybdate. As bond distances in the octa- and heptamolybdate are completely different this is one reason for the decisive changes in the UV/Vis spectra.

Further support is drawn from the [95]Mo NMR study presented above that formation of $[Mo_8O_{26}]^{4-}$ -type species is dominant in the MoVW mixed solutions (see also [24-28;41-50]). These findings are in line with a long series of pH dependent investigations of polyoxometallate chemistry. This complex depicted in Fig. 4.8 has 14 terminal and 12 bridging oxygen bonds. Terminal bonded oxygen atoms can be easily protonated and react with the vanadyl cations[37;38]. Earlier Raman spectroscopy on this system[20] revealed the formation of the molybdate species that are linked via Me-O-Me bridges, and the UV/Vis and ESR measurements specified these bonds as VO^{2+}-O-Mo^{6+}-O-VO^{2+} bridges.

The recent findings in this work have been summarised in Fig. 4.8-4.10 The vanadyl group links discrete $[Mo_8O_{26}]^{4-}$ and $[Mo_7O_{24}]^{6-}$ species in solution and form a polymer consisting of $[Mo_8O_{26}]^{4-}$ and $[Mo_7O_{24}]^{6-}$ units where Mo atoms are partially substituted

by W. In this polymer the vanadyl ion is interconnected via the four oxygen atoms of the equatorial plane of the vanadyl group with the molybdenum atoms possessing terminal oxygen bonds from isolated $[Mo_8O_{26}]^{4-}$ complexes. An octahedral coordination can be completed by water (Fig. 4.9). As $[Mo_8O_{26}]^{4-}$ has seven of such coordination sites formation of a three dimensional oligomeric network is likely (Fig. 4.10).

According to[24] tungsten enhances the oligomerisation because tungsten-oxygen bonds are much more favourable sites for protonation; hence the tendency of tungsten to form chains is stronger. This is in line with various literature findings. Krebs *et al.* report polymers consisting of $Mo_8O_{27}^{6-}$ units interlinked by an europium species. In hydrothermal conditions these polymers are found and octamolybdate can polymerise as well[42;45;51;54-57].

In parallel to the oligomerisation process there is also internal isomerisation of the octamolybdate units. Klemperer used ^{17}O-NMR spectroscopy as a structural probe to investigate the polymetallate chemistry in solution[58]. Especially α-$[Mo_8O_{26}]^{4-}$ shows a very dynamic behaviour in solution including the breaking of Mo-oxygen bonds[59]. A detailed mechanism is suggested by Klemperer *et al.* how this rearrangement and isomerisation reaction between α,β, and γ-$[Mo_8O_{26}]^{4-}$ occur. In systems containing only Mo a pentagonal bipyramide is achieved at low pH (e.g. in $[Mo_{36}O_{112}]^{8-}$)[60]. It is highly likely that during these reactions the mainly edge sharing connections in the heptamolydates and octamolybdates are broken and corner-sharing types are built up which dominate the Mo_5O_{14}-type structure (Fig. 4.10).

Müller *et al.* point out the structural similarities between the Mo_5O_{14} type structure and the $Mo_{36}(H_2O)_{24}O_{96}$[14-17]. Therefore, the reactions leading to these compounds should be very similar. Krebs *et al.* suggest from the analysis of the single crystal x-ray data that $[Mo_7O_{24}]^{6-}$ acts as nucleus for the formation of $[Mo_{36}O_{112}]^{8-}$ and identifies water as an important bridging ligand[48;49]. The removal of water could therefore lead to the breakdown of the $K_8Mo_{36}O_{112}(H_2O)_{16}$ unit and lead to the formation of the Mo_5O_{14} type solid. Knobl *et al.*[20] observed several releases of water by thermo gravimetric experiments.

At least one more element apart from Mo seems to be necessary for that. It is therefore likely that the presence of tungsten in the octamolybdate units favours the formation of the pentagonal bipyramides.

Molecular structures close to those observed in the solutions can be preserved by spray drying[20]; calcination of the spray dried material leads to the final $(MoVW)_5O_{14}$. Thus, the
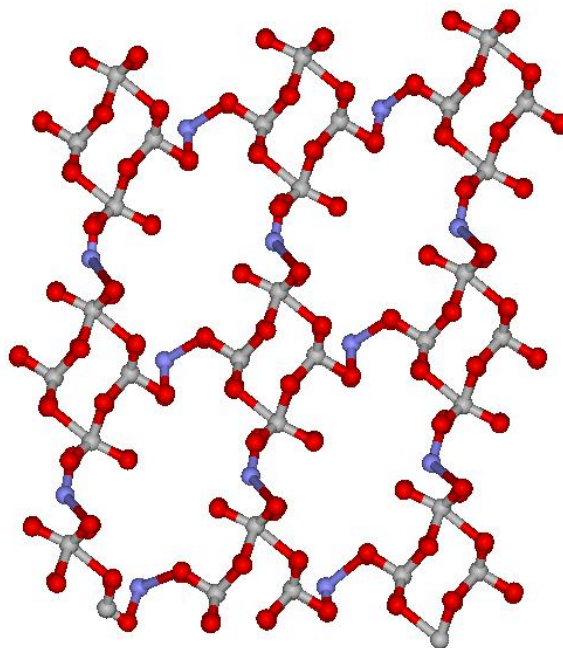
Figure 4.9: Three dimensional connections of octamolybdate units via vanadyl ions (Mo = light grey, O = red, V = blue)

main steps of the formation of the precursor solution of the complex MoVW catalyst are described as follows. Upon mixing of AHM and AMT solutions pure $[Mo_7O_{24}]^{6-}$ complexes along with W doped $[Mo_7O_{24}]^{6-}$ species appear. Addition of the Vanadyl oxalate to the binary mixture leads to the protonation of the molybdate isopolyanions and their transformation into the $[Mo_8O_{26}]^{4-}$ -type structure. The formed species become interconnected with each other via vanadyl groups such providing a kind of the oligomeric network. Incorporation of tungsten into the octamolybdate units leads to formation of the pentagonal bipyramidal motive.

4.5 CONCLUSIONS

This work has substantially increased the understanding of the detailed synthesis routine towards a single $Mo(VW)_5O_{14}$ oxidation catalyst. By using UV/Vis, ESR and ^{95}Mo NMR spectroscopy the nature of molybdate species in the AHM, AMT and mixed precursor solutions of the ternary mixed oxide was studied. Results obtained show that structure
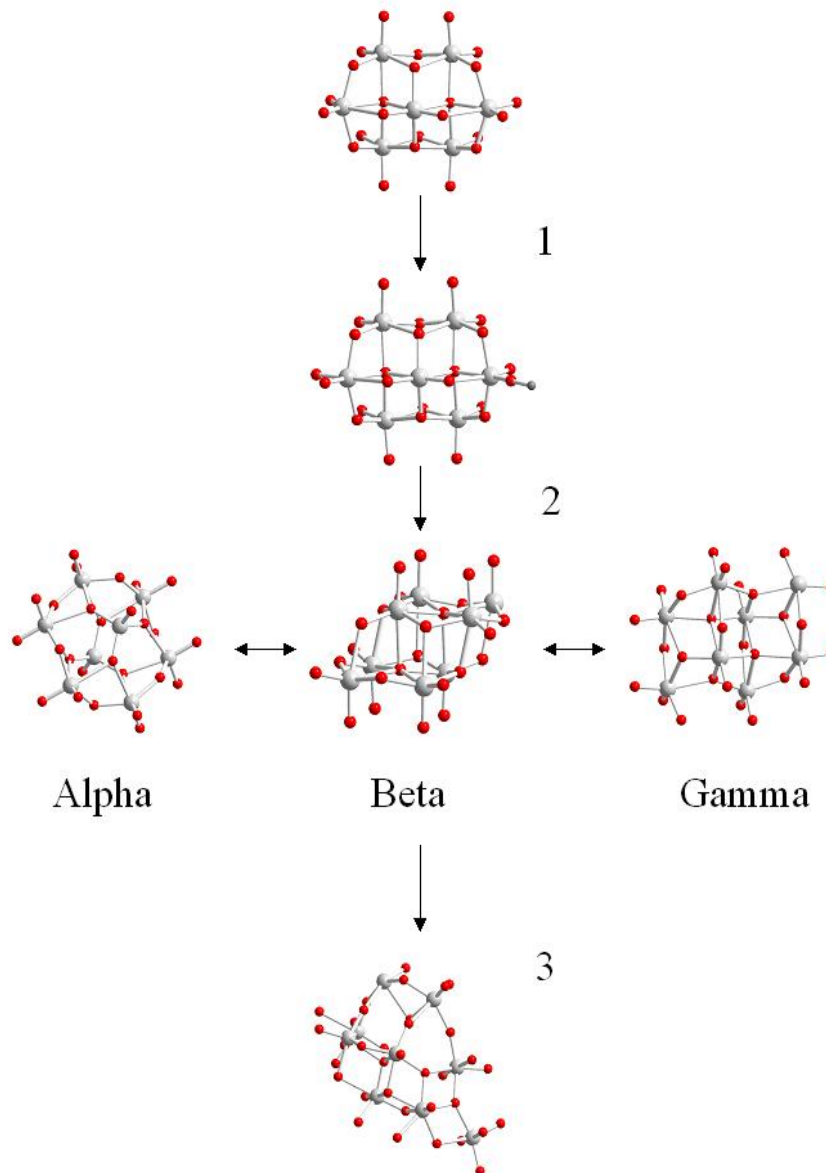
Figure 4.10: Reaction steps. 1: Protonation of the heptamolybdate, 2: Formation of octamolybdate (3 modifications), 3: Formation of the pentagonal bipyramidal motif following a mechanism set up by Klemperer [58]

formation starts as early as during the mixing process of the initial precursor solutions. Addition of acidic vanadyl oxalate causes protonation and condensation of the heptamolybdate ions into octamolybdate ions that are linked by vanadyl species and form a polymeric network. Addition of tungsten atoms clearly enhance this process. This polymeric network is an essential precursor for the final Mo_5O_{14} –type structure.

Reference List

[1.]   N. Kurtz, R. W. Cunningdam, A. W. Naumann (Union Carbide Co.) [US 4111983] (1978).

[2.]   V. Novak, L. Sokol, J. Jelinek, [CS 1207807] B(1981).

[3.]   N. Bertolini, S. Ferlazzo (Euteco Impianti S.p.A.) [US 4289654] (1981).

[4.]   T. Kawajiri, S. Uchida, H. Hironaka (Nippon Shokubai Kagaku) [EP 427 508 A1] (1991).

[5.]   F.-G.Tenten, H. Martin, H. Hibst, L. Marosi, V. Kohl (BASF AG), [EP 668104 B1] (1995).

[6.]   H. Hibst, S. Unverricht (BASF), [DE 19815281 A 1].

[7.]   M. Tanimoto, H. Himeji-shi, I. Mihara, H. H. Aboshi-ku, T. Kawajiri, H. Himeji-shi, (Nippon Shokubai), [EP 0 711 745 B1].

[8.]   F.-G. Tenten, H. Hibst, H. Martin, L. Marosi, V. Kohl (BASF), [DE 4405514 A1].

[9.]   G. Mestl, Ch. Linsmeier, R. Gottschall, M. Dieterle, J. Find, D. Herein, J. Jäger, Y. Uchida, and R. Schlögl, *J. Mol. Catal. A*, 2000, **162**, 455.

[10.] O. Ovsitser, Y. Uchida, G. Mestl, G. Weinberg, A. Blume, M. Dieterle, H. Hibst, and R. Schlögl, *J. Mol. Catal. A*, 2002, **185**, 291.

[11.] M. Dieterle, G. Mestl, J. Jäger, Y. Uchida and R. Schlögl, *J. Mol. Catal. A*, 2001, **74**, 169.

[12.] L. Kihlborg, *Ark Kemi*, 1963, **21**, 427.

[13.] A. Müller, P. Kögerler, C. Kuhlmann, *Chem.Comm.*, 1999, 1347-1358.

[14.] L. Cronin, P. Kögerler, A. Müller, *Journal of Solid State Chemistry*, 2000, **152**, 57.

[15.] I. Paulat-Böschen, *J.C.S. Chem. Comm.*, 1979, 780.

[16.] B. Krebs, I. Paulat-Böschen, *Acta Cryst.*, 1982, **B 38**, 1710.

[17.] T. Yamase, P.V. Prokop, *Angew. Chem. Internat. Ed.*, 2002, **114**, 3, 484.

[18.] T. Ekström, M. Nygren, *Acta Chem. Scand.*, 1972, **26**, 1827.

[19.] T. Ekström, M. Nygren, *Acta Chem. Scand.*, 1972, **26**, 1836.

[20.] S. Knobl, G. A. Zenkovets, G. N. Kryukova, O. Ovsitser, D. Niemeyer, R. Schlögl, and G. Mestl, *J. Catal.,* 2003, **215**, 177.

[21.] M.T. Pope, *Heteropoly and Isopoly Oxomatallate*, Springer-Verlag, Berlin, 1983.

[22.] J.J. Cruywagen, B. Krebs, I. Paulat-Böschen, *Acta, Cryst. Sect. B*., 1976, **B32**, 1697.

[23.] R.I. Maksimovskaya, K.G. Burtseva, *Polyhedron*, 1985, **4**, 1559.

[24.] J.J. Cruywagen, *Advances in Inorganic Chemistry*, 2000, **49**, 127.

[25.] J.J. Cruywagen, B.B. Heyns, *Inorg. Chem.*, 1987, **26**, 2569.

[26.] J.J. Cruywagen, A.G. Draaijer, J.B.B. Heyns, E.A. Rohwer, *Inorganica Chimica Acta*, 2002, **331**, 322.

[27.] A.A. Blumenfeld, V.V. Voevodskii, A.G. Semenov, *Application of Electron Paramagnetic Resonance in Chemistry*, Nauka, Novosibirsk, 1962 [in Russian].

[28.] J. Ballhausen, H. B. Grey, *Inorg. Chem.*, 1962, **1**, 111.

[29.] A.B.P. Lever, « Inorganic electronic spectroscopy », 1984, Elsevier (Amsterdam, Oxford, New-York, Tokyo).

[30.] L. David, C. Craciun, M. Rusu, O. Cozar, P. Ilea, D. Rusu, *Polyhedron*, 2000, **19**, 1917-1923.

[31.] S.F. Gheller, M. Didney, A.F. Masters, *Austr. J. Chem.*, 1984, **37**, 1825.

[32.] P. Sarrazin, B. Mouchel, S. Kazstelan, *J. Phys. Chem*, 1989, **93**, 904.

[33.] I. Andersson, J. J. Hastings, O. W. Howarth, L. Pettersson, *J. Chem. Soc. Dalton Trans.*, 1994, 1061.

[34.] M.C. Paganini, L. Dall'Acqua, E. Giamello, L. Lietti, P. Forzatti, G. Busca, *J. Catal.*, 1997, **166**, 195.

[35.] F. Kubec, Z. Sroubek, *J. Chem. Phys.*, 1972, **57**, 1660.

[36.] Y.Y.H. Chao, D.R. Kearns, *J. Phys. Chem.*, 1977, **81**, 666.

[37.] J.P. Jolivet, M. Henry, J. Livage, E. Bescher, Metal Oxide Chemistry and Synthesis: From Solution to Solid State, John Wiley & Sons, Chichester, 2000, p. 20.

[38.] O.W. Howarth, P.J. Kelly, *J. Chem. Soc. Dalton Trans.* 1990, 81-84**.**

[39.] O.W. Howarth, P.J. Kelly, *Chem. Soc. Chem. Comm.*, 1988, 1236.

[40.] S.A. Al'tshuler, B.M. Kozyrev, «Electronic paramagnetic resonance of the compounds of elements of transition metals», Nauka, Moscow, 1972 [in Russian].

[41.] J. Fuchs, H. Hartl, *Angew. Chem.* 1967, **88**, 385.

[42.] J. Fuchs, H. Hartl, W.D. Hunnius, S. Mahjour, *Angew. Chem.* 1975, **87**, 634.

[43.] I. Paulat - Böschen, B. Buss, B. Krebs, *Acta Cryst.* 1974, B30, 48.

[44.] O. Glemser, G. Wagner, B. Krebs, *Angew. Chem.* 1970, **82**, 639.

[45.] I. Paulat - Böschen, B. Buss, B. Krebs, O. Glemser, *Angew. Chem.* 1973, **85**, 409.

[46.] J. Aveston, E.W. Anacker, J.S. Johnson, *Inorg. Chem.* 1964, **3**, 735.

[47.] H. Tytko, G. Baethe, E.R. Hirschfeld, K. Mehmke, D. Stellhorn, *Z. anorg. allgem. Chem.* 1983 503, 43.

[48.] K. H. Tytko, O. Glemser, *Adv. Inorg. Chem. Radiochem,* 1976, **19**, 239.

[49.] O. Glemser, W. Holznagel, S. Iftikhar Ali, *Z. Naturforschung, 1965*, **20b**, 192.

[50.] J. Bridgeman, *J. Phys. Chem. A.*, 2002, **106**, 12151.

[51.] B. Krebs, I. Loose, M. Bösing, A. Nöh, E. Droste, *C. R. Acad. Sci. Paris, t. 1,* **Serie II c**, 1998, 351.

[52.] T. Pope, *Progress in Inorganic Chemistry*, 1991, **39,** 181.

[53.] A. Müller, F. Peters, M. T. Pope, D. Gatteschi, *Chem. Rev.*, 1998, **98**, 239.

[54.] G. Liu, Y-G. Wei, Q. Yu, Q. Liu, S-W. Zhang, *Inorganic Chemistry Communications*, 1999, **2**, 434.

[55.] R. Villanneau, A. Proust, F. Robert, F. Villain, M. Verdaguer, P. Gouzerh, *Polyhedron*, , 2003, **22,** 1157.

[56.] C-L. Pan, J-F. Song, J-Q. Xu, G-H. Li, L. Ye, T-G. Wang, *Inorganic Chemistry Communications*, 2003, **6**, 535.

[57.] R. S. Raring, L. Bewley, J. Zubieta, *Inorganic Chemistry Communications*, 2003, **6,** 539.

[58.] W.G. Klemperer, *Angew. Chem. Int. Ed.*, 1978, **17**, 246.

[59.] V.W. Day, M. F. Frederich, W. G. Klemperer, W. Shum, *J. Am. Chem. Soc.*, 1977, **99**, 952.

[60.] R. Schlögl, D. Niemeyer, S. B. A. Hamid, O. Timpe, S. Knobl, D. Othman, N. Abdullah, *Topics in Catalysis*, 2003, submitted.

[61.] C.P. Slichter, in *Principles of Magnetic Resonance*, Harper-Row, New York, 1963.

5 The Synthesis and Structure of a Single Phase, Nanocrystalline MoVW Mixed Oxide Catalyst of the Mo$_5$O$_{14}$-Type

5.1 INTRODUCTION

About one quarter of all organic products produced world-wide are synthesised via catalytic selective partial oxidation reactions. The industrial and economic relevance of research in this field, hence is self evident. Generally, these industrial processes are highly developed. Improvements of such processes can only be achieved if fundamental understanding is reached about the active catalyst structures and their relation to the catalytic performance.

Currently, MoVW supported catalysts are used in industry for the synthesis of acrylic acid[1-5]. Despite this industrial importance, fundamental information is not available neither on the structure formation during synthesis nor on the peculiarities of the atomic arrangements in these systems depending on different preparation routes and element ratios.

Previously, the Mo$_5$O$_{14}$-type phase was found to be highly important for selective partial oxidation catalysis for example methanol oxidation[6], acrolein oxidation[7], and propene oxidation[8]. Proceeding work[6-9] showed that the selectivity for partial oxidation products could be considerably augmented when the amount of Mo$_5$O$_{14}$ was increased. The structure of this oxide is built up by pentagonal bipyramids and octahedrally co-ordinated metal centres[10]. Coordination sphere changes can easily be imagined in this structure which might explain its activity in partial oxidation catalysis. This oxide forms at a definite transition metal ratio of Mo:V:W equal to 0.68:0.23:0.09. At the same time binary molybdenum based oxides doped with different elements such as Nb, W and Ta have been synthesised and their structure was identified as that of the Mo$_5$O$_{14}$-type[11;12]. These phases were found to be stable at a wide temperature range and a broad variation of the element ratios. However, the ternary system has not yet been synthesised as a single phase material without traces

of other molybdenum oxides, e.g. thermal treatment in inert atmosphere results in the appearance of MoO_2, while treatment in air leads to MoO_3.

Its identification as an important phase for partial oxidation catalysis, makes this $(MoVW)_5O_{14}$ oxide also important as a model substance for fundamental surface science studies, provided single crystals could be grown. Attempts to grow single crystals via gas phase transport reactions or sintering[8;13;14] showed that this phase forms from mixtures of molybdenum and tungsten, from mixtures of molybdenum, tungsten and vanadium, but not in case of binary Mo-V mixtures with high V concentrations. Both tungsten and vanadium play important roles as structural promoters in the formation and stabilization of this oxide and hence for catalytic activity.

It seems plausible that different thermal treatments of the precursor solutions effect a) the composition of the usually mixed phase catalysts and b) the crystal sises of the different constituting phases. Thus, the understanding of the aqueous precursor chemistry is required to control the preparation of such mixed oxide catalysts. Furthermore, subsequent drying and activation procedures from the liquid precursor to the active and selective catalyst are of paramount importance for the development of the optimum catalytic performance. Accordingly, knowledge has to be generated about the detailed processes which occur during these synthesis steps. Only then, it might be possible to fully control not only the phase composition of the mixed oxide catalyst, but also the crystal size, the crystallinity, and the morphology of the active phase. A developed synthesis routine thus could lead to defined crystal sizes or even nano-crystalline $(MoVW)_5O_{14}$ mixed oxide catalysts. Moreover, it offers a versatile path to control its elementary composition. Effects of crystallite size / morphology and elemental composition could be studied separately on the catalytic performance.

To this end, some steps of the developed aqueous preparation procedure are characterised by in situ micro Raman spectroscopy. The important, subsequent drying process as well as further activation and formation procedures are investigated by in situ Raman spectroscopy, HREM and XRD. Comparison with Raman spectra of well defined, single-crystalline reference oxides[13] was used to assign the obtained spectra during these catalyst preparation routes to certain oxides, such as MoO_2, Mo_4O_{11}, Mo_8O_{23}, MoO_3, or Mo_5O_{14}.

This paper was aimed at the preparation of a single phase Mo_5O_{14}-type material and the study of its molecular architecture at every step of the synthesis. Possible changes of the particle morphologies of the ternary oxide and its precursors during thermal treatment were also in the focus of this study. Last but not least, the detected physical alterations during synthesis should be related to the changing catalytic activity and selectivity in the partial oxidation of acrolein.

This approach of a knowledge-based development of all synthesis steps combined with the use of complementary physicochemical characterization techniques led to the defined preparation of a single phase $(MoVW)_5O_{14}$ oxide catalyst for acrolein partial oxidation.

5.2 EXPERIMENTAL

The mixed oxide catalyst with the $Mo_{0.68}V_{0.23}W_{0.09}O_x$ composition was prepared by spray-drying of mixed solutions of ammonium heptamolybdate (AHM, Merck, p.a.), ammonium metatungstate (AMT, Fluka, purum, > 85 % WO_3 gravimetric), and vanadyl oxalate of the respective transition metal concentrations and a pH value of 2. The aqueous solution of AHM with the concentration of 0.963 mol/l MoO_3 was prepared by dissolving AHM in bi-distilled water at 353 K. The aqueous solution of AMT with the concentration of 0.271 mol/l WO_3 was prepared by dissolving AMT in bi-distilled water at 353 K. The aqueous solution of vanadyl oxalate with the concentration of 0.379 mol/l was prepared by dissolving V_2O_5 (Merck, extra pure) in an aqueous solution of oxalic acid (EGA-Chemie, >99%) with the concentration of 1.93 mol/l at 353 K. The different transition metal precursor solutions were allowed to cool to room temperature and then mixed by adding the corresponding amounts with a metering pipette. The mixed solutions were heated at 353 K for 1h.

The $Mo_{0.68}V_{0.23}W_{0.09}$ oxide solid catalyst precursor was prepared by spray-drying the mixtures of the aqueous solutions of AHM, AMT and vanadyl oxalate with a spray-dryer of the `Anhydro´-type. Subsequently, the obtained product was calcined at 623 K for 120 min in flowing air (flow rate: 3.6 l/h) and at 723 K in flowing helium (flow rate: 3.6 l/h) for 120 min or only at 713 K in flowing air for 240 min. The heating rate to these end temperatures was 6 K/min. The calcination was done in a gas flow reactor placed in a tube furnace.

The Mo, V, and W concentrations in the precursor solutions, the solid precursor and the catalysts were determined by Atom Absorption Spectroscopy (AAS), Perkin Elmer (PE 4100).

Raman spectroscopy was performed on a Labram I (Dilor) instrument equipped with a confocal microscope (Olympus). A notch filter (Kaiser Optical) was applied to cut off the laser-line and the Rayleigh scattering up to 150 cm^{-1}. The spectrometer is equipped with a CCD camera (1024*298 diodes), which is Peltier cooled to 243 K to reduce the thermal noise. A He-laser (Melles Griot) was used to excite the Raman scattering at 632 nm with a laser power of 1,4 mW. The following spectrometer parameters were used: microscope objective: 100; slit width: 200 μm (spectral resolution: 2.5 cm^{-1}), integration time: 240 s per spectrum and 20 averages.

X-ray diffraction (XRD) analysis was carried out using an URD-63 spectrometer with Cu K$_\alpha$ radiation in the 5 - 70 2Θ range by continuous scanning (2° Θ/min). The integration time was set at 20 s. The POLYCRYSTAL software package[15] was used to refine the structure of the sample calcined in air at 623 K and He at 713 K. Additional X-ray diffraction (XRD) measurements were done at room temperature on a STOE STADI-P focusing monochromatic transmission diffractometer equipped with a Ge(111) monochromator and a position sensitive detector. Cu-K$_a$ radiation was used. The phase analysis was performed with the STOE Win XPOW software package (version 1.06; Stoe Darmstadt, Germany) and with PowderCell (V 2.3; Bundesanstalt für Materialforschung und -prüfung (BAM) Berlin, Germany).

The particle size distribution was measured on a Coulter Counter TA- 2 from Coultronics. The specific surface areas were determined by the BET method (Micromeritics).

The morphology and the size of the catalyst particles after spray-drying and during calcination was determined by SEM analysis. SEM was conducted on a S 4000 FEG microscope (Hitachi). The acceleration voltage was set at 10 kV, the objective aperture was 30 mm, and the working distance was 10 mm.

High resolution transmission electron microscopy (HRTEM) analysis was carried out on a CM 200 electron microscope (Philips) (point resolution: 0.2 nm, acceleration voltage: 200 kV) equipped with an EDX system (EDAX). For HRTEM analysis, the samples were prepared from suspensions of the powders in methanol. A drop of the methanol slurry was put on holey-carbon / copper grids.

Thermal analysis (TA) was performed with a STA 449 C Jupiter apparatus (Netzsch). Flowing helium and air atmosphere were applied (the flow rate was set at 15 ml/min in both cases). The heating rate was set at 10 K/min and 20 K/min. Mass spectrometric analysis (TG-MS) of the evolved gases was performed with an Omnistar quadrupole mass spectrometer (Pfeiffer Vacuum).

The sieve fraction between 0.4 and 0.6 mm of crushed pellets was used for the catalytic measurements. The catalytic tests were performed in a quartz tubular flow reactor (i.d. 4mm). The catalyst (0.025-0.1 g) was diluted with quartz (1:10 –1:4 by weight) to achieve a better temperature control. Reaction mixtures of 4% C_3H_4O, 8% O_2, 20% H_2O, and the balance He with total flow rates between 0.2 to 2 ml/s were used for the catalytic measurements. The reactants and products were analyzed by an on-line gas chromatograph (Varian 3800) equipped with TCD and FID detectors. A Porapak-QS column (2 m×1/8 IN, s.s.) and a 60/80 Carboxen^{TM} 1000 column (15 FTs×1/8 IN, s.s.) were employed for the analysis of permanent gases and organic substrates. The carbon mass balance was 100±5 %.

5.3 RESULTS AND DISCUSSION

5.3.1 SEM

Table 5.1 EDX Result

Elements (At %)	T = 383 K	T = 623 K	T = 713 K
V	18.9	21.2	24.4
W	10.1	11.1	7.3
Mo	70.9	67.7	68.3

Fig. 5.1 A shows a characteristic SEM image of catalyst particles after spray-drying. All particles are spherically shaped and have smooth surfaces. Their sizes range from 2 – 50 μm with main values lying between 5 – 10 μm. The shape and the size of the spherical particles did not change after the calcination in air of the spray-dried material at 623 K. But the observed morphology of the sample has changed after

heating at 713 K in helium or in air. These results are given in Fig. 5.1 B, C. One can see that now the spherical particles consist of numerous smaller particles of regular shape and size ranging from 0.2 to 0.5 μm. The EDX results given in Tab. 5.1 show that the concentrations of the different elements slightly change with thermal treatment.
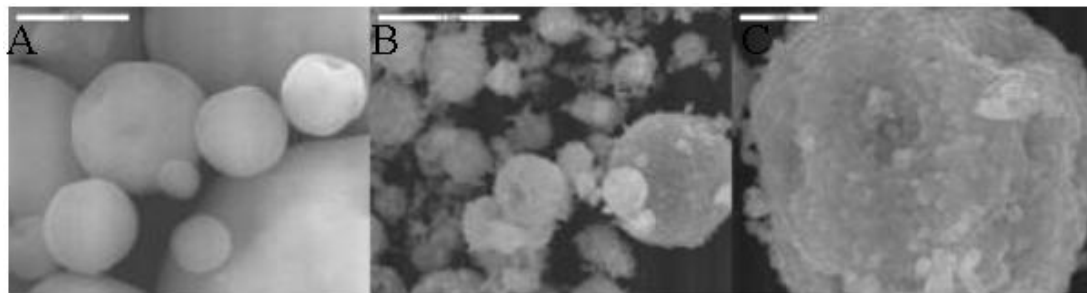
Figure 5.1: Typical SEM images of the spray-dried precursor A), the MoVW oxide catalyst heated at 623 K in air and at 713 K in He B, C) at different magnifications

5.3.2 Particle size distribution and BET surface area

Analysis of particle size distribution shows that most particles have sizes between 5 and 10 μm (59.5 %) and this data is in line with the SEM analysis. About 21 % of the particles are smaller than 5 μm, and a few particles are bigger than 10 μm (19 %). After calcination at 623 K and 713 K, the particle size distribution did not decisively change.

The specific BET surface area of the dried precursor was very low with 0.8 m^2/g, the one of the calcined oxide was 4.1 m^2/g. These values are close to those reported for the industrial MoVW mixed oxide catalyst[6-9].

5.3.3 TG-MS

The TA data of the spray-dried $Mo_{0.68}V_{0.23}W_{0.09}O_x$ sample, measured in flowing synthetic air, is shown in Fig. 5.2. Four main mass losses are observed at 385, 545, 621, and 675 K. DSC performed simultaneously with TA shows endothermic events at 385 K, 525 K and 675 K, and two exothermic effects at 563 K and 621 K, which are similar to the mass losses as evident from the DTG trace.
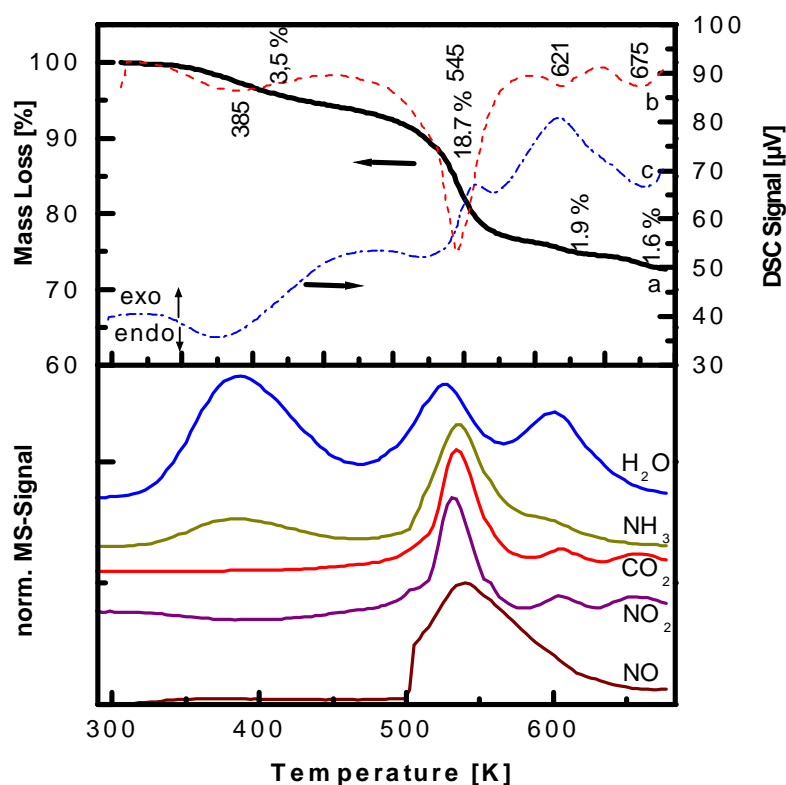
Figure 5.2: TA in flowing synthetic air of the spray-dried $Mo_{0.68}V_{0.23}W_{0.09}O_x$ catalyst. a) **TG data,** b) **DTG data,** c) **DSC data (upper panel); MS traces of evolved H_2O, NH_3, CO_2 NO_2, and NO**

The first endothermic effect is associated with a mass loss of 3.5 % in the TA. As seen from the MS traces, 33.4 % of the total amount of water in the catalyst is released from the sample. Water, carbon dioxide, ammonia and nitrogen oxides are released at the endothermic and exothermic effects at 525 and 563 K, respectively. The release of carbon dioxide is due to the decomposition of vanadyl oxalate. Nitrogen oxides are formed from the oxidation of ammonia and the reduction of the vanadium and molybdenum precursors. An exothermic effect is detected at 621 K, which is related to only a slight mass loss of 3.5 %. Water and traces of ammonia, carbon dioxide and nitrogen dioxide are observed by MS. This exothermic effect is associated with a crystallisation process as revealed by SEM and XRD.

Fig. 5.3 displays the TA data obtained in flowing helium of the sample which was pre-treated in flowing air at 623 K for 2h. Two major mass losses are observed of 4.6
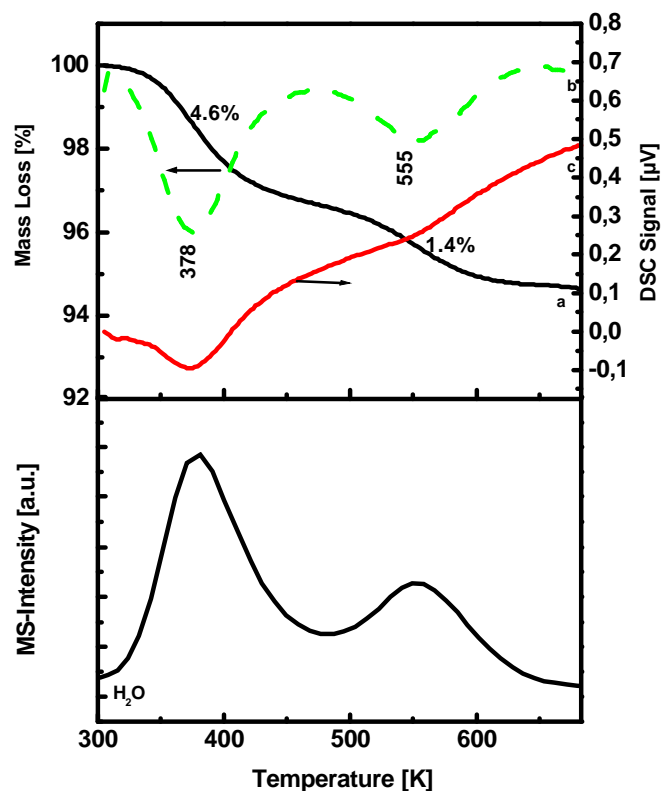
Figure 5.3: TA in helium of the spray-dried $Mo_{0.68}V_{0.23}W_{0.09}O_x$ catalyst pre-treated in air at 623 K for 2h. a) **TG-data,** b) **DTG data,** c) **DSC data (upper panel); lower panel: MS trace of evolved water**

and 1.4 %, respectively. The DSC curve shows endothermic events at 378 K and 555 K, which correlate with the mass losses as also confirmed by the DTG trace. The first effect is accompanied by a mass loss of 4.6 % as shown in the TG curve. The MS-analysis of the evolved gases shows that only water is released from the sample. The second endothermic effect at 555 K is also accompanied by loss of water. Other thermal effects or mass losses were not observed up to 743 K. In this experiment, the release of carbon dioxide or nitrogen oxides was not observed. These compounds obviously were completely released during the pre-treatment of the precursor in air at 623 K for 2h, in line with the TA data shown in Fig. 5.2.

5.3.4 XRD

Fig. 5.4 displays the results of the XRD analysis of the $Mo_{0.68}V_{0.23}W_{0.09}$ mixed oxide samples after the different treatment steps. The XRD pattern shown in Fig. 5.4 of the initial and calcined samples differ considerably. The XRD patterns reveal that the mixed $Mo_{0.68}V_{0.23}W_{0.09}$ oxide precursor was poorly crystallised after spray-drying (Fig. 5.4 a) and after calcination in air at 623 K (Fig. 5.4 b).
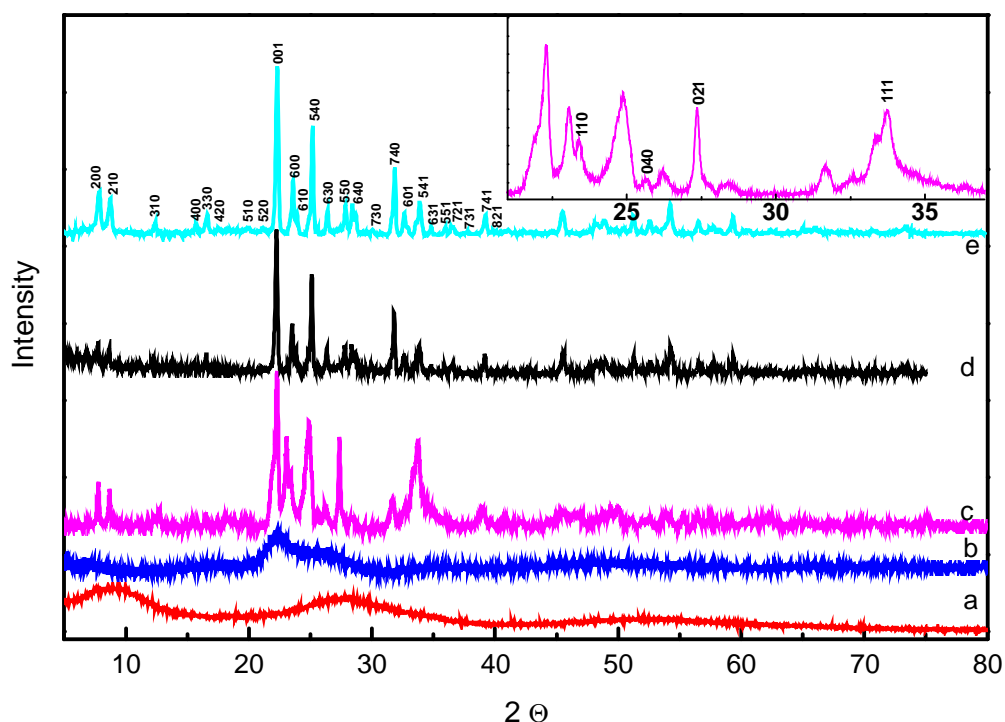
Figure 5.4: X-ray pattern of the MoVW oxide precursor/catalysts: a) spray-dried precursor , b) catalyst calcined in air at 623 K for 2h, c) catalyst calcined in air at 723 K for 2h, d) catalyst calcined in air at 623 K and in helium at 713 K, and e) catalyst calcined in air at 623 K for 2h after operation in acrolein oxidation for 80h. The inset shows the 2Θ region of diffractogram c which shows reflections due to MoO₃

The broad halo lying between 5 and 14° of the spray-dried sample as evident set of reflections of the Mo_5O_{14} this 2θ region (pattern c and d of Fig. spray-dried sample at 623 K in air, the is observed at 22° 2θ in the XRD pattern Fig. 5.4).

2θ is characteristic for the XRD pattern from Fig. 5.4 a. It should be noted that a structure, such as (210), (310), appear in 5.4). After thermal treatment of the halo disappeared and a broad XRD peak of this sample (see diffractogram b of

In this case, the peak location is very close to that of the (001) reflection of Mo_5O_{14}. The spray-dried material shows a second broad signal at 27.6° 2Θ. The broad reflection, observed in this range (pattern a of Fig. 5.4) transforms into a set of sharp

peaks, including the (550) reflection of Mo_5O_{14}, after calcination in air at 723 K (Fig. 5.4 c), and in air at 623 K plus in helium at 713 K (Fig. 5.4 d).

These observations indicate that a Mo_5O_{14}-type structure is pre-formed in the spray-dried precursor but of course with a very low degree of structural ordering within the basal plane. This observation is in agreement with published results of the structural studies of the nanocrystalline, industrial catalyst[6,16].

The XRD pattern of the MoVW sample calcined in air at the higher temperature of 723 K is shown in Fig. 5.4 c. This temperature results in the crystallisation of the complex Mo-V-W oxide of the Mo_5O_{14}-type from the nanocrystalline, spray-dried material as confirmed by the appearance of the sharp and characteristic peaks of this phase in the XRD diffractogram (pattern c of Fig. 5.4).

However, traces of a MoO_3 phase are also detected for this sample. The inset of Fig. 5.4 shows the 2Θ range of the diffraction pattern c, in which the reflections of MoO_3 occur as marked by their respective indices. The result of the assignment of the reflections are given in Tab. 5.2. These XRD data are corroborated by Raman spectroscopy (vide infra). Hence, the single phase $Mo_{0.68}V_{0.23}W_{0.09}$ O compound of the Mo_5O_{14}–type structure could not be identified when the sample was heated in air at 723 K. MoO_3, known for its total oxidation activity, is definitely present in the catalyst.

The single phase $Mo_{0.68}V_{0.23}W_{0.09}O$ compound of the Mo_5O_{14}–type structure is only formed after subsequently heating the catalyst, pre-calcined in air at the lower temperature of 623 K, in helium at 713 K as evident from the XRD pattern d of Fig. 5.4, which additionally shows the indices of the reflections of $Mo_{0.68}V_{0.23}W_{0.09}O$.

It has to be noted that the XRD pattern recorded for the catalyst, which was thermally treated in air at 623 K and then operated in the acrolein oxidation for 80 h (pattern e of Fig. 5.4) is similar to pattern d of Fig. 5.4. This observation confirms recent results on the enhanced formation of the Mo_5O_{14}-type structure during acrolein oxidation[7].

The XRD pattern d of Fig. 5.4. was used for the structural refinement of the ternary oxide sample. According to the results obtained, the structure is well described by the space group P4/nmm with following lattice parameters: a = 4.54063, b = 4.54063, c = 0.39979 nm, respectively. A slight decrease of the unit cell parameters of the

thermo-activated ternary oxide is observed as compared to the reference Mo_5O_{14} Kihlborg[10] (P4/mbm space group, a = 4.5990, b = 4.5990, c = 0.3936 nm).

The incorporation of V and W ions into the structure of this molybdenum oxide could be the reason for this. It was shown above that crystalline particles of this sample have W and V contents as high as 9 and 23 at.%, respectively.

Data given in Fig. 5.4 may provide the supposition that the structure of the spray-dried catalyst precursor only exhibits close-range order rather than nanocrystalline 3D periodicity, because there is only one single halo in XRD pattern, which disappears upon calcination with the simultaneous growth of the broad (001) reflection of nanocrystalline Mo_5O_{14} (Fig. 5.4 b).

In case of nanocrystallinity, there should be several very broad peaks, instead of one single halo, whose intensities grow with raising the calcination temperature due to the increasing degree of sample crystallinity. Hence, it seems likely that the structure of the spray-dried sample is characterised by some structural ordering in the layer plane but does not possess any periodicity in the perpendicular direction, e.g. along [001].

Moreover, the gradual increase of the intensity of the (001) reflection during the crystallization of the Mo_5O_{14}-type structure from an amorphous, spray-dried precursor indicates a lamellar, or pseudolamellar character of this mixed oxide (pattern b, c, d of Fig. 5.4). When the layers begin to pack into slabs, the 3D periodicity of the MoVW oxide becomes evident. That is also demonstrated by the increasing intensities of the basal reflections. The proposed structural model fits well with Raman spectroscopic data, which also indicates the presence of nuclei of the Mo_5O_{14} phase in the spray-dried material, and with TEM observations, which confirm the pseudolamellar character of the Mo_5O_{14} structure (vide infra).

Attention should also be focused on the fact that the crystallization process of the Mo-V-W oxide from the amorphous precursor is governed by a proper maintenance of the cation oxidation states during the thermal treatment steps to the final catalyst. According to the XRD analysis, calcination of the spray-dried precursor in an oxidizing medium, i.e. air, leads to the partial disintegration of the complex oxide phase of the Mo_5O_{14}-type as proven by the reflections of MoO_3 in the XRD pattern (Fig. 5.4, inset). Hence, the treatment of the spray-dried precursor under well chosen

tempering or reaction conditions is a critical requirement for the synthesis of well-crystalline, single phase Mo-V-W oxide (Fig. 5.4 c, d, e).

Table 5.2: XRD data

2Θ	D	Int. (%)	Phase
7.77	11.4	32	$(MoVW)_5O_{14}$
8.69	10.17	29.9	$(MoVW)_5O_{14}$
12.30	7.19	10.5	MoO_3 (r)
15.6	5.68	8.4	$(MoVW)_5O_{14}$
22.29	4.0	100	$(MoVW)_5O_{14}$
23.13	3.84	55.2	$(MoVW)_5O_{14}$
23.44	3.79	39.0	$(MoVW)_5O_{14}$
24.82	3.58	39.4	$(MoVW)_5O_{14}$
27.28	3.266	36	MoO_3 (r)
31.66	2.824	17.1	$(MoVW)_5O_{14}$
33.74	2.66	32.8	MoO_3 (r)
38.98	2.31	12.2	$(MoVW)_5O_{14}$

5.3.5 HRTEM

According to TEM, the particles of the spray-dried, and the calcined sample (air, 623 K; helium, 713 K) are of platelet-like shape with sizes of about 200 nm in length and 10 nm in width. With the help of selected area electron diffraction (SAED) patterns, the structure of the sample was identified as a Mo_5O_{14}-type. SAED pattern oriented along [001] zone axis and given in the inset of Fig. 5.5. reflects the closely packed character of the Mo_5O_{14} structure in the basal plane. SEAD pattern shown in the inset of Fig. 5.5 displays a set of strips similar to those characteristic of lamellar materials Thus, this ternary oxide can be considered as pseudolamellar. These layers are

alternating along the [010] direction. It is evident from the TEM observations that the (010) plane is the most developed plane of the crystalline particle.

At higher magnification, the structure of the sample is rather complicated. A cubic motif of the dark spots is clearly visible in the HRTEM micrograph of the sample indicating the Mo_5O_{14}-type structure viewed along the [001] orientation (see Fig. 5.5). The distance between two neighbouring spots is equal to 2.25 nm, which fits well with half of the unit cell parameter of Mo_5O_{14}. This value also coincides with the distance between two channels formed by the pentagonal bipyramides in the structure of this complex ternary oxide[17,18]. Therefore, it can be suggested that the micrograph in Fig. 5.5 shows the channels in the basal plane. On the other hand, the pseudolamellar nature of the crystal structure is evident from the HRTEM image of the crystal viewed down the [010] projection (Fig. 5.6) from which an interlayer
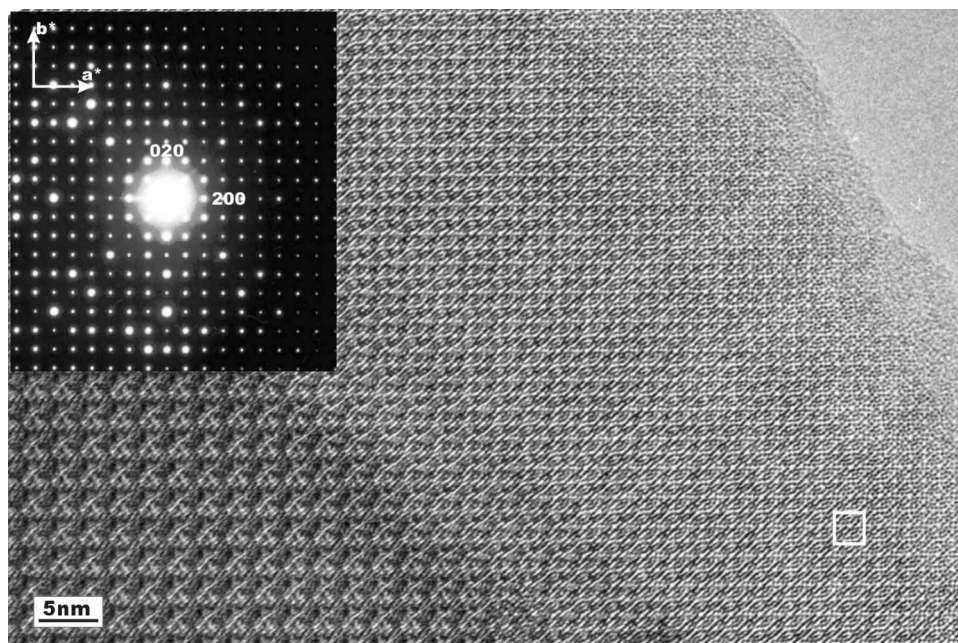
Figure 5.5: HRTEM image and SAED patterns of Mo_5O_{14} structure viewed along the [001] direction

parameter as long as 1 nm can be measured.

EDX measurements indicate similar elemental compositions for all investigated particles of the ternary oxide sample. As evident from EDX, the concentrations of Mo, V, and W are equal to 68.13, 22, and 9.88 at%, respectively. These values are in a good agreement with the EDX data obtained by SEM analysis.

The XRD and TEM data presented in this work are in a good agreement with earlier observations on the structural arrangement of the MoVW oxide with an admixture of MoO_3[6,9]. The structural evolution of the main ternary phase during thermal treatment seems to be similar to the structural transformation of the catalyst in the present study. The XRD pattern of the precursor described in[6,9,16] shows the same diffuse peaks, which became sharp and strong due to crystallisation of the initial structure upon thermal treatment. Note that the (210) and (200) reflections, although very broad, already exist in the XRD pattern of the precursor, whereas the (001) reflection is almost absent in the XRD diffractogram. After the first calcination step of the precursor, the reverse situation was observed. The former reflections disappear, and the latter start to grow until the sharp and intense peaks appear after further heating. From the structural point of view, this implies that there is a kind of short-order and structural periodicity in the [210] direction, but it is very poor along the [001] direction. This finding is in line with recent TEM data[7,9], which indicated diffusion reflections in the SAED pattern. Irregular packing of thin layers within the ternary oxide particles in the direction perpendicular to the (001) basal plane leads to the so-called bundle structure. The TEM results obtained in this study also show this pseudolamellar character of the ternary MoVW phase.
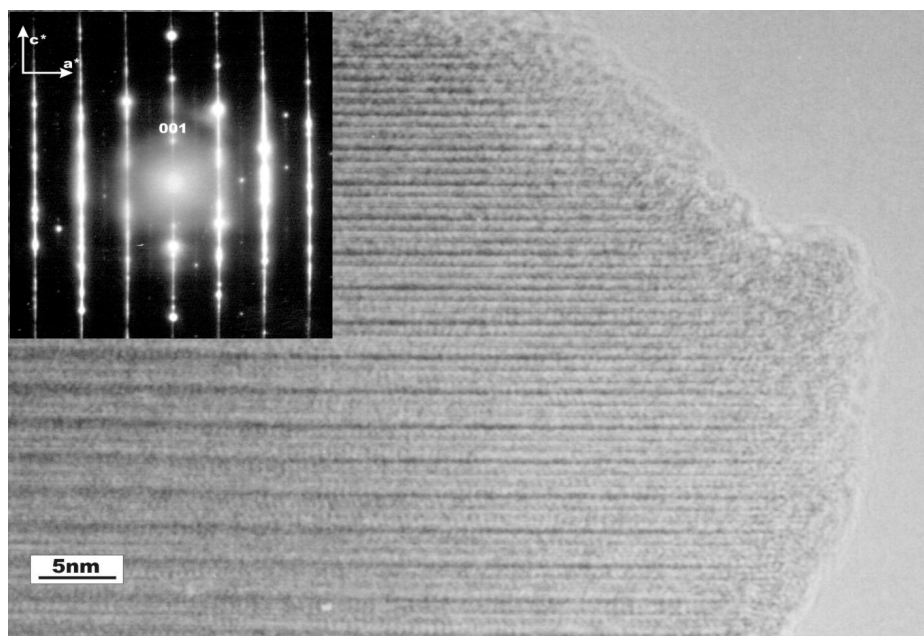
Figure 5.6: HRTEM image and SAED pattern of Mo_5O_{14} structure viewed along the [010] direction

5.3.6 Raman Spectroscopy
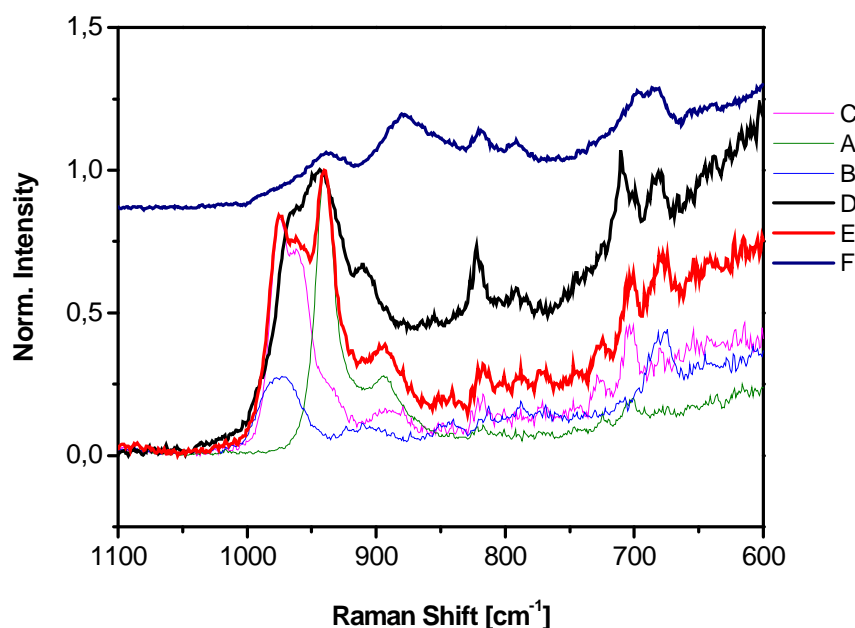
Figure 5.7: Raman spectrum normalised to the intensity of the band at 944 cm^{-1} of A the ammonium heptamolybdate solution; B vanadyl oxalalte solution, C the ammonium meta tungstate solution, D the mixed solution (0,53 mol/l Mo; 0,18 mol/l V; 0.07 mol/l W) E the sum as calculated from the respective weighted spectra of the pure starting compounds and fitted to the experimental spectrum, F the mixed solution (of D) after heat treatment at 353 K for 1h

Figure 5.7 shows the Raman spectrum of an aqueous mixed solution of the three transition metal compounds and the spectra of individual AHM, AMT and vanadyl oxalate solutions for comparison. The spectrum (a of Fig. 5.7) of the pure, colourless AHM (c=0.96 mol/l Mo) solution displays bands at 940, 894, 818, and 700 cm^{-1} in agreement with literature[19].

The Raman spectrum of the pure, blue vanadyl oxalate solution (c = 0.76 mol/l V) displays bands at 974, 908 and 678 cm^{-1} (b of Fig. 5.7), while a band is detected at 971 cm^{-1} for the pure, colorless AMT (c = 0.27 mol/l W) (c of Fig. 5.7). The spectrum d of Fig. 5.7 was recorded for the freshly mixed solution of the precursor solutions.

Raman bands of the fresh mixed solutions are observed at 964, 944, 910, 821, 790, 711 and 682 cm^{-1}, which are in the typical regime for Raman bands of polyoxo metallates. These bands tentatively could be assigned to terminal M=O vibrations in the regime between 1000 and 890 cm^{-1} and to M-O-M bridges in the regime between 890 and 600 cm^{-1}.

The calculation of the theoretical spectrum of a hypothetical, mixed solution, which was fitted to the experimental data (spectrum e of Fig. 5.7) shows bands at 973, 940, 894, 817, 701, and 678 cm^{-1}. Note that the band positions and observed relative intensities of the different signals vary from those of the freshly mixed solution. This hypothetical sum spectrum is clearly different from that of the freshly mixed solution. Hence, it can be assumed that already mixing the three starting solutions induces a chemical reaction towards a polyoxo compound on Mo basis with incorporated V and W.

Figure 5.7 F shows the spectra of a freshly mixed solution, after additional heat treatment at 353 K for 1 hour. The Raman spectrum of this solution (spectrum b of Fig. 5.7) also differs decisively from that of the freshly mixed solution (spectrum e of Fig. 5.8). A new intense band appears at 878 cm^{-1} together with bands at 697 and 683 cm^{-1}. These bands appear in the typical regime of frequencies of Me-O-Me bridge stretching modes. The observation of these bands, thus, points to the formation of polymeric aggregates after this additional heating presumably containing W and V due to the absence of their respective Raman bands in the spectrum.

The Raman bands, detected at 938 and 872 cm^{-1} in the solution Raman spectrum (Fig. 5.7, F), are also observed in the Raman spectrum of the spray-dried solid (spectrum a of Fig. 5.8) together with a broad wing extending to lower wavenumbers and a very weak band at 682 cm^{-1}. Simultaneously, all other bands disappear which were recorded for the solution.

Spectral alterations are evident as compared to the solution Raman spectra (Fig. 5.7, 5.8). By comparison with Raman spectra reported for $Mo_{0.68}V_{0.23}W_{0.09}$ mixed metal oxide catalysts[6,9], the band observed at 872 cm^{-1} after this treatment step is tentatively attributed to a mixed oligomeric species with a molecular structure, which might already contain the structural motif of Mo_5O_{14}, i.e. the central pentagonal bipyramid surrounded by five octahedra[14]. In this context, is has to be mentioned

that similar Raman spectral bands were reported for the Keplerates also containing the pentagonal bipyramids as a structural motif[20,21].
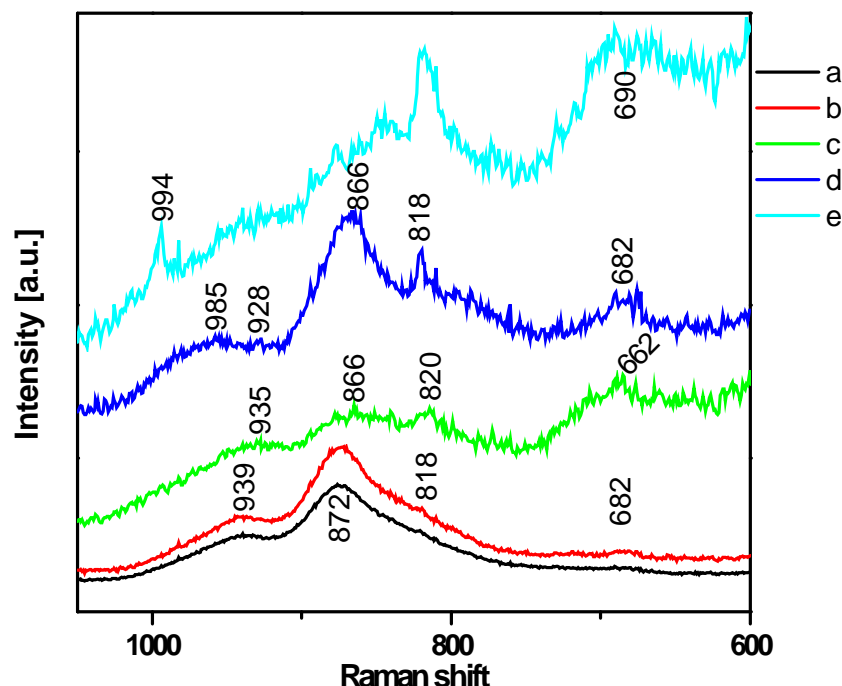
Figure 5.8: Raman spectra of the MoVWO oxide precursor/catalysts: a) spray-dried, b) dried in air at 383 K overnight, c) calcined in air at 623 K for 2h, d) calcined in air at 623 K for 2h and in helium at 713 K for 2h and e) heated in air at 723 K for 2h

Thus, the combined information from XRD and Raman spectroscopy indicate the presence of a molecular MoVW precursor species and the absence of long-range order in the spray-dried solid precursor. After further drying at 383 K overnight, the Raman spectrum (spectrum b of Fig. 5.7) of the sample has not changed.

The relative intensity of the band at 866 cm^{-1} attributed to the polyoxo $(MoVW)_5O_{14}$-precursor however has increased somewhat as compared to the band at the same wavenumber of the spectrum recorded in solution. A comparison with the XRD results (Fig. 5.4) clarifies that the X-ray amorphous spray-dried precursor consists of these polyoxo clusters.

Calcination of the sample in air at 623 K for 2h resulted in a Raman spectrum (spectrum c of Fig. 5.8) which has considerably altered as compared to the spectra of the dried materials (spectra a of Fig. 5.8).
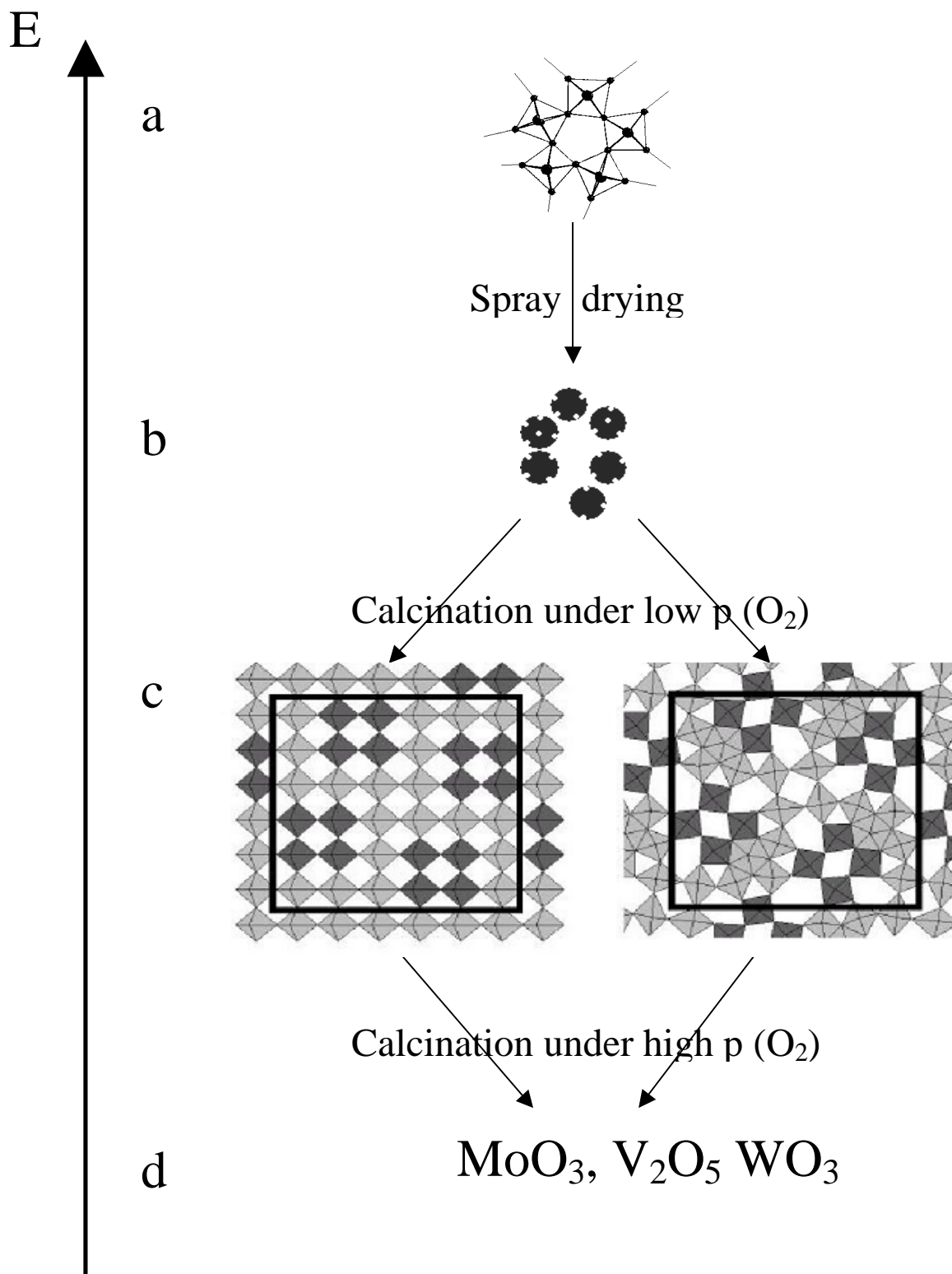
Figure 5.9: a) Oligo anions in solution b) Material after spray–drying (with oxygen defects) c) Material calcined under low oxygen partial pressure where a variety of defects can be obtained d) Binary oxide materials calcined under higher oxygen partial pressure (i.e. air)

The formerly prominent bands between 800 and 1000 cm^{-1} have changed in shape and have lost their structure. The band at 662 cm^{-1} assigned to Me-O-Me bridges shows a higher relative intensity as compared to the bands between 800 and 1000 cm^{-1}.

This increased intensity might indicate an increased degree of cross linking in the solid. However, the Raman spectrum is still poorly resolved and is additionally characterised by a high background extending to lower frequencies, which points to an ill-defined, poorly crystallised material, in line with the XRD results (see Fig. 5.4).

The Raman spectrum d of Fig. 5.8 was recorded of the catalyst additionally tempered in He at 713 K for 2h. The spectrum is more resolved compared to the spectrum of the preceding step and shows bands and shoulders at 985, 949, 866, 818, 682, and 584 cm^{-1}.

The Raman bands are more resolved and the background is reduced compared to the mixed oxide after thermal treatment at 623 K in air. The observed band positions are in agreement with those reported by Dieterle at al.[9] and Blume[13] for the catalyst prepared by other methods and a different transition metal ratio. These spectral alterations indicate an increase in crystallinity of the mixed oxide after this treatment step that fits well with the XRD results, which proved the crystallisation of the Mo_5O_{14}-type mixed oxide.

When the spray-dried sample was additionally calcined at 723 K for 2 h, Raman shows bands or shoulders at 995, 875, 845, 818, and 667 cm^{-1} (spectrum f of Fig. 5.8). The Raman band at 891 cm^{-1} can be attributed to monoclinic Mo_4O_{11}[22], whereas the band at 845 cm^{-1} may be assigned to orthorhombic Mo_5O_{14}, which is characterised by Raman bands at 983, 909, 845, 790 and 728 cm^{-1} [13]. But XRD did not reveal the presence of Mo_4O_{11} in the sample [see Table 5.2] that is likely to be caused by its XRD amorphous state. Obviously, calcination in air at temperatures below 673 K (data not shown) leads to the formation of $(MoVW)_5O_{14}$ in phase mixtures with traces of MoO_3. Temperatures higher than 673 K result in the decomposition the majority $(MoVW)_5O_{14}$ phase into a broad phase mixture.

5.3.7 Catalytic properties

The catalytic performances of the different, above described materials were studied in the acrolein oxidation under identical reaction conditions. Fig. 5.10 shows the acrolein conversions at 563 K and at $\tau = 0.12$ g×s/ml as a function of time on stream. The selectivities to acrylic acid and $CO_2 + CO$ with time on stream are displayed in Fig. 5.11. It is evident from Fig. 5.10, 5.11 that the precursor pre-treatment in air, or in air plus He considerably affected the final catalytic properties.

The catalyst, only calcined in air at 623 K for 2 hours, shows an activation period similar to that observed for an industrial MoVWO catalyst[7]. It is important to note that a significant change in catalytic performance was not observed during the first minutes of operation, which could be related to surface processes, like desorption of water or surface reduction.

Such processes can be excluded to be responsible for the improving catalyst activities. Moreover, the BET surface areas of all materials were very low with about 4 m^2/g and did not change upon the different calcination treatments or catalysis.

Textural changes, thus, can be excluded to be responsible for the changing catalytic activity. As suggested in the previous work[7], such an activation period is related to the formation of an active crystalline phase. In full agreement and confirming previous results, XRD of the catalyst after operation in the acrolein oxidation for 80 h revealed the exclusive presence of crystalline $(MoVW)_5O_{14}$ in this sample (diffractogram e of Fig. 5.4).

The selectivity to acrylic acid over the catalyst calcined in air also slightly increased
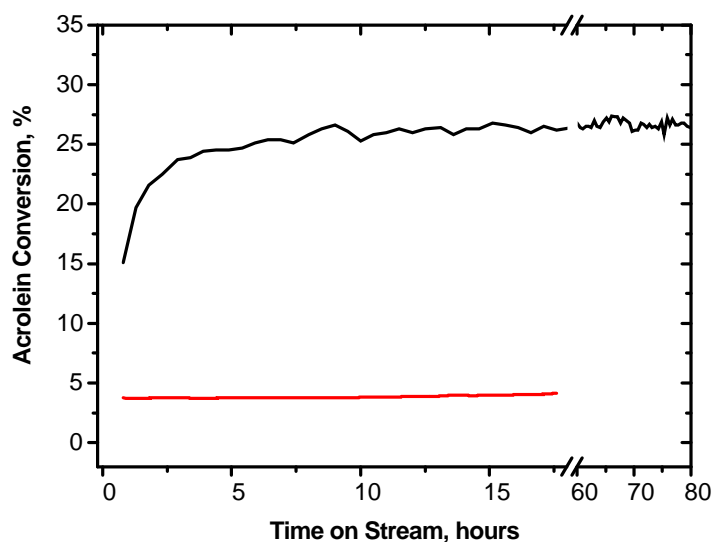
Figure 5.10: Acrolein conversion over the $Mo_9V_3W_{1.2}O_{14}$ catalyst at 563 K and as a function of operation time on stream. Spray dried sample after calcination in air at 623 K for 2 hours (black), spray dried sample after calcination in air at 623 K for 2 hours and subsequent treatment in He at 713 K for 2 hours (red). Reaction mixture composition: 4 % C_3H_4O, 8 % O_2, 20 % H_2O, balance – He

with time on stream and reached 97% at an acrolein conversion of 25-26%, while that to $CO + CO_2$ decreased (Fig. 5.8). This slight change in the selectivities over the first 1.5 hours might be related to red ox processes within the catalyst material[6].

However, it has to be stated that the time scale of the selectivity changes does not correlate with that of the increasing catalyst activity. Hence, this result once more proves that this increasing catalyst activity is not directly related to red ox processes in the material, which should be reflected by selectivity alterations.
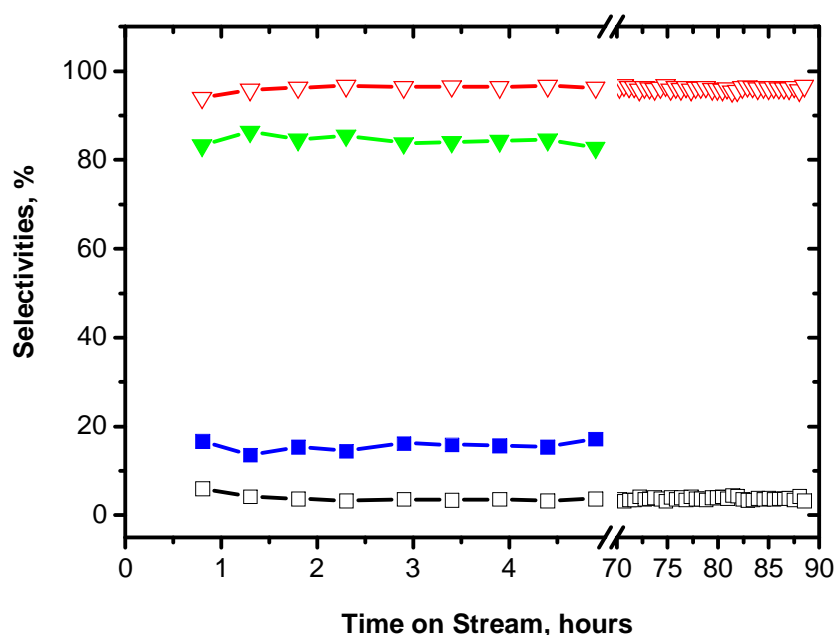
Figure 5.11: **Selectivities to acrylic acid (triangles) and $CO + CO_2$ (squares): spray dried sample after calcination in air at 623 K for 2 hours (open triangles and squares), spray dried sample after calcination in air at 623 K for 2 hours and subsequent treatment in He at 713 K for 2 hours (filled triangles and squares).**

The steady state selectivity to acrylic acid of 97 % finally reached is close to that of the industrial catalyst[7]. The catalyst, which was additionally treated in He at 713 K for 2 hours, only reached a 6-7 times lower acrolein conversion under identical reaction conditions. Its selectivity to acrylic acid was also lower with 86%.

It is important to emphasise that treatments, which lead to the decomposition of the Mo_5O_{14}–type structure, were not applied in the present catalytic tests. Previous investigations have proven[9] that the Mo_5O_{14}-type structure is stable up to 818 K in

He. Thermal treatments at temperatures above 829 K led to the decomposition of the metastable Mo_5O_{14} phase to stable MoO_3 and MoO_2[9]. Additionally, strong oxidative or strong reductive conditions were not used in the present study, which also result in the formation of phases with a higher or with a lower degree of reduction, such as MoO_3 or Mo_2O_{5-x}[6,9,23].

XRD analysis on the sample with the high catalytic activity (sample heated in air at 623 K for 2 h) revealed that a crystalline Mo_5O_{14}–structure appears after operation in the acrolein oxidation reaction (Fig. 5.4 e). As was shown previously the structure of the sample before reaction represents poorly crystalline (almost X-ray amorphous) material.

It seems likely that the induction period, which was observed for this sample is caused by crystallisation of the Mo_5O_{14} phase during the reaction. Note that the catalyst heated in air and in helium and composed of single crystalline Mo_5O_{14}–type structure shows low activity and less selectivity for acrolein in spite of identical XRD patterns of the activated material.

This phenomenon might be associated with different `real structures´ of the compound under reaction conditions e.g. sise of the Mo_5O_{14} particles, degree of nanocrystallinity, different oxidation states of molybdenum, vanadium and tungsten. Further, the character of the structural disordering during the reaction might also be a reason. This result shows the full complexity of the system by demonstrating that the long range structure of a catalyst is necessary but by no means sufficient information to obtain a structure–function relationship. New ways in catalysis research are therefore recommended that investigate in detail the real structure of the material in situ under reactive conditions.

5.4 CONCLUSION

A synthesis procedure has been developed in this work, which allowed the preparation of the single phase, well-crystallised Mo_5O_{14}-type oxide. The whole process of structure formation starting from the precursor solutions up to the final product has been closely monitored. A strong interaction of AHM, AMT and vanadyl ions involving the formation of Me-O-Me bridges and a mixed Mo, V, W compound was observed with a structure already being closely related to the Mo_5O_{14}-type. This

structural motif was maintained during the spray-drying process but the material showed a low crystallinity. Further thermal treatment removed ammonia, water and oxalate and increased the state of crystallinity. Whilst calcinations in air led to over oxidation with a phase mixture amongst a well crystallised Mo_5O_{14}-type structure, the pure single phase was only obtained by additional treatment in helium.

Particles of this Mo_5O_{14}-type compound are oriented along the [001] and the [010] zone axes. Micro diffraction patterns show the closely packed character of the Mo_5O_{14}-type structure in the basal plane. This ternary oxide is pseudolamellar with alternating layers along the [010] direction and a strongly developed (010) face. Structure refinement showed decreased **a** and **b** lattice parameters with respect to Kihlborg *et al.*[10], but an increased **c** parameter. This effect is probably due to incorporation of V and W into the lattice. This statement is also supported by Raman spectral features and shows the importance of V and W as structural promoters to maintain the Mo_5O_{14}-type phase presumably by stabilizing the pentagonal bipyramides.

Whilst the catalyst that formed the Mo_5O_{14} structure after an induction period of about 2.5 h achieved the highest catalytic activity for acrolein oxidation, the synthesised single-phase material showed less activity but its selectivity was almost as high as the industrial material. Some important conclusions can be drawn from this. Apparently the active material is single-phase but distinctively different from the perfect structure of Mo_5O_{14}. The Mo_5O_{14} structure is an idealised endpoint that is formed under reduced oxygen partial pressure by the organization process of a mixture of oligo anions, which are generated in solution. The active phase is metastable until crystallisation and oxidative decomposition into binary oxide phases occurs under high oxygen partial pressure (air and above). This is illustrated in Fig. 5.9.

These experimental results are highly significant for future catalysis research, because they confirm that a single-phase material can be catalytically active, and that no phase cooperation or spill over phenomena are functionally essential. Additionally, this work has highlighted the full complexity of these systems, because x-ray powder diffractometry indicates the same crystallographic phase for two differently active materials. This difference can only be explained by different `real´ structures of the two materials. It must be strongly emphasised that precise analytical

methods need to be developed, that look into the details of a real structure of a given phase in order to determine structure–function relationships. The synthesis procedure reported in this paper is an example for this approach.

Reference List

[1.]   A. N. Kurtz, R. W. Cunningdam, A. W. Naumann (Union Carbide Co.) US 4111983 (1978).

[2.]   V. Novak, L. Sokol, J. Jelinek, CS 1207807 B(1981)

[3.]   N. Bertolini, S. Ferlazzo (Euteco Impianti S.p.A.) US 4289654 (1981)

[4.]   T. Kawajiri, S. Uchida, H. Hironaka (Nippon Shokubai Kagaku) EP 427 508 A1 (1991)

[5.]   A. Tenten, F.-G. Martin, H. Hibst, L. Marosi, V. Kohl (BASF AG), EP 668104 B1 (1995)

[6.]   G. Mestl, Ch. Linsmeier, R. Gottschall, M. Dieterle, J. Find, D. Herein, J. Jäger, Y. Uchida, and R. Schlögl, J. Mol. Catal. A, 162 (2000) 455-484.

[7.]   O. Ovsitser, Y. Uchida, G. Mestl, G. Weinberg, A. Blume, M. Dieterle, H. Hibst, and R. Schlögl, J. Mol. Catal. A, 185, 291-303, (2002).

[8.]   M. Dieterle, PhD thesis, TU Berlin, 2001.

[9.]   M. Dieterle, G. Mestl, J. Jäger, Y. Uchida and R. Schlögl, J. Mol. Catal. A, 174 (2001) 169-185.

[10.]   L. Kihlborg, Ark Kemi, 21 (1963) 427.

[11.]   T. Ekström, M. Nygren, Acta Chem. Scand., 26, (1972), 5, 1827-1835.

[12.]   T. Ekström, M. Nygren, Acta Chem. Scand., 26, (1972), 5, 1836-1842.

[13.]   A. Blume, PhD thesis, Berlin, 2002.

[14.]   G. Mestl, J. Raman Spectrosc., 33, 335-347, (2002).

[15.]   L.P. Solovyeva, S.V. Tsybulya, G.N. Kryukova, E.M. Moroz, JSTCAM 32 (1991) 18.

[16.]   H. Werner, O. Timpe, D. Herein, Y. Uchida, N. Pfaender, U. Wild, R. Schlögl, and H. Hibst, Catal. Lett., 44 (1997) 153.

[17.] Kihlborg, L., Acta Chem. Scand., 26, (1972), 3381.

[18.] W. Ueda, K. Oshihiara, Appl. Catal. A, 200 (2000) 135-143.

[19.] G. Mestl, T.K.K. Srinivasan, Catal. Rev.-Sci. Eng., 40 (4), 451-570 (1998).

[20.] A. Müller, S. Polarz, S.K. Das, E. Krickemeyer, H. Bögge, M. Schmidtmann, B. Hauptfleisch, Angew. Chem., 111, 3493-3443 (1999).

[21.] A. Müller, S. Sarkar, S.Q.N. Shah, H. Bögge, M. Schmidtmann, S. Sarkar, P. Kögerler, B. Hauptfleisch, A.X. Trautwein, V. Schünemann, Angew. Chem., 111, 3435-3439 (1999).

[22.] A.A. Bolznan, B.J. Kenned, C.J. Howard, Austr. J. Chem., 48, 683 (1995).

[23.] Y. Uchida, G. Mestl, O. Ovsitser, J. Jäger, A. Blume and R. Schlögl, J. Mol. Catal. A., 187, 247-257, (2002)

6 Conclusion and Outlook

6.1 STRUCTURE - ACTIVITY RELATION

Mo Oxide model catalysts with a variety of structural and chemical complexity have been presented. A tremendous structural diversity was shown on binary molybdenum and oxygen containing systems. Additionally various degrees of crystallinity and particles sizes occurred as smaller particles do not necessarily show the same crystalline structure as the bigger particles.

A number of nanostructured molybdenum oxides with high structural complexity has been successfully prepared. Depending on the preparation conditions trimolybdate, hexagonal MoO_3, orthorhombic MoO_3 and a supramolecular compound was prepared. Compounds showing a very similar crystal structure but a different degree of protonation showed a decisively different catalytic behaviour.

No material is active as precipitated. Transformation into metastable active phases occurred at about 300 °C, as seen from the TPRS experiments. Above 450 °C phase transformation into orthorhombic MoO_3 significantly reduced the catalytic activity, as shown in the second cycle of the TPRS run. Whilst it is often reported that additives increase the catalytic activity, it is more likely that they merely stabilize the metastable Mo-O phase.

Many attempts have been carried out in the literature to develop structure activity relations. This work has demonstrated that such relations by integrative methods as XRD or Raman have to be treated with extreme caution, as the existence of many differently shaped and structured particles were only observed with HRTEM. Only a minor amount of the mass balance exposed to the surface is responsible for catalysis.

The relevance of this effect for catalysis becomes obvious by comparing the small scale samples with the large scale samples. The latter ones consist of larger, more homogeneous particles. Their catalytic behaviour especially the deactivation is much more rapid as with the small scale samples.

The TPRS experiments show clearly that even a chemically simple system can be tuned by controlling its thermodynamic parameters. This opens two new pathways. Firstly, catalytic reactions can be studied and understood on comparatively simple model catalysts. Secondly, catalysts can be optimised by varying and controlling thermodynamic parameters during the preparation process and not only by additives whose role often is obscure.

A higher level of complexity is reached by addition of vanadium and tungsten into the system. However, the model character still prevails because in contrast to real multi element industrial systems only one crystalline phase (Mo_5O_{14}) is observed.

The importance of the real structure of a catalyst including its amorphous components is nicely demonstrated in the work concerning the Mo_5O_{14} system. The catalyst which was calcined in air at 350 °C showed the highest activity for the acrolein partial oxidation after an induction period of about 2.5 h. The post mortem sample showed the Mo_5O_{14} structure. The synthesised single phase material is behaving differently. The activity is much lower but selectivity is close to the industrial material.

Some important conclusions can be drawn from this. Apparently the active material is a single crystalline phase but distinctively different from the perfect structure of Mo_5O_{14}. The Mo_5O_{14} structure is an idealised endpoint that is formed under reduced oxygen partial pressure by the organization process of a mixture of oligo anions, which are generated in solution. The active phase is metastable until crystallisation and oxidative decomposition into binary oxide phases occurs under high oxygen partial pressure.

6.2 PREPARATION AND REACTIONS IN SOLUTION

Often in the catalysis literature the precipitation process carried out in water is neglected. In this thesis the aqueous chemistry and structure formation was studied carefully. In addition to the potentiometric measurements in situ Raman spectroscopy was performed.

The in situ Raman data on the molybdenum-only model systems presented in this work has clearly demonstrated the severe temperature effect on the nature of molybdate species in solution. Also the pH traces are very sensitive to a change in

reaction mechanism in solution. Especially a shift in the equilibrium between α and β octamolybdate is the important factor influencing the nature of the final precipitate and therefore of the catalyst precursor. Further in this context different activities and consequently solubility products need to be mentioned. This is the reason why also the normalised pH traces are different, especially when cations are changed.

The first model systems are vital for understanding the genesis of the second system (multicomponent). The molybdenum chemistry as a function of pH and temperature is very similar. At the octamolybdate equilibrium the added vanadyl is able to link the prevailing elements and a different structure namely Mo_5O_{14} is generated. It is noteworthy that pentagonal bipyramids appear in the supramolecular compound as a structural motif as well as in Mo_5O_{14}.

The whole process of structure formation starting from the precursor solutions up to the final product has been closely monitored by using UV/Vis, ESR, Raman and ^{95}Mo NMR spectroscopy. The results obtained show that structure formation starts as early as during the mixing process of the initial precursor solutions. Addition of acidic vanadyl oxalate causes protonation and condensation of the heptamolybdate ions into octamolybdate ions that are linked by vanadyl species and form a polymeric network. Addition of tungsten atoms clearly enhance this process. This polymeric network is an essential precursor for the final Mo_5O_{14}–type structure. In this case precipitation is inconvenient to obtain the solid catalyst precursor. Therefore spray-drying was used to conserve the structural motif.

6.3 OUTLOOK

In the future the interplay between model development and complex real system can be applied to even more challenging systems containing more additives such as $MoVTeNbO_x$. The key step identified in the model system, namely the isomerisation reaction between α and β octamolybdate will be decisive in the $MoVTeNbO_x$ preparation procedure or any other complex catalytic system containing molybdenum.

During this isomerisation process the system is most reactive as shown by in situ Raman spectroscopy in the model case. Therefore the structure formation will depend strongly on the treatment during this stage e.g. on the temperature or on the

element added at the time. Very likely one step will determine the following. Consequently the mixing sequence will play a role.

In this context another function of the additives can be discussed. One or more components might act as a transporting reagent for gas phase vapour deposition. This might be the key step for achieving high activity. As discussed in the Mo_5O_{14}-case the crystalline phase might just be the support for an either ill defined amorphous or highly dispersed material. Again, this hypothesis can only be confirmed by a well investigated model system, because only in this case effects from the additives can be separated from the effects from the support.

Table of Figures:

Table of Tables:

Stefan Knobl

Persönliche Information	
• Eltern:	Katharina Knobl, geb. Bäuerlein, Wilhelm Knobl
• Familienstand:	ledig
• Staatsangehörigkeit:	deutsch
• Geburtsdatum:	23.09.1973
• Geburtsort:	Selb

Ausbildung

1980-1984:	Dr. Franz-Bogner-Schule, Selb.
1985-1993:	Abitur, Gymnasium Selb.
1993-1994:	Zivildienst, Zentrale Diakonie-Station, Selb.
1996:	Diplomvorprüfung, Universität Tübingen.
1996-1997:	University Of Wales, Bangor.
2001:	Diplom-Chemiker, Universität Tübingen.
2001-2004:	Doktorand, Fritz-Haber-Institut der Max-Planck-Gesellschaft, Berlin.

Praktika

1997:	Bayer AG Leverkusen.

Tätigkeiten neben dem Studium

- Mitglied der Vertreterversammlung des Studentenwerks Tübingen.
- Mitglied des Verwaltungsrates des Studentenwerks Tübingen.
- Mitglied der Studienkommission des Fachbereichs Chemie.